SPECTRALLY SELECTIVE $Al_XO_Y/Pt/Al_XO_Y$ SOLAR ABSORBER COATINGS FOR HIGH TEMPRATURE SOLAR-THERMAL APPLICATIONS

ZEBIB YENUS NURU

A thesis submitted in a partial fulfilment of the requirements for the degree of

Doctor of Philosophy

in the

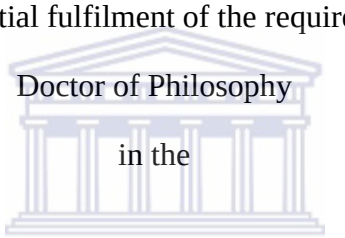

DEPARTMENT OF PHYSICS

UNIVERSITY OF WESTERN CAPE

Supervisor: Prof. M. Maaza, iThemba LABS, National Research Foundation

Co-supervisor: Prof. C. J. Arendse, University of the Western Cape

February 2014

KEYWORDS

“SPECTRALLY SELECTIVE $Al_XO_Y/Pt/Al_XO_Y$ SOLAR ABSORBER COATINGS FOR HIGH TEMPRATURE SOLAR-THERMAL APPLICATIONS”

ZEBIB YENUS NURU

Solar absorbers

Absorptance

Emittance

Spectral selectivity

Optical constants

Morphology

Structure

Composition

Annealing

Thermal stability

Optical performance

Diffusion barrier

ABSTRACT

"SPECTRALLY SELECTIVE $Al_XO_Y/Pt/Al_XO_Y$ SOLAR ABSORBER COATINGS FOR HIGH TEMPRTAURE SOALR-THERMAL APPLICATIONS"

ZEBIB YENUS NURU

The limited supply of fossil hydrocarbon resources and the negative impact of CO_2 emission on the global environment dictate the increasing usage of renewable energy sources. Concentrating solar power (CSP) systems are the most likely candidate for providing the majority of the renewable energy. For efficient photo-thermal conversion, these systems require spectrally selective solar absorber surfaces with high solar absorbance in the solar spectrum region and low thermal emittance in the infrared region. In this thesis, a spectrally selective $Al_xO_y/Pt/Al_xO_y$ multilayer solar absorber was designed and deposited onto copper substrate using electron beam evaporation at room temperature. The employment of ellipsometric measurements and optical simulation was proposed as an effective method to optimize and deposit the multilayer solar absorber coatings. The optical constants measured using spectroscopic ellipsometry, showed that both Al_xO_y layers, which used in the coatings, were dielectric in nature and the Pt layer was semi-transparent. The optimized multilayer coatings exhibited high solar absorptance (α) ~ 0.94±0.01 and low thermal emittance (ε) ~

0.06 ± 0.01 at 82^{o}C.The structural and optical properties of the coatings were investigated. It was found that the stratification of the coatings consists of a semitransparent middle Pt layer sandwiched between two layers of Al_xO_y. The top and bottom Al_xO_y layers were non-stoichiometric with no crystalline phases present. The Pt layer is in the fcc crystalline phase with a broad size distribution and spheroidal shape in and between the rims of Al_xO_y. The surface roughness of the stack was found to be comparable to the inter-particle distance. To study the thermal stability of the multilayer solar absorber coatings, the samples were annealed at different temperatures for different duration in air. The results showed changes in morphology, structure, composition, and optical properties depend on both temperature and duration of annealing. The XRD pattern showed that the intensity of Pt decreased with increasing annealing temperature and therefore, disappeared at high temperature. With increasing annealing temperature, an increase in the size of Pt particles was observed from SEM. The $Al_xO_y/Pt/Al_xO_y$ multilayer solar absorber coatings deposited onto Cu substrate were found to be thermally stable up to 500^{o}C in air for 2 h with good spectral selectivity α/ε of 0.951/0.09. At 600^{o}C and 700^{o}C, the spectral selectivity decreased to 0.92/0.10 and 0.846/0.11 respectively, which is attributed to the diffusion of Cu and formation of CuO and Cu_2O phases. Long term thermal stability study showed that the coatings were thermally stable in air up to 450^{o}C for 24 h. To elucidate the degradation mechanism beyond 500^{o}C, HI-ERDA has been used to study depth-dependent atomic concentration profiles. These measurements revealed outward diffusion of the copper substrate towards the surface and therefore, the decrease in the constituents of the coating. Hence, to prevent copper from diffusing towards the coatings, a thin Tantalum (Ta) layer was deposited between the base Al_xO_y layer and the copper substrate.The effect of a thin Ta layer on the thermal stability of $Al_xO_y/Pt/Al_xO_y$ multilayer solar absorber coatings was investigated. The $Cu/Ta/Al_xO_y/Pt/Al_xO_y$ multilayer solar absorber coatings were found to be thermally stable up to 700^{o}C in air for 2 h with good spectral

selectivity α/ε of 0.937/0.10. At 800^{o}C, the spectral selectivity decreased to 0.870/0.12, which is attributed to the diffusion of Cu and formation of CuO phase. The formation of CuO phase was confirmed by XRD, EDS and Raman spectroscopy. Long term thermal stability study showed that the coatings were thermally stable in air up to 550^{o}C for 24 h. Therefore, the Cu/Ta/Al_xO_y/Pt/Al_xO_y spectrally selective solar absorber coatings can be used for high temperature solar-thermal applications.

DECLARATION

I declare that

"SPECTRALLY SELECTIVE $Al_XO_Y/Pt/Al_XO_Y$ SOLAR ABSORBER COATINGS FOR HIGH TEMPRATURE SOALR-THERMAL APPLICATIONS"

is my own work and that all the sources used have been indicated and acknowledged by means of complete references.

_____ _____

Zebib Yenus Nuru Date

ACKNOWLEGMENTS

I thank Allah/ God for the guide in which I have now opened a chapter to express my deep heart feeling in the following acknowledgements. This thesis wouldn't have been written without incentive and cooperation of many people, their good will, thoughtful and faith.

It is worth to thank Organization of Women Scientists for Developing World "OWSDW", Swedish International Development Cooperation Agency "Sida" and iThemba LABS-National Research Foundation of South Africa for financing my study.

My heartfelt gratefulness is extended to my supervisors, Prof. Malik Maaza and Prof. Christopher Arendse for their eternal supervision, patience, support, commitment, and their belief have been extraordinary in my academic work and I thank them for all the constructive criticism, which benefitted me hugely both during the experimental part and the compilation of this thesis.

I would like to appreciate Dr Theophilius Frederic George Muller for giving me short introduction on simulation programme that complements my experimental work. Also, I would like to thank for his valuable discussion, support and kindness.

Many thank to Dr O. Nemroui for his guidance and valuable discussions especially during my first year that helped me to find out the direction of my project.

To my mother (Kedija Abdulahi), I have no words to express my gratitude for your constant love, support and encouragement to study away from home, and to my youngest and smart

brother (Naser Yenus Nuru) for his commitment and time to follow up the status of my scholarship when I was in a place where there was a limited access of internet connection.

I am overwhelmingly thankful for my husband (Mohammedmekin Mohammedseid Mohammednur) for allowing me to come to South Africa and of course, for his love, sacrifices, patience, trust and support throughout my studies.

I thank to Dr Saleh Khamlich for well coming and telling me what it is like to be in South Africa, and also, for being a good friend along with his scientific discussions throughout my study.

Special thanks to Dr. Tukabo Tesfamikael (Australia) for reflectance measurements and to David Andrew (Germany) for ellipsometry and Raman measurements.

I am grateful to Dr. Mulungsi Nkosi, Dr.Remy Bucher, Mr Phillip Sechogela and Mrs. Miranda for AFM, XRD, RBS and SEM measurements respectiveley.

My sincere gratitude goes to the Staff of Material Research Group and Physics Department (UWC) for their support, and many thanks to Ms Lusanda Nyusani and Angela Adams, who are secretary of the MRG and the Physics Department at UWC respectively, for always helping me with the registration and other issues.

Finally, I am indebted to my fellow students and friends at iThemba, UWC, Europe, Canada, USA and back home for their continuous support.

DEDICATION

To my father (Yenus Nuru).

Dad I wish you were alive.

It’s because of you that I’m here today.

You mean so much to me.

CONTENTS

LIST OF SYMBOLS, CONSTANTS AND ABBREVATIONS

T	Absolute temperature
λ	Wavelength
λ_c	Cut off wavelength
h	Plank's constant, 6.626 *10^{-34}Js
K_B	Boltzman's constant, 1.382*10-23 J/k
C	Speed of light in vacuum
$R(\lambda)$	Reflectance
$A(\lambda)$	Absorbance
$T(\lambda)$	Transmittance
$\varepsilon(\lambda)$	Emittance
$I_b(\lambda)$	Intensity of black body radiation
c	Concentration ratio
A_r	Area of the collector aperture
A_a	Energy of the absorber
α	Absorptance
$I_s(\lambda)$	Intensity of solar irradiance
E	Electric field
v	Velocity
E_o	Incident electric field
t	Time
P	Power
R	Bulk reflectance

c	Speed of light
ε_o	Permittivity of free space
μ_o	Permeability of free space
n	Refractive index
κ	Extinction coefficient
σ	Conductivity
ε	Complex dielectric constant
ω	Angular frequency
r_x	Complex amplitude reflection between layers (x= 1, 2, 3….)
N_x	Complex optical constant(x= 0, 1, 2, 3…)
δ	Change in phase
f	Frequency
γ	Dumping constant
ω_o, ω_p	Resonance frequency
e	Electronic charge
m	Mass of the electron
ω_p	Resonance frequency
IR	Infrared
AM	Air mass
CSP	Concentrating solar power
f	Selectivity
$UV-vis-NIR$	Ultraviolet-Visible-Near infrared

CHAPTER ONE

THEORETICAL BACKGROUND OF THE STUDY

1.1 ELECTROMAGNETIC RADIATION

The electromagnetic wave, first proposed by J.C. Maxwell, is a combination of electric and magnetic properties of all wave-like energy as it propagates in space, and classified according to the frequency of its wave. The electromagnetic spectrum, in the order of increasing wavelength ranges from gamma rays of wavelength ~ 10^{-8}µm to radio wave wavelength ~10^{10}µm. The wavelengths of interest for solar-thermal applications are found in the wavelength range of ultraviolet to infrared (0.3-50µm), thus include the solar spectrum range of 0.3-3µm and the spectral range of thermal radiation at about 2-50µm, which is emitted from a surface.

Solar and thermal radiation

Thermal radiation is the emission of electromagnetic waves from all matter that has a temperature greater than absolute zero [1.1]. The wavelength distribution of radiation depends on its absolute temperature, T. An idealized physical body that absorbs all incident

electromagnetic radiation is called black body. The Stefan–Boltzmann law states that the total energy radiated per unit surface area of a black body per unit time $I_b(T)$ is described by:

$$I_b(T) = \sigma T^4 \qquad 1.1$$

where σ is derived from other constant values given by:

$$\sigma = \frac{2\pi^2 k_B^{\ 2}}{15c^2h^2} = 5.670400\ x10^{-8}\ JS^{-1}m^{-2}K^{-4} \qquad 1.2$$

where k_B is the Boltzmann constant, h is Plank's constant, and C is the speed of light in a vacuum. The distribution of emitted power per unit area as function of wavelength, λ, is given by Plank's radiation law [1.2, 1.3]:

$$I_b(\lambda, T) = \frac{2\pi hc^2}{\lambda^5}\left[\frac{1}{e^{hc/\lambda k_B T} - 1}\right] \qquad 1.3$$

The symbol I_b represents the intensity of blackbody radiation, i.e. energy per unit area per unit time per unit wavelength interval at wavelength λ emitted by a blackbody surface.

The solar radiation is attenuated when it passes through the earth's atmosphere. Since the spectral distribution of the solar radiation also depends on the attenuation, various solar spectra can be measured at the earth's surface. The degree of attenuation is variable. The most important parameter that determines the solar irradiance under clear sky conditions is the distance that the sunlight has to travel through the atmosphere [1.4]. This distance is the shortest when the sun is at the zenith (directly overhead). The ratio of an actual path length of the sunlight to this minimal distance is known as the optical air mass (AM). When the sun is at its zenith the optical air mass is unity and the radiation is expressed as air mass one (AM1) radiation. When the sun is at an angle θ to the zenith, the air mass is given by:

Air mass = $(\cos\theta)^{-1}$ 1.4

AM0 radiation is an extraterrestrial spectrum of solar radiation outside the earth's atmosphere at which power density is the solar constant. The power density of the sun's radiation on the earth's surface is approximately 1.4 kW/m^2. This value varies slightly throughout the year by no more than 0.001 due to the change in earth-sun distance. The solar constant is defined as the quantity of solar energy (W/m²) at normal incidence outside the atmosphere at the mean sun-earth distance; i.e. 1367.7 W/m². However outside the earth's atmosphere, terrestrial solar radiation varies both in intensity and spectral distribution depending on the position on the earth and the position of the sun in the sky [1.5]. AM 1.5 is used in the following sections to calculate solar absorptance corresponding to an angle of 48.2º between the sun's position and the zenith.

The terrestrial solar spectral wavelength range is found between 0.3 µm and 4 µm with its maximum intensity at about 0.5 µm. This spectrum corresponds to an effective black body temperature of about 5800 K. Figure 1.1 shows a normalized solar spectrum and normalized blackbody radiation spectra at three different temperatures. The solar spectrum has several local minima, which are caused by absorption in the atmosphere mainly by water vapour, carbon dioxide and ozone [1.6]. There is minimal overlap between the solar spectral range of AM1.5 and the thermal emittance spectra at three temperatures of a blackbody-like surface. The non-overlap between the solar radiation and emittance spectra provides an opportunity to tailor a material and to achieve spectral solar selectivity which strongly determines the efficiency of the solar thermal collectors.

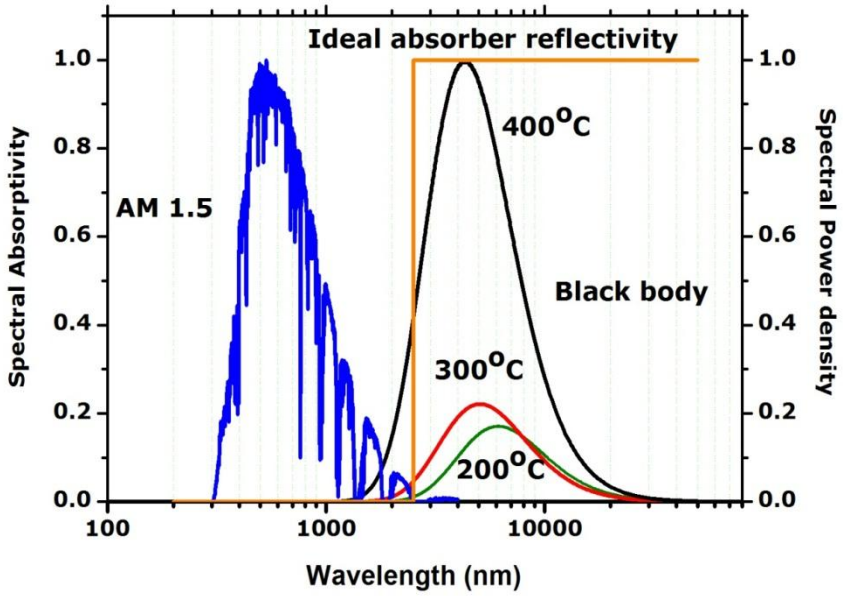

Figure 1.1.The normalized solar radiation spectrum (blue curve), black body radiation spectra at three different temperatures (black, red and green) and the ideal selective absorber reflectance spectrum (yellow).

1.2 SOLAR-THERMAL COLLECTORS

Solar-thermal collectors are solar collectors designed to collect and convert the incoming solar radiation into heat to satisfy some energy needs. Basically solar collectors are classified as concentrating and non-concentrating based on their concentration ratio (*c*). In non-concentrating collectors such as flat plate and evacuated tube, their concentration ratio is one and for concentrating solar power (CSP) systems such as parabolic-trough, parabolic-dish, and central tower their concentration ratio is above one. The concentration ratio depends on geometric characteristics, and it is given by:

$$C = \frac{A_a}{A_r} \qquad 1.5$$

where A_a is the area of the collector aperture, and A_r is the energy absorber. The geometric concentration ratio is a measure of the average concentration for the case where energy flux in the receiver is homogeneous, although this is not what actually happens. In contrast, very complex flux distribution reaches the receiver; in general high-intensity concentration occurs at the centre and decreases to the ends of the receiver [1.7].

Based on the operational temperature ranges of materials for solar energy applications, collectors can also be categorized as: (i) low temperature (< 100^oC), (ii) mid temperature (100^oC< T< 400^oC) and (iii) high temperature (> 400^oC). Hence, based on the classification, flat plate collectors operate at low temperature whereas CSP systems operate at mid and high temperatures [1.8]. The application of this thesis is focussed on CSP systems.

1.2.1 Parabolic trough systems

The most commonly used CSP system is a linear concentrator that uses parabolic trough collectors. In such a system, the absorber tube is positioned along the focal line of each parabola-shaped reflector as shown in figure 1.2. The tube (solar field piping) is fixed to the mirror structure, and the heated fluid either a heat-transfer fluid or water/steam flows through and out of the field of solar pipes to where it is used to create steam [1.9]. And in the case of a water/steam receiver, it is sent directly to the turbine.

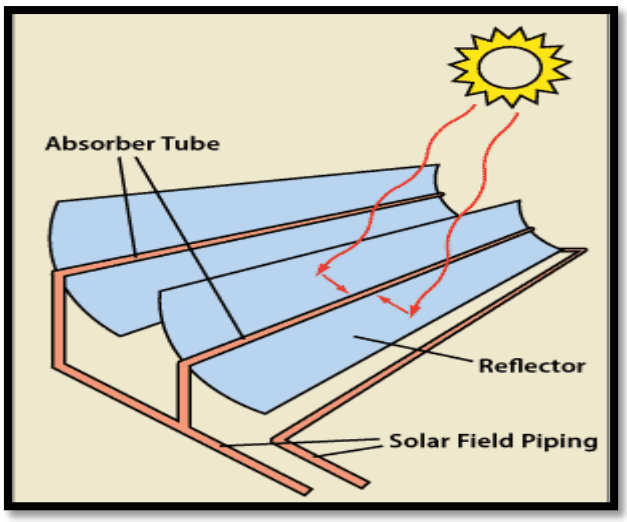

Figure 1.2: Schematic of parabolic trough system [1.9].

1.2.2 Dish system

Dish systems, the most powerful collector, use dish-shaped parabolic mirrors as reflectors to concentrate and focus the sun's rays onto a receiver, which is mounted above the dish at the dish center see figure 1.3 [1.10]. This system works by collecting and concentrating the sun's energy with a dish shaped surface onto a receiver that absorbs the energy and transfers it to the engine. The engine then converts that energy to heat. The heat is then converted to mechanical power, in a manner similar to conventional engines, by compressing the working fluid when it is cold, heating the compressed working fluid, and then expanding it through a turbine or with a piston to produce mechanical power. Finally an electric generator converts the mechanical power into electrical power.

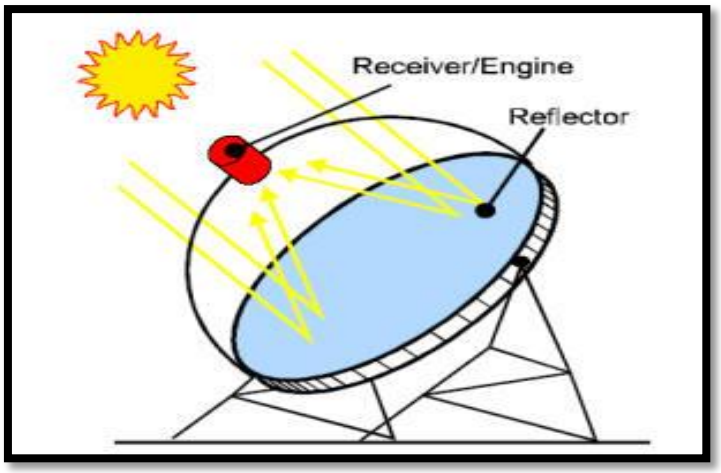

Figure 1.3: Schematic of solar dish system [1.10].

1.2.3 Central receiver system

Central receivers (power towers) use thousands of individual sun-tracking mirrors called "heliostats" to reflect solar energy onto a receiver located on top of a tall tower as shown in figure 1.4. The receiver collects the sun's heat in a heat-transfer fluid (molten salt) that flows through the receiver [1.11]. The salt's heat energy is then used to make steam to generate electricity in a conventional steam generator, located at the foot of the tower.

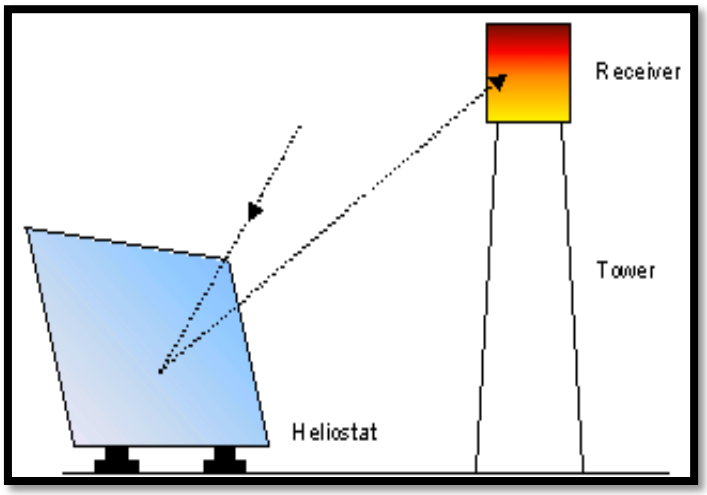

Figure1.4: Schematic of central receiver system [1.11].

Only these collectors are not efficient to cover the ever increasing demand of energy. Hence in order to increase their efficiency, adding spectral selective materials is vital. .

1.3 CHARACHTERSTICS OF SPECTRAL SELECTIVITY

Spectrally selective absorbers used in solar collector are the most important and critical to improve the efficiency of photo-thermal conversion. The optical properties of these surfaces are such that they possess high solar absorptance (α) over the solar spectrum (0.3-2.5μm) region to maximize the fraction of solar energy transformed to heat, and low thermal emittance (ε) to suppress infrared radiation losses at an operating temperature [1.12, 1.13]. This is realised by low reflectance of absorbing surface in the solar radiation spectrum (nearly zero) and high reflectance (close to one) in the infrared region. For practical reason, a good selective coating features optical properties of α greater than 0.9 and ε less than 0.02 [1.14]. Selective coating is defined as the ratio of solar absorptance to thermal emittance.

When an incident light strikes on a surface of a solid material, some part of the incident light is reflected, some part is absorbed, and some part is transmitted. Reflection, absorption and transmission are wavelength dependent. Reflectance, $R(\lambda)$, of light, either specular or diffuse depending on the nature of the interface, is the fraction of incident radiation reflected by a surface, absorbance, $A(\lambda)$, is the fraction of incident light that is absorbed by the surface and transmittance , $T(\lambda)$, is the fraction of incident light which passes through the surface. Emittance, $\varepsilon(\lambda)$, is the ratio between light emitted from a surface and from a perfect blackbody, at the same wavelength and temperature. Conservation of energy gives [1.15]:

$$R(\lambda) + A(\lambda) + T(\lambda) = 1 \qquad 1.6$$

where $R(\lambda)$ is the sum of both specular and diffuse reflectance, λ is the wavelength, and T is transmittance.

Using Kirchhoff's law, spectral absorptance can be expressed in terms of total reflectance $R(\lambda)$ for opaque materials where $T(\lambda) = 0$ [1.15]:

$$A(\lambda) = 1 - R(\lambda) \quad \text{and} \quad \varepsilon(\lambda) = A(\lambda) \qquad 1.7$$

The performance of a solar absorber can be characterized by its solar absorptance and thermal emittance. The total normal solar absorptance α is the weight average, weight by solar irradiation, $I_s(\lambda)$ as shown in equation 1.8. The parameter λ_c designates the cut off wavelength, which shows the wavelength at which the optical behaviour changes from absorption to reflection and it is temperature dependent. For high temperature applications (> 400°C), λ_c is set to 2000 nm and the integral limits are fixed at $\lambda_{\min}$ = 300 nm and $\lambda_{\max}$ = 50000 nm [1.16]. In the calculation of the study, AM1.5 solar spectrum, defined by the ISO standard 9845-1(1992) [1.17] was used.

$$\alpha = \frac{\int_{\lambda\min}^{\lambda c} I_s(\lambda)(1 - R(\lambda)d\lambda}{\int_{\lambda\min}^{\lambda c} I_s(\lambda)} \qquad 1.8$$

Unlike solar absorptance, the thermal emittance is a weighted average, weighted by the blackbody radiation, $I_b(\lambda, T)$ for the given temperature, T, as shown in equation1.9. For T = 373 K, λ_c is 2000 nmm. In this study calculation, temperature is chosen as 373 K.

$$\varepsilon = \frac{\int_{\lambda c}^{\lambda\max} I_b(\lambda, T)(1 - R(\lambda))d\lambda}{\int_{\lambda c}^{\lambda\max} I_b(\lambda, T)} \qquad 1.9$$

To evaluate the performance of solar absorber material, the absorptance and emittance are usually combined in the figure of merit *f* called selectivity. High value of *f* indicates high performance, which is defined as:

$$f = \frac{\alpha}{\varepsilon} \qquad 1.10$$

1.4 MECHANISMS OF SPECTRAL SELECTIVITY

Several different kinds of spectral selectivity have been proposed and fabricated for photo-thermal applications [1.18-1.19]. Three main types can be distinguished from a structural point of view: (i) intrinsic, (ii) surface texturing and (iii) tandem. Moreover, tandem selective surfaces can further be classified into three: (i) semiconductor-metal tandems (ii) multilayered absorbers, and (iii) metal – dielectric composite tandem.

1.4.1 Intrinsic absorbers

Intrinsic absorber materials have a single substance in which selectivity is an intrinsic property of the material. However, there are no naturally occurring materials that exhibit intrinsically solar-selective properties, however some roughly approximate selective properties such as transition metals and semiconductors, both need to be greatly modified to serve as an intrinsic absorber. One of the best absorber of this type so far is ZrB_2 [1.20] nevertheless in most cases, the transition from low to high reflectance occurs at too short wavelengths or the cutoff is not step function.

1.4.2 Surface texturing

Spectral selectivity can be obtained by properly textured surfaces such as needle-like, dendrite, or porous microstructures on the same scale as the wavelength of the incident radiation. When

light strikes on these kinds of surfaces some are absorbed and some are reflected. The reflected light is then absorbed after multiple reflections while appearing highly reflective and mirror-like in the long wavelength region. Textured copper, nickel and stainless steel surfaces are well known examples [1.21]. Lithography with X-rays, Ion-exchange reactions between metals, Vapour-liquid-solid (VLS) mechanism are among other methods to prepare textured microstructures.

1.4.3 Tandems absorbers

Solar selectivity using a single-phase bulk material was hard; hence interest was focused on two layer structures. These tandem absorbers consist of two different surfaces, each with unique optical properties. Together they can exhibit a far greater spectral selectivity compared to what an intrinsic absorber could theoretically achieve. The simplest way to obtain the desired optical properties is to design semiconductor-metal, multilayered absorbers, and metal – dielectric composite tandems as shown below in Figure 1.8.

1.4.3.1 Semiconductor-metal tandems

Semiconductors with the band gap E_g of 0.5 eV able to create high quality of solar absorber in which all the incoming solar radiation is absorbed in the short wavelength λ (< 2.5μm). The largest obstacle to common semiconductors is that, most of them have too large band gaps, corresponding to too short wavelengths. However, lead sulphide, PbS, is a suitable semiconductor with a band gap of 0.4 eV [1.22].

1.4.3.2 Metal-dielectric composite tandems

Metal-dielectric composites are fine-grained metallic particles in an insulating host matrix and are transparent in the thermal IR region, while they are strongly absorbing in the solar region due to the interband transition in the metal and the small particle resonance [1.23]. Hence to

enhance the solar selectivity, composite films can be deposited onto a highly reflective substrate to provide high reflectivity in the IR region and covered with antireflection to minimize radiation loss.

1.4.3.3 Multilayer tandems

An efficient spectrally selective absorbing surface can easily be tailored by using a multilayer design. A multilayer is constructed out of several alternate layers of semitransparent metal and dielectric materials as show in Figure 1.8c. Light absorption in this type is due to the multiple reflection and destructive optical interferences of light passes through the dielectric portion of the stack lying between the two reflective semitransparent layer, which should be in the range of 5-10 nm thick. The semitransparent metallic layer reflects high in the IR region and less in the visible; therefore the dielectric layers are engaged in reducing the visible reflectance from the surface. Generally, selectivity determines by the appropriate thickness of the dielectric layers, which determines the shape and the position of the reflectance curve.

So far Multilayer absorbers using metals such as Mo, Ag, Cu, Ni and dielectric layers Al_2O_3, SiO_2, CeO_2, and ZnS have been studied for high temperature applications [1.24]. In particular, Al_2O_3/ Mo/ Al_2O_3 multilayer absorber appeared to be selective and stable at high temperature, which is ideal for high temperature CSP systems. Hence it is worth to mention that it is important to choose materials having peculiar optical and thermal properties for this kind of design for high temperature applications.

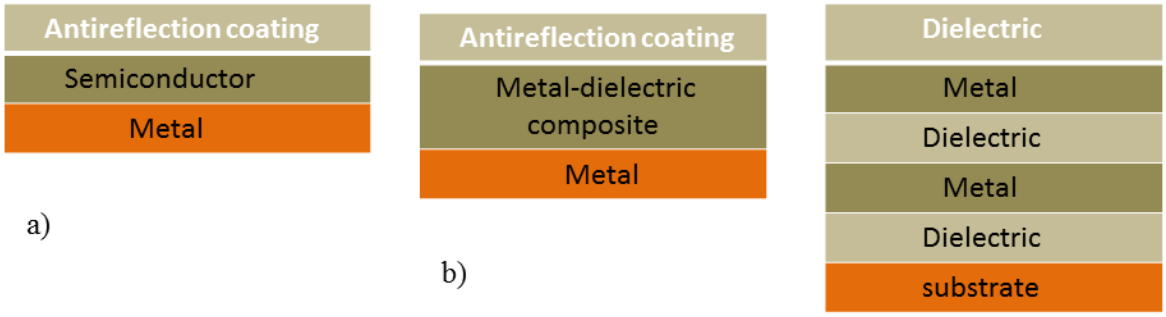

Figure 1.8: Schematic design of tandem absorber film structures: a) semiconductor-metal tandems b) metal-dielectric absorber and c) multilayer absorber

1.5 OPTICAL PROPERTIES OF SOLIDS

As any optical phenomenon is connected with the interaction of electromagnetic radiation with matter, it is worth to understand the basic electromagnetic wave theory for the well-designed spectrally selective absorbing surfaces. The section below describes how electromagnetic waves interact with matter in thin films.

1.5 1 Relationship of optical constants and absorption

The velocity of propagation of an electromagnetic wave through a solid is given by the frequency-dependent complex refractive index:

$$N = n \pm ik, \qquad 1.11$$

where the real part, n is related to the velocity, and k, the extinction coefficient is related to the decay, or damping of the oscillation amplitude of the incident electric field. The optical properties of the solid are therefore governed by the interaction between the solid and the electric field of the electromagnetic wave where $\mu=\mu_o$.

If a plane wave of frequency f propagates through a solid with velocity v in a direction defined by x, the electric field E is described by the following progressive wave equation:

$$E = E_o e^{\left[2\pi f\left(t - x/v\right)\right]} \qquad 1.12$$

where, E_o is the incident electric field vector and $2\pi f\left(t - x/v\right)$ is the displacement at time t after a disturbance, created by the electric field at a point situated at x along the line of propagation.

From Maxwell's equations on electromagnetic theory, the speed of light in a vacuum C is related to the permittivity of free space ε_o, (the degree to which a medium can resist the flow of charge, defined by the ratio of the electric displacement to the intensity of the electric field that produces it), and the permeability of free space μ_o (the ratio of the magnetic flux density in a solid to the external magnetic field strength inducing) is expressed by

$$C = \frac{1}{\sqrt{\mu_o \varepsilon_o}} \qquad 1.13$$

The velocity of propagation through the solid of complex refractive index, $N = n \pm ik$ is related to the speed of light in a vacuum, C, by , $v = c/N$ as

$$\frac{1}{v} = \frac{n}{c} - \frac{ik}{c} \qquad 1.14$$

Therefore, substituting $1/v$ into equation 1.12 gives:

$$E = E_o \exp i2\pi ft \exp\left[\frac{-i2\pi xn}{c}\right]\exp\left[\frac{-2\pi fkx}{c}\right] \qquad 1.15$$

where the last exponential term is the measure of the damping factor or extinction coefficient k.

The power (P) or intensity of an incident wave through a solid is the conductivity (σ) of the solid multiplied by the square of the electric field vector $P = \sigma E^2$. Using the damping factor term, the fraction of the incident power that has propagated from position (*0*) to a distance (x) through the material with conductivity (σ) is given by:

$$\frac{P(x)}{P(0)} = \frac{\sigma E^2(x)}{\sigma E^2(0)} = \exp\left[\frac{-4\pi f k x}{c}\right] \qquad 1.16$$

from which the absorption coefficient (α) can be expressed in terms of the extinction coefficient as:

$$\alpha = \frac{4\pi f k}{c} \qquad 1.17$$

The velocity of light in a vacuum is $C = f\lambda$, then $\alpha = \frac{4\pi k}{\lambda}$, and the power or intensity is $P = P_o \exp -\alpha x$ which is known as Lambert's law of absorption, by which radiation is absorbed to an extent that depends on the wavelength of the radiation and the thickness and nature of the medium.

Due to Maxwell's equations, the complex dielectric function is related to the complex index of refraction in a non-magnetic medium by

$$\varepsilon = N^2 \qquad 1.18$$

The real and imaginary parts of the dielectric function ε are given by:

$$\varepsilon = \varepsilon_1 + i\varepsilon_2 = (n \pm ik)^2 \qquad 1.19$$

One obtains $n \pm ik$ by choosing the form of the plane-wave solution to Maxwell's equations as $\exp(\pm(\omega t \pm q.r))$ .This choice also determines signs in the Lorentz-Oscillator formula for lattice vibrations. We have chosen the tabulated n and k because it is then an easy matter to

obtain the relations of equation 1.20 as well as the intensity based reflectivity *R* (equation 1.21):

$$\varepsilon_1 = n^2 - k^2 \qquad \text{and} \qquad \varepsilon_2 = 2nk \qquad 1.20$$

Generally, the real part of the refractive index relates to the phase of the wave, the imaginary part describes a damping of the amplitude in the direction of propagation and the dielectric function is more suited when we describe the microscopic effects inside a solid. For the normal incidence, the reflectivity is [1.25]:

$$R = \left|\frac{1-N}{1+N}\right|^2 = \frac{(1-n)^2 + k^2}{(1+n)^2 + k^2} \qquad 1.21$$

1.5.2 Lorentz model of non-conducting materials

Near the beginning of the last century H. A. Lorentz developed a classical theory of optical properties in which the electrons and ions of matter were treated as a simple harmonic oscillator subject to the driving force of applied electromagnetic fields.

The classical Lorentz model [1.26] of dielectric dispersion due to resonance polarization is of fundamental importance in optics. It provides a physically appealing, accurate description of both normal and anomalous dispersion phenomena in the extended optical region of the electromagnetic spectrum from the far infrared up to the near ultraviolet. It expresses the complex dielectric constant as a function of material parameters, such as resonance frequency, damping constant, and plasma frequency as it is stated below [1.27].

In non-conducting solids the electrons are localized by being bound to individual atoms as they are not free to move through the lattice. When bounded electrons interact with electromagnetic field, they generally oscillate around their equilibrium position. These phenomena can be described in quantum mechanics as electrons transfer between one energy states to another. But classically, it could approximate the oscillation by a damped oscillator. As it is known a damping force exists due to various collision processes such as electron-electron interaction, electron-lattice interaction and others to extract energy. There are several forces acting on an oscillator: driving force, spring force and damping force are among others.

Newton's second law gives us:

$$m\ddot{x} = -\beta\dot{x} - k_s x - eE_x \qquad 1.22$$

Since the electrical field is harmonic, $E_x = E_o \exp - i\omega t$ and the above equation can be rewritten as:

$$\ddot{x} + \gamma\dot{x} + \omega_o^2 x = -eE_o e^{-i\omega t/m} \qquad 1.23$$

where γ is the dumping constant, ω_o is the resonance frequency, e is the electron charge, m is the mass of the electron, and E_o is the incident electric field. The quantity γ describes the energy dissipation property of the medium and ω_o describes the ability of the medium to store energy.

To solve the above equation, let's assume

$$X(t) = Ae^{-i\omega t} \qquad 1.24$$

Substituting equation 1.23 into 1.22 and solving for A gives us

$$A = -\frac{eE_o}{m}\left(\frac{1}{\omega_o^2 - \omega^2 - i\gamma\omega}\right) \quad \text{and} \quad x(t) = \frac{eE_o}{m}\left(\frac{e^{-i\omega t}}{\omega_o^2 - \omega^2 i\gamma\omega}\right) \qquad 1.25$$

The induced dipole moment due to the charge displacement is given by:

$$P(t) = -e.x(t) \qquad 1.25$$

The induced polarization vector P is given by:

$$P = Np \tag{1.27}$$

where N is the number of charge dipoles per unit volume in the material. Assuming that all induced dipoles are parallel within the volume, the induce polarization through the volume is given by:

$$P(\omega) = \frac{N_o e^2 E_o}{m} \cdot \frac{e^{-i\omega t}}{\omega_o^2 - i\gamma\omega - \omega^2} = \frac{\omega_p^2}{\omega_o^2 - i\gamma\omega - \omega^2} \varepsilon_o E \tag{1.28}$$

where

$$\omega_p^2 = \frac{N_o e^2}{m\varepsilon_o} \tag{1.29}$$

ω_p is called resonance frequency.

The polarization vector characterizes the polarization density of the medium under the influence of the electric field and it excludes the vacuum contribution. Hence one can expect the polarization of the material to be proportional to the strength of the electric field.

$$\mathrm{P} \propto E \rightarrow \mathrm{P} = \varepsilon_o x E \tag{1.30}$$

The constant of proportionality x is called the electrical susceptibility of the material such that x is stated above and the relative dielectric constant $\varepsilon = \varepsilon_o \varepsilon_r$ is; $\varepsilon_r = x + 1$.

Substituting this value of x, the complex permeability is then given by:

$$\varepsilon_r = \varepsilon_r^{'} + i\varepsilon_r^{''} \tag{1.31}$$

where the real and imaginary parts are:

$$\varepsilon_r^{'} = 1 + \frac{\omega_p^2(\omega_o^2 - \omega^2)}{(\omega_o^2 - \omega^2)^2 + \gamma^2\omega^2} \quad \text{and} \quad \varepsilon_r^{''} = 1 + \frac{\omega_p^2 \gamma\omega}{(\omega_o^2 - \omega^2)^2 + \gamma^2\omega^2} \tag{1.32}$$

Classically, ω_o is the resonance frequency of the simple harmonic oscillator but Quantum mechanically; it is the difference in energy between the final and the initial states.

To further understand the physical insight, it is important to discuss the different frequency regions. When the response is below resonance, the frequency ω is less than ω_o $(\omega \ll \omega_o)$, equation 1.31 is reduced to:

$$\varepsilon_r^{'} = 1 + \frac{\omega_p^2}{\omega_o^2} \cdot \frac{1}{1 - 2\left(\omega / \omega_o\right)^2} \quad \text{and} \quad \varepsilon_r^{''} = \frac{\omega_p^2 \gamma \omega}{\omega_o^4} \cdot \frac{1}{1 - 2\left(\omega / \omega_o\right)^2} \qquad 1.33$$

Since $\gamma \ll \omega_o^2$, the real part is less than imaginary part $(\varepsilon_r^{'} < \varepsilon_r^{''})$. Hence in such cases absorption is negligible, below the resonance, which implies that the material is transparent. At resonance $(\omega = \omega_o)$ the frequency ω is comparable to ω_o equation 1.33 is rewritten as:

$$\varepsilon_r^{'} = 1 + \frac{\omega_p^2}{2\omega_o} \cdot \frac{\omega - \omega_o}{1 + \left(\frac{\omega - \omega_o}{\gamma / 2}\right)^2} \quad \text{and} \quad \varepsilon_r^{''} = \frac{\omega_p^2}{2\omega_o} \cdot \frac{\gamma / 2}{1 + \left(\frac{\omega - \omega_o}{\gamma / 2}\right)^2} \qquad 1.34$$

Under these conditions, the absorption is significant i.e. $\omega - \omega_o < \gamma$ and the absorption line has a characteristic shape, Lorentzian line. This shape has a central frequency ω_o and a full width half maximum of γ. While ω_o has a physical significance of the frequency at which the system "resonates", or absorbs strongly. Moreover in case of above resonance $(\omega \gg \omega_o)$ equation 1.32 is reduced to:

$$\varepsilon_r^{'} = 1 + \omega_p^2 \cdot \frac{\omega^2}{\omega^4 + \gamma^2 \omega^2} \quad \text{and} \quad \varepsilon_r^{'} = 1 + \omega_p^2 \cdot \frac{\omega^2}{\omega^4 + \gamma^2 \omega^2} \qquad 1.35$$

In these cases the absorption becomes less significant, as expected in a frequency range away from the resonance.

The response of Al_2O_3 is well described by the Lorentz oscillatory model with narrow resonant absorption located suitably above the UV [1.28]. Fig 1.9 illustrates the optical constants (*n*, *k* and obtained bulk reflectance *R*) of Al_2O_3 in the UV-VIS-NIR region [1.29]. One can observe that the refractive index is greater than the extinction coefficient where the extinction coefficient is zero. This feature depicts the transparency of the material.

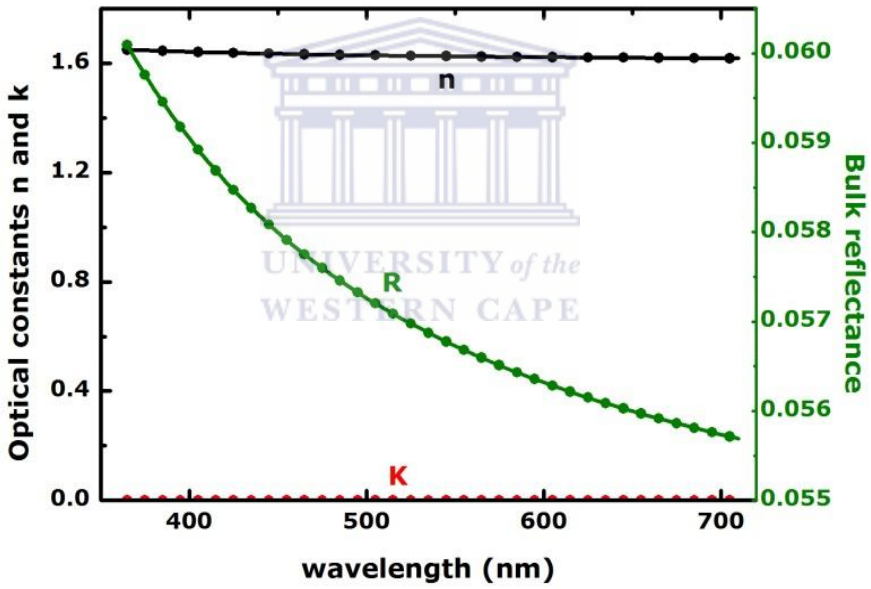

Figure 1.9 Optical properties (*n*, *k*, and normal bulk reflectance *R*) of Aluminum oxide as function of wavelength

1.5.3 Drude Model of conducting materials

The Drude model was developed at the turn of the 20th century by Paul Drude to explain the transport properties of electrons in material particularly in metals. The complex dielectric

constant of free-electron in metals can be obtained by the Drude model as a function of plasma frequency and relaxation time as briefly shown below [1.30].

In conductive materials, the restoring $m\omega_o^2 x$ force vanishes, establishing that the charge can move freely. Under these conditions, from Lorentz model one can obtain Drude's model $(\omega_o^2 \to 0)$, in which equation 1.35 reduces to:

$$\varepsilon_r^{'} = 1 - \frac{\omega_p^2}{\omega^2 + \gamma^2} \quad \text{and} \quad \varepsilon_r^{'} = \frac{\omega_p^2}{\omega} \cdot \frac{\gamma}{\omega^2 + \gamma^2} \qquad 1.36$$

Generally, $\gamma = 1/\tau_{col} \langle \omega$, the frequency of collisions is much lower than that of optical frequencies. If the optical frequency is greater than plasma frequency $(\omega \rangle \omega_p)$, we can see that $\varepsilon_r^{''} \to 0$ this indicates that the imaginary part of the complex refractive index vanishes $(\kappa \to 0)$. In addition at high frequency, there is no absorption so that the metal becomes transparent. The reason is that at this frequency, the electrons in the metal cannot react fast to the incident electrical field.

The plasma frequency of metals typically lies in the visible or ultraviolet spectral region in which the reflectance shows a dramatic drop starting at the wavelength corresponding to plasma frequency towards increasing wavelength. Fig 1.10 illustrates the optical constants along with the bulk reflectance of platinum in the UV-VIS-NIR region.

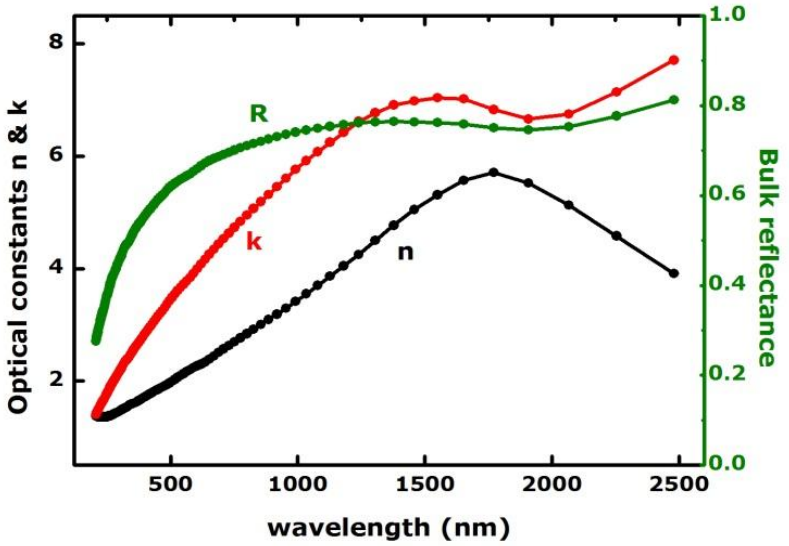

Figure 1.10 Optical properties (*n*, *k*, and bulk reflectance *R*) of Platinum illustrated as function of wavelength.

As it can be seen from figure 1.10, The reflectance in the solar range shows a noticeable slope towards short wavelengths, and this is caused by low energy interband transitions among the d electrons [1.31] and the optical properties (*n*, and *k*) of Platinum [1.29] illustrates that $n > 0$, or $k > n > 0$, which results in negative real dielectric constant indicating that light is rejected by metals.

1.6 MULTILAYER REFLECTION

It was mentioned in section 1.3 that a fraction of light is reflected from the surface which can be a single or more layers. A branch of optics that deals with very thin structured layers of different materials is called thin film optics. In order to exhibit thin-film optics, the thickness of the layers of material must be of the order of the wavelengths of visible light (about 500 nm).

Layers at this scale can have remarkable reflective properties due to light wave interference and the difference in refractive index between the layers, air, and substrate.

The reflection of a multilayer consisting of several thin, flat and homogeneous films with known optical constants can be calculated typically according to the matrix method [1.32]. However, for two- and three-layer thin films, it is more convenient to use a summation method by extending equations used in the single layer case as shown below.

For a single homogeneous thin film, two boundaries are considered for the optical behavior. The numbering of the boundary adheres to the convention of optical multilayer, i.e. counting from the top to the substrate. Thus, complex amplitude reflection on the first (air/thin film) and second (thin film/substrate) boundaries are presented as r_1, r_2 in equation (3.37), (1.38) assuming semi-infinite of materials exists on both sides is given as [1.30]:

$$r_1 = \frac{N_o + N_1}{N_o + N_1} \qquad 1.37$$

$$r_2 = \frac{N_1 - N_2}{N_1 + N_2} \qquad 1.38$$

where N_o, N_1, N_2 are the complex optical constants of air (vacuum), thin film, and substrate material respectively. The complex amplitude reflection of such homogeneous thin film is expressed in equations (1.39) [1.30].

$$r = \frac{r_1 + r_2 e^{-2i\delta_1}}{1 + r_1 r_2 e^{-2i\delta_1}} \qquad 1.39$$

The change in phase is given by:

$$\delta_1 = -\frac{2\pi}{\lambda} N_1 d_1 \qquad 1.40$$

Where d_1 is the film thickness, λ is the wavelength and the term $e^{-2i\delta_1}$ contains phase shift information and is further expressed by

$$e^{-2\delta_1} = \exp -4\pi k_1 \cdot d/\lambda \left[\cos\left(4\pi \cdot n_1 d/\lambda\right) + i\sin\left(4\pi . n_1 d/\lambda\right)\right] \quad 1.41$$

In the above equation (1.41), the factor $4n_1 d/\lambda$ controls the periodicity of sine, cosine functions, which determine thin film interference property.

For double layers, there are three interfaces. Equation (1.37), (1.38) is extended to the third interface having amplitude reflection:

$$r_2 = \frac{N_2 - N_3}{N_2 + N_3} \quad 1.42$$

Similarly, the phase change in layer 2 is expressed as:

$$\delta_2 = -\frac{2\pi}{\lambda} N_2 d_2 \quad 1.43$$

Starting from the base layer, i.e. layer 2, the total reflected amplitude between boundary 2 and 3 is (compared with equation (1.40)):

$$r_{L2} = \frac{r_2 + r_3 e^{-2i\delta_2}}{1 + r_2 r_3 e^{-2i\delta_2}} \quad 1.44$$

Then the total reflection of double layer can then be obtained by replacing r_2 with the term r_{L2} in equation (1.44),

$$r = \frac{r_1 + r_{L2} e^{-2i\delta_1}}{1 + r_1 r_{L2} e^{-2i\delta_2}} \quad 1.45$$

Following the same procedures from the above equations to three layers the total reflection obtained can be calculated by:

$$r = \frac{r_1 + r_{L3} e^{-2i\delta_1}}{1 + r_1 r_{L3} e^{-2i\delta_1}} \quad 1.46$$

1.7 AIMS AND OUTLINE

Currently the world relies on fossil fuels to produce 86% of its energy. However, the consumption of fossil fuels generates green-house gases, a major factor responsible for global warming [1.33].The importance to overcome our dependence on fossil fuels is becoming more and more evident. The enhancement of environmental of environmental problems on the one hand and the increasing need of the energy motivated people to look for alternative energy resources [1.34]. Significant effort needs to be invested in the development of inexpensive and efficient light-harvesting materials. This leads to utilize solar energy [1.34], wind and hydrogen energy [1.35], biomass energy [1.36], and other renewable energy technologies.

The primary component of a solar power system is the photovoltaic systems. Photovoltaic devices use semiconducting materials to convert sunlight directly into electricity (quantum conversion) and are a cost effective method for many applications [1.37]. At the same time, the technology of solar-thermal conversion becomes mature and cost-competitive, which convert solar radiation into heat (thermal conversion). Solar- thermal devices are used to heat water at lower temperatures ($T < 400^{o}C$) and to produce steam for electricity generation at high temperatures ($> 400^{o}C$) [1.38]. Like many others, the application of these devices depends on the progress of the materials used in the components of the collectors. For this reason, most solar collectors use a spectrally solar selective surface, which has high absorption of solar radiation in the solar spectrum region and minimum thermal radiation losses in the infrared region [1.39].

Currently most spectrally solar selective coatings degrade at high temperature due to corrosion, oxidation, and inter-diffusion. However, some efficient photo-thermal conversion is obtained at

higher temperatures. One of the most promising materials for high temperature application is multilayer of $Al_2O_3/Pt/Al_2O_3$ coatings.

The main objective of this work is to provide an improved spectrally solar selective multilayer coating prepared by electron beam vacuum evaporation, which has high solar absorptance in the solar spectrum region, low thermal emittance in the infrared region, and thermally stable above 400^{o}C in air for high temperature solar-thermal power applications.

The remain of the thesis is organized as follows:

Chapter two will focus on optimization and deposition of $Al_xO_y/Pt/Al_xO_y$ multilayer spectrally solar selective coatings using an ellipsometric measurements and optical simulation, as well as determination of optical constants of each layer.

The microstructural and optical properties of the optimized and deposited $Al_xO_y/Pt/Al_xO_y$ multilayer solar absorber coatings are presented in *chapter three*.

Chapter four reports on the effect of thermal annealing on the structural, compositional and optical properties of an electron beam evaporated $Al_xO_y/Pt/Al_xO_y$ multilayer solar absorber coatings. Special focus is given to the optical properties of the solar absorber coatings annealed in air for short and long durations in order to evaluate its spectral selectivity.

Chapter five will continue this trend to assess the changes in the depth profile of $Al_xO_y/Pt/Al_xO_y$ multilayer solar absorber coatings, which demonstrates the main cause for the degradation of the solar absorber coatings above 500^{o}C in air.

To improve the thermal stability of $Al_xO_y/Pt/Al_xO_y$ multilayer solar absorber coatings beyond 500^oC, a tantalum diffusion barrier layer is used. Structural, compositional, optical properties and thermal stability are carried out in *chapter six*.

Finally, a *summary* of the thesis will be presented.

1.8 REFERENCES

1.1 S. Blundell, K. Blundell ‘‘Concepts in Modern Physics’’, Oxford University Press. ISBN 78-019-856769-1(2006) 247.

1.2 M. Planck, ‘‘Theory of the heat radiation’’ English transition of Theorie der Wärmestrahlung, 2nd edi, New York (1913).

1.3 J. Blatt, Frank, ‘‘Roots of the Quantum Theory in Modern Physics’’, McGraw-Hill Inc. New York (1991) 71.

1.4 J. Blatt, Frank, ‘‘Roots of the Quantum Theory in Modern Physics’’, McGraw-Hill, Inc. New York, (1994) 71.

1.5 M. Iqbal, ‘‘an Introduction to Solar Radiation, Academic Press’’, Canada (1983).

1.6 A. John. Duffie, A. William. Beckman, ‘‘Atmosphere attenuation of solar radiation in Solar Energy of Thermal Process’’, John Wiley & Sons, New York, (1991) 7-10, and 64-68.

1.7 Zakia. Sen, ‘‘Solar Energy Fundamentals and Modeling Techniques: Atmosphere, Environment, Climate change and Renewable Energy ’’ Springer, (2008) 245.

1.8 C. E. Kendy, ‘‘Review of Mid-High temperature solar selective absorber’’, NREL/TP-520-31267, (2002).

1.9 G. C Bankos, D. Adamopoulos and N. F Tsagas, ‘‘Design and construction of a line-focus parabolic trough solar concentrator for electricity generation’’, ISES Solar World Congress Vol III (1999).

1.10 Robert Foster, Majid Ghassemi, Alma Cota, ‘‘Soalr Energy: Renewable Energy and the Environment’’ CRC Press (2010) 94.

1.11 John A. Duffie and William A. Beckman, ‘‘Solar engineering of thermal process’’, John and Wiley & Sons, INC (1980).

1.12 B. O .Seraphin, in: B. O. Serphin (Ed.), ‘‘Solar Energy Conversion-Solid State Physics

aspects, Topics in Applied Physics'', 31, Springer, Berlin, (1979).

1.13 C. G. Niklasson, C. G. Granqvisit, J. Mater. Sci. 18 (1983) 3475.

1.14 A. Andersson, O. Hunderi, C. G. Granqvisit, J. Appl. Phys. 51 (1980) 754.

1.15 W. L. Wolfe and G. J. Zissis, ''The infrared hand book, Environmental Research Institute of Michigan'', Washinton DC, (1989).

1.16 R. Kirchner, M, Ch. Lux-Steiner, E. Liebemann, E. Bucher, Solar Energy materials & Solar Cells 33 (1994) 453.

1.17 E. Wäckelgård, G. Hultmark, Solar Energy Materials & Solar Cells, 54 (1998) 165-170.

1.18 C. G. Granqvist, G. A. Niklasson Phys. Rev. B 18 (1978) 554.

1.19 G. A. Niklasson, C. G. Granqvist J. Appl. Phys. 55 (1984) 3382.

1.20 B. O. Seraphin, Thin Sold Films **90** (1982) 395-403.

1.21 G. L. Harding, M. R. Lake, Solar Energy Materials, 5 (1981) 445-464.

1.22 O. P. Agnihotri, B.K. Gupta, ''Solar Selective Surfaces'', John Wiley & Sons, New York (1981).

1.23 R. A. Buhrman, H. G. Craighead, ''Composite Film Selective- Absorbers, in Solar Materials Science'', Academic Press, New York, (1980) 277-292

1.24 A. Andersson, O. Hunderi, and C. G. Granqvist, J. Appl. Physics, 51 (1980) 754.

1.25 O.S Heavens, ''Optical properties of thin solid films'', Dover Publications, New York, (1991).

1.26 H. A. Lorentz, ''Versuch einer Theorie der Electrischen und Optischen Erscheinungen'' in Bewegten Körpern, (1906).

1.27 Frederick Wooten, ''Absorption and Dispersion, in Optical Properties of Solids'', Academic Press, New York (1972) 42-55.

1.28 R. Howard. Huff, C. Gilmer David , ''High dielectric materials: VLSIMOSFET applicatrions'', Springer, (2005),5051.

1.29 E. D. Palik , ‘‘Hand book of optical constants of Solids III’’, Academic press, USA, (1998), 641.

1.30 Shiuzi Zaoh, ‘‘Spectrally Selective Solar Absorbing Coatings Prepared by dc Magnetron Sputtering’’, ISSN 1651-6214, (2007).

1.31 H. Ehrereich, H. R. Philipp, D. J. Olechna, Physical Review, 131 (1963) 2469-2477.

1.32 O. S. Heavens, ‘‘Thin Film Optics, in Optical Properties of Thin Solid Films’’, Dover publications, Inc., New York (1954) 46-50.

1.33 M. A. Signore, A. Sytchkova, A.Rizzo, J. Opti. Mat. 34 (2011) 292-297.

1.34 M. S. Dresselhaus, I. L. Thomas, Natural gas, 21, (2001)19-29.

1.35 J. M. Carrasco, L. G. Franquelo, J. T. Bialasiewicz, E. Galván, R. C. P. Guisado, M. A. M. Prats. Industrial Electronics, IEEE Transactions on 53 (2004), 1002-1016.

1.36 P. McKendry, Bioresour. Technol., 83, 37-46 (2002).

1.37 H. A. Ossenbrink, ‘‘Futue research and development in photovoltics in the future forrenewable Energy II’’, edited by EUREC Agency, (2005).

1.38 C. E. Kenndy, ‘‘Review of mid- to high-temperature solar selective absorber materials’’; (2002). NREL/TP-520-31267.

1.39 G. A. Niklasson, C. G. graqvist, J. Mater. Sci. 18 (1983) 3475-3534.

CHAPTER TWO

OPTIMIZATION OF $Al_xO_y/Pt/Al_xO_y$ MULIT-LAYER SPECTRALLY SELECTIVE COATINGS FOR SOLAR-THERMAL APPLICATIONS

ABSTRACT

Spectrally selective $Al_xO_y/Pt/Al_xO_y$ multilayer absorber coatings were deposited onto corning 1737 glass, Si (111) and copper substrates using electron beam (e-beam) vacuum evaporator at room temperature. The employment of ellipsometric measurements and optical simulation was proposed as an effective method to optimize and deposit multilayer solar absorber coatings. The optical constants (n and k) measured using spectroscopic ellipsometry, showed that both Al_xO_y layers, which used in the coatings, were dielectric in nature and the Pt layer was semi-transparent. The optimized multilayer coatings exhibited high solar absorptance α ~ 0.94±0.01 and low thermal emittance ε ~ 0.06 ± 0.01 at 82^{o}C.

The content of this chapter was published in: vacuum 86 (2012) 2129-213

2.1 INTRODUCTION

Spectrally selective absorber surfaces, used in solar collector, are the most important and critical to improve the efficiency of photothermal conversion. The optical properties of these surfaces are such that they possess high solar absorptance (α) over the solar spectrum (0.3-2.5 μm) region to maximize the fraction of solar energy transformed to heat, and low thermal emittance (ε) to suppress infrared radiation losses at an operating temperature [2.1, 2.2]. This is realized by low reflectance of an absorbing surface in the solar main irradiation spectrum (nearly zero) and high reflectance (close to one) in the infrared region. For practical reason, a good selective coating features optical properties of α greater than 0.9 and ε less than 0.02 [2.3].

Recently, selective absorbing surfaces based on semiconductormetal tandems and metal-dielectric composites have been reported by several authors [2.4-2.11]. However, multilayer absorbers based on metallic oxide coatings such as Cr_2O_3, MoO_3, WO_x, HFO_2, Al_2O_3 etc. have also attracted considerable attention due to their optical properties and good thermal stability [2.1].

The optical properties of transition metal based coatings can be tailored by controlling the stoichiometry, which affects the density of free electrons in the d band [2.12]. Among transition metal oxides, especially aluminium oxide (Al_2O_3) coatings are technologically important because of its high hardness, excellent dielectric properties, refractoriness and good thermal properties.

Nobel metals such as Pt (VIIIB), Ir (VIIIB), Au (IB), Pd (VIIIB) etc., metals of group VIIB, VIII, IB of the second and third transition series of the periodic table, are prime candidates for high temperature applications due to their capacity to resist oxidation. However, W, Mo, Os, and Ta have very poor oxidation resistance. And Ag, Al, Cr, and Ni are not suitable for concentrating solar power applications because they diffuse at fairly low temperatures [2.13]. Hence, owing to the peculiar properties of Pt and Al_2O_3, multilayer absorber of $Al_2O_3/Pt/Al_2O_3$ can be fabricated for high temperature solar-thermal applications.

Multilayer absorbers also called 'multilayer interference stacks' essentially consist of thin semi-transparent metal layer between two dielectric layers and can be designed to be efficient spectrally selective surface. Multilayer absorbers using metals such as Mo, Ag, Cu, Ni and dielectric layers Al_2O_3, SiO_2, CeO_2, and ZnS have been studied for high temperature applications [1.13]. $Al_2O_3/Mo/Al_2O_3$ interference type deposited onto stainless steel using cylindrical magnetron sputtering technique showed high solar absorptance of 0.92-0.95 and thermal emittance of 0.06-0.10 at 20^oC [2.14]. Harish C. Barshilia *et al*. [2.15] reported $Cr_xO_y/Cr/Cr_xO_y$ multilayer coatings deposited onto copper substrate using a pulsed sputtering system achieved solar absorptance of 0.88-0.912 with low emittance of 0.05-0.06. They also reported multilayers of $Al_xO_y/Al/Al_xO_y$ interference type deposited onto copper and molybdenum substrates using the same system exhibited high solar absorptance of 0.950-0.970 and low thermal emittance of 0.05-0.08 at 82^oC [2.16]. $HfO_x/Mo/HfO_2$ deposited onto copper and stainless steel using magnetron sputtering system revealed high solar absorptance of 0.905-0.923 and low thermal emittance of 0.15-0.17 at 82^oC [2.17]. However, multilayer absorber using Pt metal and Al_2O_3 dielectric using e-beam vacuum evaporation has not been studied for solar-thermal applications. E-beam vacuum evaporation is a promising method due to the possibility of depositing large area with a large extent contamination-free and no impurities.

In this chapter, we have designed $Al_xO_y/Pt/Al_xO_y$ multilayer absorber coatings with improved optical properties for solar-thermal applications. High vacuum e-beam evaporation was used to deposit the $Al_xO_y/Pt/Al_xO_y$ multilayer absorber coatings onto corning 1737 glass, Si (111) and copper substrates. Phase modulated spectroscopic ellipsometry (SE) spectrophotometry, emissometer and simulation programme were used to characterize the coatings.

2.2 EXPERIMENTAL DETAILS

$Al_xO_y/Pt/Al_xO_y$ multilayer stacks of 700-2000 Å Al_xO_y top layers, 50-100 Å Pt middle layers and 100-600 Å Al_xO_y base layers were deposited onto corning glass (3×3 cm^2), Si (1×2 cm^2) and copper (3×3 cm^2) substrates using a home-made 3 kW high vacuum e-beam evaporator system at a deposition pressure of 10^{-6}mb. Fig. 1 shows the block diagram of the evaporator system. Highly pure, Al_2O_3 pellets (purity 99.999%) (3 mm in diameter) and Pt disc (purity 99.9%) (35 mm in diameter) targets were placed on Cu crucibles for the deposition of the above mentioned films. Prior to deposition, the substrates were cleaned by ultrasonic washing and degreased with methanol, ethanol, and trichloroethylene each for 15 min and finally cleaned using de ionized water.

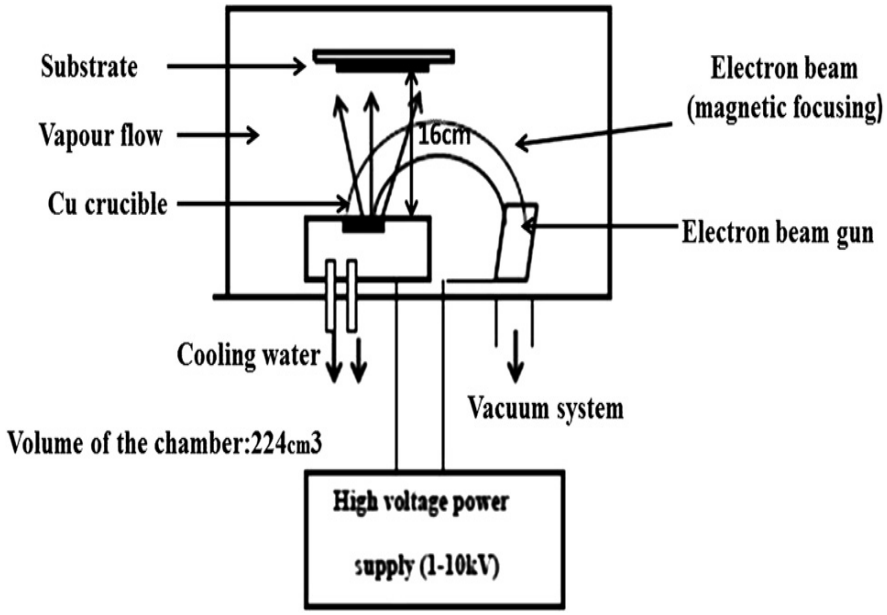

Figure 1: Block diagram of the 3 kV vacuum electron beam evaporation system.

The e-beam current was 20 mA for Al_xO_y layers and 160 mA for Pt layers. E-beam current, determines the rate of the films, and hence the thickness. The thickness of the dielectric layers governs the position of the reflectance curve, which leads to get high solar absorptance and low thermal emittance. The rates and thickness were measured continuously during the evaporation by a quartz crystal monitor. The rate was (1.8 ± 0.6)Å/s and (1.2 ± 0.6) Å/s for Al_xO_y and Pt layers respectively.

For all deposited layers, the values of the refractive index ( ) and extinction coefficient ( ) were determined from the ellipsometeric parameters (Ψ, Δ) obtained from the ratio of Fresnel coefficients for parallel and normal polarization [2.18], which was measured using spectroscopic phase modulated ellipsometery model Jobin-Yvon UVISEL^{TM}. This instrument enables (Ψ, Δ) measurement in the wavelength range of 250-1650 nm. Al_xO_y layers were modeled using Adachi's model [2.19, 2.20]. And the middle Pt layer was modeled using

Cauchy's formula [2.21] for generating refractive indices $n(\lambda)$ and $k(\lambda)$ spectra [2.19, 2.22]. The fitting details are described elsewhere [2.19, 2. 22].

In order to validate the estimations performed by ellipsometric measurements, the reflectance spectrum of each layer and multilayer structure were computed using an optical spectrum simulation program called SCOUT [2.23] with thickness and optical parameters as an input data. This software is used for the analysis of optical spectra by comparison of measurements (reflectance, transmittance, absorptance etc) and models (Tauc-Lorentz interband transition model, user-defined expressions for optical constants, imported dielectric functions, classical Drude model etc). The software uses Fresnel formalism to calculate the reflectance of multilayer films [2.24]. This programme uses a downhill simplex method to minimize the fit deviation, which gives graphics to windows and data to text files as an output.

Subsequently this simulated reflectance was compared with the experimental reflectance obtained by spectrophotometric technique. Diffuse reflectance was collected with a double beam Varian Cary 5000 model internal DRA-2500 spectrophotometer in the wavelength range of 0.3-2.5 μm to calculate solar absorptance using an AM1.5. And a direct measurement of emittance using an emissometer model AE1, which has an accuracy of about ± 0.01 emittance units was used to measure the emissivity of the devices.

2.3 RESULTS AND DISCUSTION

In this experimental work, the final aim consisted of an optimized spectrally selective coating, which has very good photo-thermal performances i.e. high solar absorptance and low thermal emittance at an operating temperature.

Generally, the optimization of a multilayer selective coating consists in the specification of appropriate thickness values related to each of the three layers, which form a spectrally selective coating. In this section we will describe the experimental procedure adopted to choose these parameters in order to fabricate a spectrally selective multilayer coating for solar-thermal applications.

2.3.1 Optical properties of Al_xO_y top layer

In multilayer solar absorbers, the thickness of the dielectric determines the shape and position of the reflectance curve. Hence, in order to get the best step transition reflectance curve at an appreciable wavelength, we deposited a set of Al_xO_y layers onto glass substrates by varying the thickness from 700 to 2000 Å at the following process conditions: e-beam current applied to the target of 20 mA, pressure 10^{-6} mb and growth rate 1.8 ± 0.6 Å/s.

The complex refractive index (N) was estimated by ellipsometric measurements and was modelled using Adachi's model. Ninomiya and Adachi [2.19] relate the energy band structure and imaginary part of the complex dielectric function to derive the dispersion relation for the complex dielectric function of crystalline semiconductor as shown below in Eq. (1).

$$\varepsilon_2(E) = \frac{(e^2\hbar^2)}{\pi\mu^2 E^2}\int dk\left|P_{cv}(k)\right|^2 \delta\left[E_v(k) - E_V(k) - E\right] \qquad 2.1$$

where μ is the combined density of states, the Dirac δ function represents the joint spectral density of state between the valence $E_v(k)$ and the conduction band $E_c(k)$ deferring by the incident light energy $E = \hbar\omega$, $P_{cv}(k)$ the momentum matrix element between valence and conduction band states and evaluated by integration over the first Brillion zone. Eq. (2.1) can

be rewritten in terms of joint density of state function of the S[th] interband critical point $J_{cv}^{s}(E)$ as:

$$\varepsilon_2(E) = \sum_{x=1}^{M} \frac{Ae^2\hbar^2}{\pi\mu^2 E^2} B_{cv}^{5} (E - E_{cv}^{5})^{-2} J_{cv}^{5}(E) \qquad 2.2$$

Since the analytical expressions for different critical points are well defined, Eq. (2.2) is used to obtain the analytical expression for imaginary part of dielectric constant $\varepsilon_2(E)$ at different critical points. Then, by using Kramerse Kronig relation, the real part of the dielectric function $\varepsilon_1(E)$ can be determined; hence the complex dielectric function can then be generated over the spectral range. According to Adachi *et al.* [2.20], the above expression can be applied to amorphous materials by changing the critical point energies. For more detail the reader can refer [2.25].

Fig. 2a shows the generated optical constants of top Al_xO_y layers. It is observed that the real part (*n*) of the different thicknesses is greater than the imaginary part $k(E)$ of the complex refractive index. And the *n* values exhibited maximum at a wavelength of ~ 250-300 nm, and then after decreased with wavelength, whereas *k* values are zero over all wavelength, which indicates the dielectric behaviour. Fig. 2b shows the experimental spectral reflectance obtained from spectrophotometer technique. It is clearly observed that as the thickness of the Al_xO_y layers increase: i) the reflectance in the visible region increases and shifts to higher wavelength, ii) the number of interference in the visible region increases and iii) the sharpness of the transition reflectance curve decreases. These are attributed to an increase in refractive index of Al_xO_y layers in the visible region (see Fig. 2a).

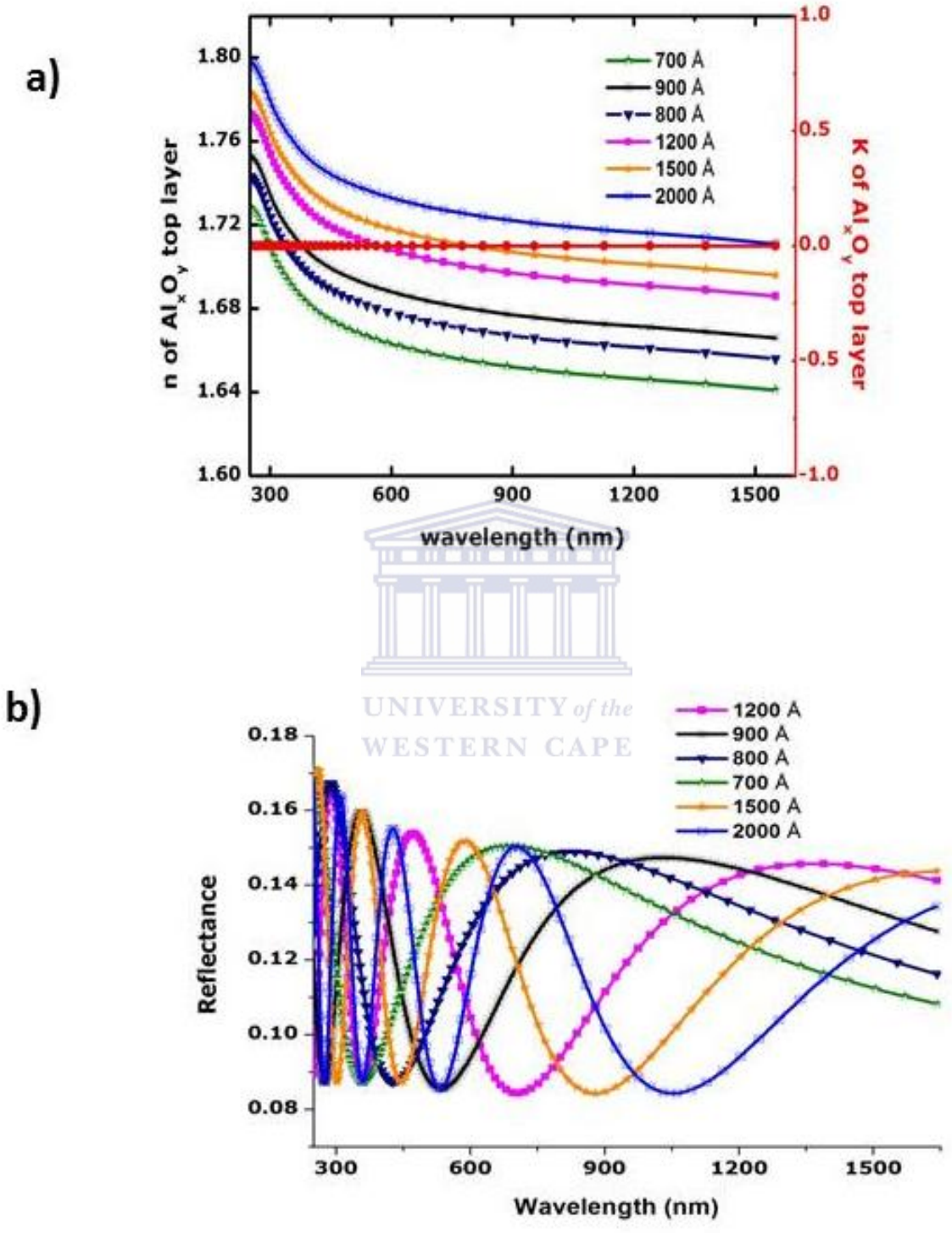

Figure 2: Al_xO_y top layer: a) estimated refractive index *n* and extinction coefficient *k* of different thickness, b) their corresponding reflectance spectra deposited on glass substrate.

Subsequently utilizing the spectral ellipsometric values, was simulated the spectral reflectance, of glass/Al_xO_y and compared it with the experimental spectral reflectance obtained by spectrophotometer technique, as reported in Fig. 3, we can see that the simulated and the experimental curve of glass/Al_xO_y 900 Å thick are in a good agreement. And the same good agreement was obtained for all the other layers, for this reason; we can affirm that the characterization of the top Al_xO_y layer may be considered very careful.

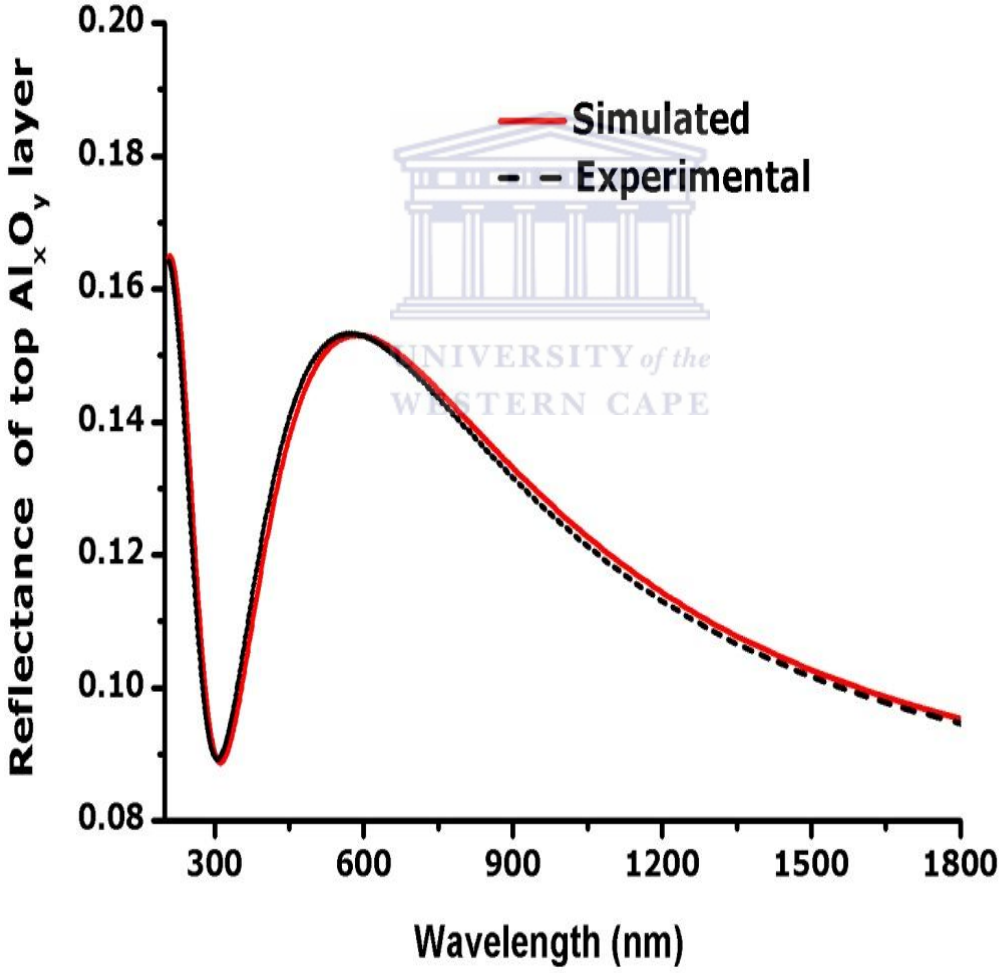

Figure 3: Comparison between the simulated solid red curve and the experimental dashed curve spectral reflectance of Al_xO_y top layer 900 Å thick deposited on glass.

2.3.2 Optical properties of Pt middle layer

In order to evaluate the transparency, as first step we deposited on glass a set of Pt layers by varying the thickness from 50 to 100 Å, starting from the measured transmittance, then we deposited on glass substrate at the following process conditions: e-beam current applied to the target of 160 mA, pressure 2×10^{-6} mb and growth rate 1.2 ± 0.6 Å/s.

Each layer was subjected to ellipsometric measurements in order to estimate the spectral behavior of the complex refraction index $\tilde{N}$. This layer was modelled using Cauchy's formula for generating the refractive indices n and extinction coefficient k spectra. Cauchy's dispersion formula is used to determine (semi) transparent materials given by [2.21]:

$$n(\lambda) = A + \frac{B}{\lambda^2} + \frac{C}{\lambda^4}$$

$$k(\lambda) = D + \frac{E}{\lambda^2} + \frac{F}{\lambda^4} \qquad 2.3$$

where A-F are the parameters of dispersion relation and λ wavelength of light.

Assuming the trial thickness and the parameters of dispersion relation of the layers, theoretical reflection coefficients r_p and r_s for P and S components of the waves respectively were calculated using Fresnel formalism. Then Ψ and Δ spectra were generated using Eq. (2.4) given below:

$$\rho = \frac{r_p}{r_s} = \tan\psi \exp i\Delta \qquad 2.4$$

The theoretically generated spectra were fitted with experimentally measured ellipsometry data by varying thickness, parameters of dispersion relations for extracting the thickness and optical constants (n and k). To obtain the best fit the measured ellipsometric data were fitted by

minimizing the square difference between the measured and calculated values. The fitting details are described elsewhere [2.22].

Figs. 4a and 4b shows the optical constants *n* and *k* spectral curves respectively. It is clearly seen that the *n* values increased monotonically with increasing wavelength and thickness of the semi-transparent Pt layer, indicating metallic behaviour. And the *k* values increased monotonically up to ~ 1000 nm and then after, started to bend with increasing wavelength. Besides these values decreased as the thickness of the Pt layer decreased, showing semitransparent behavior. The n values of the top Al_xO_y (Fig. 2a) layers were lower than that of the semi-transparent Pt layers. These data revealed that the top Al_xO_y layer also act as antireflection layer.

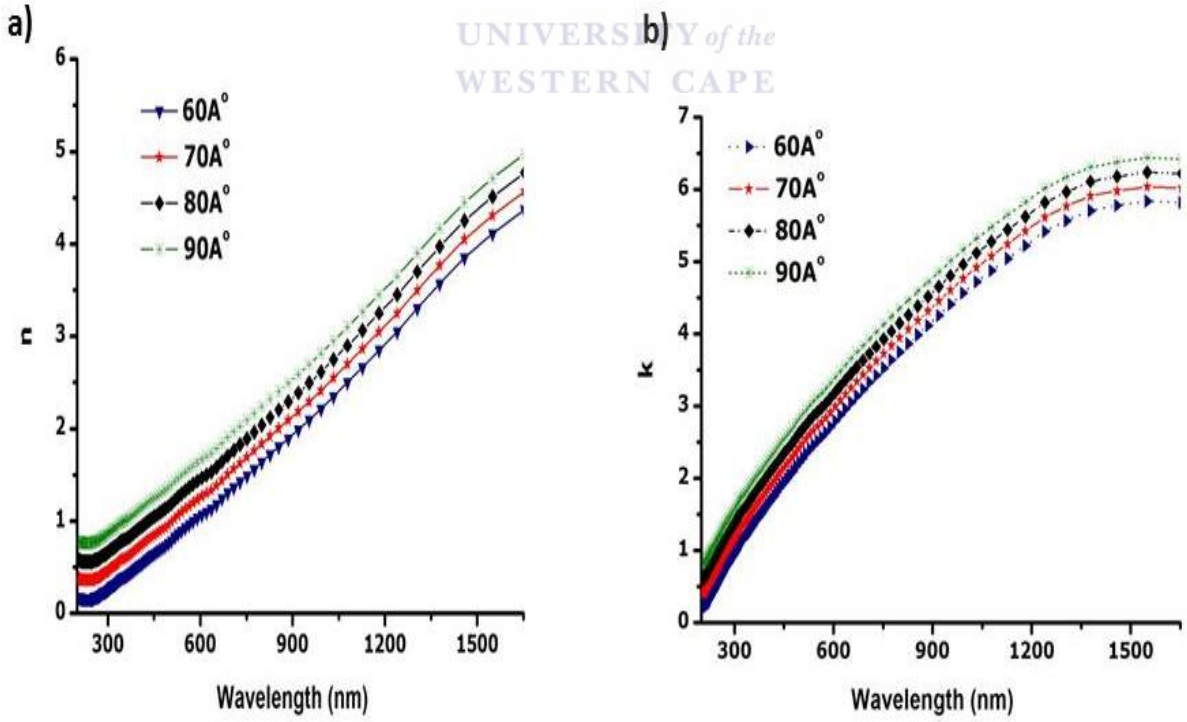

Figure 4: Estimated optical constants for Pt deposited on glass substrate having the evaluated thickness between 50 and 100 Å: a) refractive index b) extinction coefficient.

By utilizing n and k values, it was possible to simulate the spectral reflectance. Also in this case, we utilized the comparison between the simulated curve and the experimental spectrophotometric reflectance in order to validate the goodness of the procedure in determining the complex refractive index as shown from Fig. 5. It is seen that that there is a good agreement between the simulated and experimental reflectance spectra for the Pt layer 70 Å thick. The same good agreement was also obtained for all the other Pt layers.

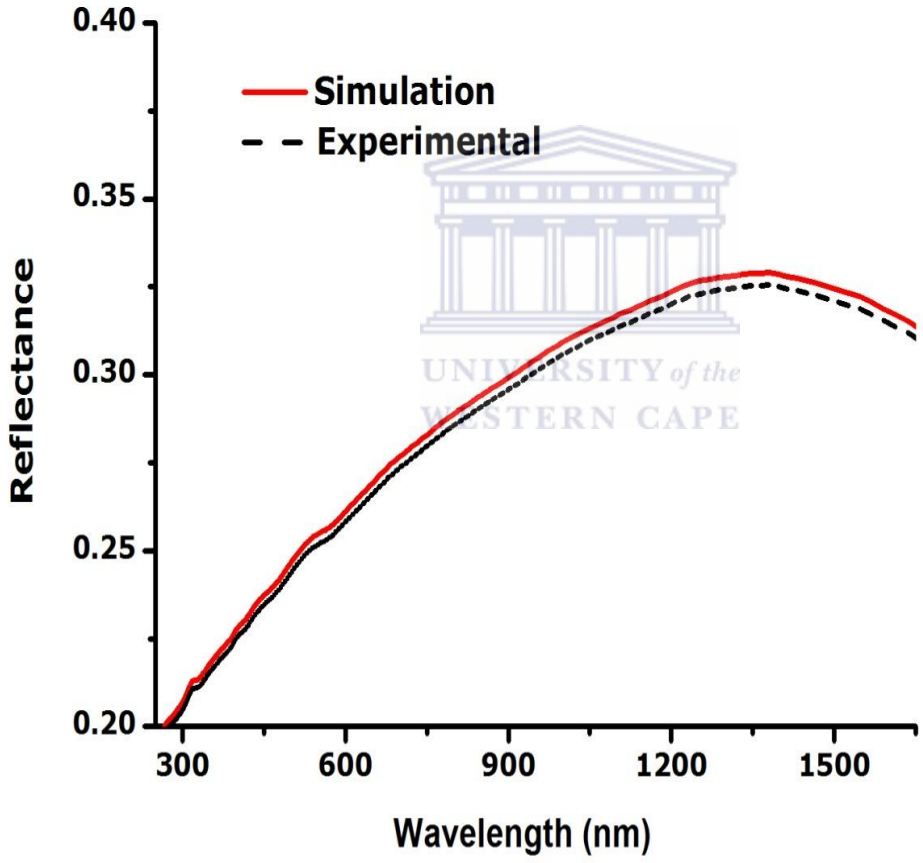

Figure 5: Comparison between the simulated solid red curve and the experimental black dashed curve spectral reflectance for Pt middle layer 70 Å thick deposited on glass.

2.3.3 Optical properties of Al_xO_y base layer

In order to characterize the base Al_xO_y layers of the multilayer absorber, a set of Al_xO_y 100-600 Å thick was deposited on glass substrate for the same purpose (see section 3.3.1) at the following process conditions: e-beam current applied to the target of 20 mA, pressure 10^{-6} mb and growth rate 1.8 ± 0.6 Å/s.

These layers were subjected to ellipsometric measurements in order to determine the spectral behavior of the complex refraction index $\tilde{N}$ and the same model as the top Al_xO_y layer was used. The generated optical constants, n and k, are shown in Fig. 6a. Similarly, it is seen that these layers have also dielectric behaviour. Fig. 6b shows the experimental spectral reflectance obtained from spectrophotometer technique. It is clearly observed that the reflectance curves decreased monotonically with increasing wavelength for Al_xO_y 100-400 Å thick. Whereas interference peaks appeared at the shortest visible region for 500 Å and 600 Å thick, this confirms the result of Al_xO_y top layers.

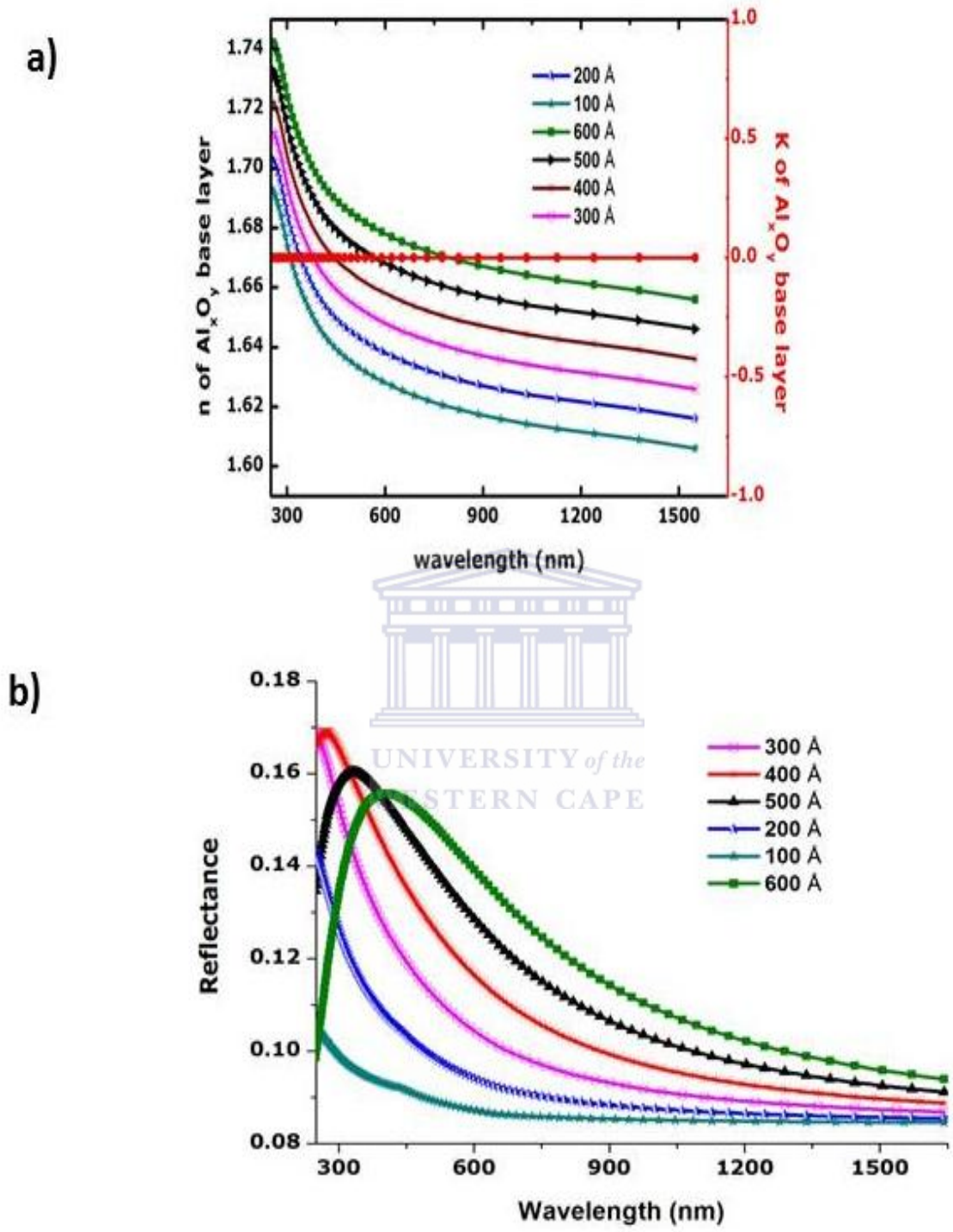

Figure 7: Al_xO_y base layer: a) estimated refractive index *n* and extinction coefficient *k* of different thickness, b) their corresponding reflectance spectra deposited on gas substrate.

At this point, by utilizing n and k values, it was possible to simulate the spectral reflectance of glass/Al_xO_y. Also in this case, we utilize the comparison between the simulated and the experimental reflectance in order to validate the goodness of the procedure in determining the complex refractive index. Fig. 7 showed a good agreement between the simulated and the experimental reflectance of the base Al_xO_y 400 Å thick layer. The same good agreement was also obtained for all the layers.

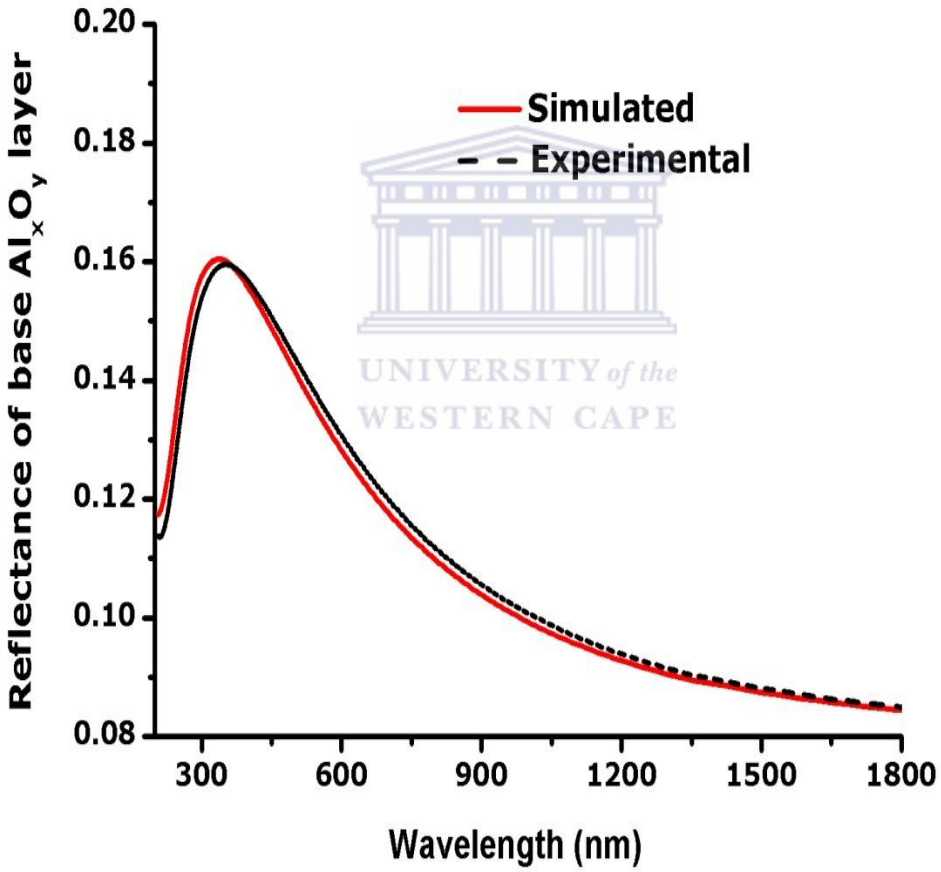

Figure 7: Comparison between the simulated red solid curve and the experimental black dashed curve spectral reflectance for Al_xO_y base layer 400 Å thick deposited on glass.

2.3.4 Optical properties of Al_xO_y /Pt/Al_xO_y selective absorber

At the end of the optical characterization, we had a suitable database in terms of spectral optical parameters related to the layers useful for the optimization and deposition of the spectrally selective stratification. As well known, an optimized spectrally selective coating must have a high absorption in the solar spectrum region and low thermal emittance in the wavelength of emission spectrum of the black body at an operating temperature. For this purpose, we utilize an optical spectrum simulation program suitable to generate the reflectance curve of thousands of thin film stratifications. Theoretically the optimized spectral should be a step function, zero reflectance in the solar spectrum region, unitary in the infrared region and step transition located at the longer wavelength in order to maximize solar absorptance (α) and to minimize thermal emittance (ε) at a fixed operating temperature. Therefore, the choice of optimized coating was carried out in two successive steps: first the coatings with highest absorptance in the spectral range 0.3-2.5 μm were selected. Afterwards, among these coatings, that one having the position and slop of transition able to minimize the thermal emittance was chosen.

Using the optical simulation programme, Al_xO_y and Pt was selected from the database available in the software and developed Al_xO_y/Pt/Al_xO_y layer stratification. The thicknesses of all the deposited layers were used as an input data for simulation. Numbers of simulation for the different thicknesses of the three layers were performed to obtain the best. More details of the software is described elsewhere [2.23]. Hence, the programme was able to select Al_xO_y 900 Å/Pt 70 Å/Al_xO_y 400 Å stratification with the desired photo-thermal parameters. Fig. 8 shows the simulated and the experimental reflectance of Al_xO_y 900 Å/Pt 70 Å/Al_xO_y 400 Å stacks. It is clearly seen that there is a good agreement between the simulated and experimental curves. The good agreement between these curves validates the procedure adopted to fabricate an

optimized coating at room temperature. Thus the multilayer coating exhibited low thermal emittance ε ~ 0.06 ± 0.01 at 82^{o}C maintaining an appreciable solar absorptance α ~ 0.94 ± 0.01.

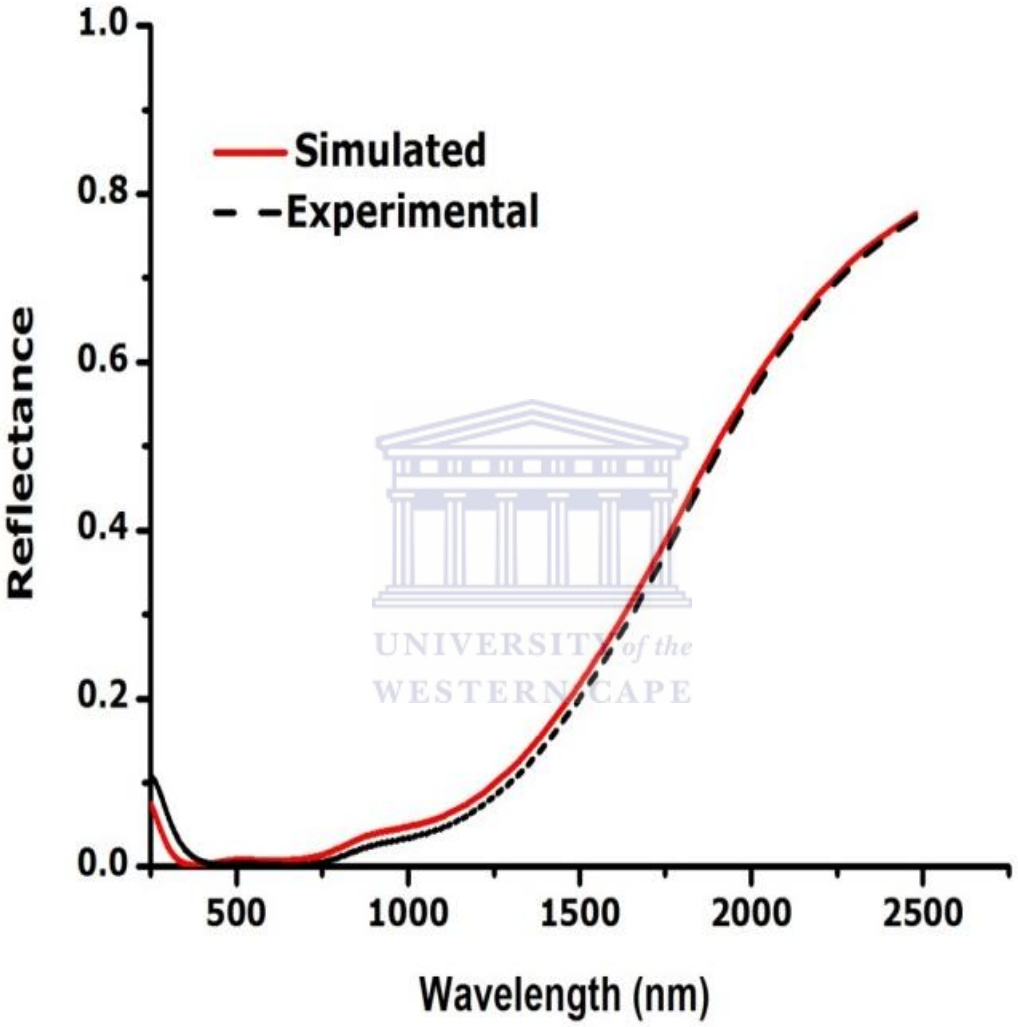

Figure 8: Comparison between the simulated solid red curve and the experimental black dashed cueve spectral reflectance for the optimized multilayer coating deposited on copper.

Generally, light absorption in thin films is due to two mechanisms: i) intrinsic absorption, which is characterized by extinction coefficient k ii) interference induced mechanism, which is characterized by refractive index n [2.26]. In the present case, for Pt metal layer both n and

k are high, whereas for both top and base Al_xO_y layers n is high while k is zero. This implies that the absorption in Pt layer is due to both intrinsic and interference induced mechanism. On the other hand, for both Al_xO_y absorption is due interference induced mechanism.

2.4 CONCLUSION

Coatings based on dielectric/metal/dielectric, fabricated starting from a careful optimization study, can well answer the requirements for spectrally selective coatings showing high performance. The employment of ellipsometric measurements and optical simulation was proposed as an effective method to optimize and deposit coatings, which shows the best performance at an operating temperature. In this contribution, we have described an approximately 1370 Å thick Al_xO_y/Pt/Al_xO_y solar selective coating which was fabricated using high vacuum e-beam evaporator. From the optical constants (n and k) obtained using ellipsometry of each layer, the top and base Al_xO_y layers used in the corresponding coatings were naturally dielectric and the middle Pt layer, was semi-transparent. The optimized multilayer absorber deposited on Cu substrate exhibited high solar absorptance of 0.94 ± 0.01 and low thermal emittance of 0.06 ± 0.01 at 82 ^oC. Light absorption was due to intrinsic and interference mechanism for Pt layer and due to interference mechanism for Al_xO_y layers.

2.5 REFERENCES

2.1 B. Seraphin, ‘‘solar energy conversion-solid state physics aspects, topics in applied physics’’, Berlin: Springer; (1979).

2.2 C. G. Niklasson, C. G. Granqvisit, J. Mater. Sci 18 (1983) 3475-3534.

2.3 A. Andersson, O. Hunderi , C. G. Granqvisit. J. Appl. Phys 51 (1980) 754-764.

2.4 A. Gibauda, C. Sellab, M. Maaza, L. Sungd, J. A. Durad, S. K. Satijad, Thin Solid Films 340 (1999) 153 -158.

2.5 Q. C. Zhang, D. R. Mills, J Appl Phys 72 (1992) 3013-3021.

2.6 Zebib Y. Nuru, C. J. Arendse, R. Nemutudi R, O. Nemraoui, M. Maaza, Physica B 407 (2012) 1634-1637.

2.7 G. A. Niklasson, C. G. Granqvist, J. Appl. Phys 55 (1984) 3382-3410.

2.8 J. A Thrnthon, L. Lamb James, Thin Solid Films 83 (1981) 377- 385.

2.9 C. Sella, Vien Tran Khanh, J. Lafait, S. Berthier, Thin Solid Films 90 (1982) 425-431.

2.10 M. Maaza, O. Nemraoui, C. Sella, J. Lafait, A. Gibaud , Baruch-Barak, Solid State Comm. 137 (2006) 166-170.

2.11 M. Maaza, O. Nemraoui, C. Sella, J. Lafait, A. Gibaud, V. Pischedda, Phys. Lett. A 344 (2005) 57-63.

2.12 A. Mascetta Joseph. ‘‘Chemistry the easy ways’’, 4th ed. New York, (2003).

2.13 C. E Kenndy, ‘‘Review of mid- to high-temperature solar selective absorber materials’’; (2002). NREL/TP - 520-31267.

2.14 Jhon A Thornton, Alans. S. Penfold, James L. Lamb, Thin Solid Films 72 (1980) 101-110.

2.15 Harish C. Barshilia, N. Selvakumar, K. S. Rajam. J. Appl. Phys 103 (2008) 023507(1) - 023507(11).

2.16 Harish C. Barshilia, N. Selvakumar, G. Vignesh, K. S Rajam, A. Biswas, Solar Energy Materials & Solar Cells 93 (2009) 315-323.

2.17 N. Selvakumar, Harish C. Barshilia, K. S. Rajam, A. Biswas, Solar Energy Materials & Solar Cells 94 (2010) 1412-1420.

2.18 H. Fujiwara, ‘‘Spectroscopy ellipsometry principles and applications’’, England: John Weley & Sons Ltd; (2007).

2.19 S. Ninomiya, S. Adachi. J. Appl. Phys 78 (1995) 1183-1- 1183-8.

2.20 S. Adachi, H. Mori, S. Ozaki, Phys. Rev B 66 (2002) 153201-1 - 153201-4.

2.21 N. K. Sahoo, S. Thakur, M. Senthilkumar, D. Bhattacharyya, N.C. Das. Thin Solid Films 440 (2003) 155-168.

2.22 A. Biswas , D. Bhattacharyya, H. C. Barshilia, N. Selvakumar , K. S. Rajam Appl Surf Sci 254 (2008) 1694- 1699.

2.23 W. Theiss, ‘‘SCOUT Optical Spectrum Simulation, W. Theiss Hard- and Software’’, Achen, (2002).

2.24 K. Gelin, ‘‘Preparation and characterization of sputter deposited spectrally selective solar absorbers’’, Ph.D. Dissertation. Sweden: Uppsala University; (2004).

2.25 D. Bhattacharyya, A. Biswas, J. Appl. Phys 97 (2005) 053501.

2.26 O. S. Heavens, ‘‘Optical properties of thin solid films’’, New York (1965).

2.27 J. A. Van Kan, J. H. Rector, B. Dam, R. D. Vis. Nucl. Instrum. Methods Phys. Res B 89 (1994) 204-207.

CHAPTER THREE

STRUCTURAL AND OPTICAL PROPERTIES OF $Al_xO_y/Pt/Al_xO_y$ MULTILAYER ABSORBER

ABSTARCT

We report on the microstructure and optical properties of $Al_xO_y/Pt/Al_xO_y$ interference-type multilayer films, deposited by electron beam (e-beam) deposition onto corning 1737 glass, silicon (111) and copper substrates. The structural properties were investigated by Rutherford backscattering spectrometry, X-ray diffraction, scanning electron microscopy, energy dispersive X-ray spectroscopy and atomic force microscopy. The optical properties were extracted from specular reflection/transmission, diffuse reflectance and emissometery measurements. The stratification of the coatings consists of a semitransparent middle Pt layer sandwiched between two layers of Al_xO_y. The top and bottom Al_xO_y layers were non-stoichiometric with no crystalline phases present. The Pt layer is in the fcc crystalline phase with a broad size distribution and spheroidal shape in and between the rims of Al_xO_y. The surface roughness of the stack was found to be comparable to the inter-particle distance. The optical calculations confirm a high solar absorptance of ~0.94 and a low thermal emittance of ~0.06 for the multilayer stack, which is attributed not only to the optimized nature of the multilayer interference stacks, but also to the specific surface morphology and texture of the

coatings. These optical characteristics validate the spectral selectivity of the $Al_xO_y/Pt/Al_xO_y$ interference-type multilayer stack for use in high temperature solar-thermal applications.

The content of this chapter was published in: Journal of Material Science and Engineering B 177 (2012) 1188-1193

3.1 INTRODUCTION

The limited supply of fossil hydrocarbon resources and the negative impact of CO_2 emission on the global environment dictate the increasing usage of renewable energy sources. Concentrating solar power (CSP) systems are the most likely candidate for providing the majority of the renewable energy. For efficient photo-thermal conversion, these systems require spectrally selective surfaces with high solar absorbance in the solar spectrum region and low thermal emittance in the infrared region [3.1]. To achieve this spectral selectivity, various concepts such as semiconductor–metal tandems, metal–dielectric composites and multilayer absorbers have been used by several authors [3.2–3.6].

A large number of studies have been made for Al_2O_3 based solar selective coatings, such as Ni–Al_2O_3 [3.7], Mo–Al_2O_3 [3.8, 3.9], Au–Al_2O_3 [3.10], Ag–Al_2O_3 [3.11], W–Al_2O_3 [3.12], Co–Al_2O_3 [3.13], Fe–Al_2O_3 [3.14] and Pt–Al_2O_3 [3.15–3.19]. These studies have mainly focused on Metal–dielectric composite coatings. Metal–dielectric composites have a highly absorbing coating in the solar spectrum region that is transparent in the IR region, deposited onto a highly IR reflector metal substrate [3.20]. However the multilayer concept for solar selective applications has not been studied widely.

Multilayer absorbers, also called multilayer interference stacks, basically consist of a thin semi-transparent metal layer between two dielectric layers and can be designed to be an efficient spectrally selective surface. Several multilayer absorbers using metals, such as Mo, Ag, Cu and Ni, and dielectric layers, such as Al_2O_3, SiO_2, CeO_2 and ZnS, have been studied for high temperature applications [3.20]. Al_2O_3–Mo–Al_2O_3 interference stacks, deposited by sputtering onto stainless steel substrates, showed high solar absorptance of 0.92–0.95 and thermal emittance of 0.06–0.10 at 20ºC [3.21]. Barshilia *et al*. [3.22] reported that Cr_xO_y/Cr/Cr_xO_y,

deposited on copper substrate by pulsed sputtering, achieved solar absorptance of 0.088–0.912 with low emittance of 0.05–0.06. They also reported multilayer of $Al_xO_y/Al/Al_xO_y$ interference stacks, deposited onto copper and molybdenum substrates using the same system that exhibited high solar absorptance of 0.950–0.970 and low thermal emittance of 0.05–0.08 at 82ºC [3.23]. $HfO_x/Mo/HfO_2$ deposited on copper and stainless steel using magnetron sputtering revealed high solar absorptance of 0.905–0.923 and low thermal emittance of 0.15–0.17 at 82ºC [3.24]. To the best of our knowledge, multilayer absorber stacks using Pt metal and Al_2O_3 dielectric, deposited by electron beam (e-beam) vacuum evaporation, have not been studied for high temperature solar-thermal applications. e-Beam vacuum evaporation is a promising method due to the possibility of depositing large area of thin films with a large extent contamination-free and no impurities.

It is well known that Pt is a good conductor of electricity, very unreactive and resists corrosion by water, air and other chemicals; even at high temperatures. Al_2O_3 has a high thermal conductivity, strength and stiffness, which is the most cost effective and widely used material in the family of ceramics that makes Al_2O_3 the choice for a wide range of optical applications. Owing to their unique properties, multilayer stacks using Pt and dielectric Al_2O_3 could be an attractive candidate for high temperature photo-thermal conversion applications.

The chapter reports on the microstructure and optical properties of $Al_xO_y/Pt/Al_xO_y$ multilayer stacks grown by e-beam vacuum evaporation onto corning 1737 glass, silicon (111) and copper substrates. The structure and the morphology of the stacks were studied using X-ray diffraction (XRD) and the scanning electron microscopy (SEM), respectively. The composition and thickness were determined by using Rutherford backscattering spectrometer (RBS), energy-dispersive X-ray spectroscopy (EDS) and profilometry. The surface mean roughness value of

the multilayer sample was measured using atomic force microscopy (AFM). The optical performance, absorptance and emittance were measured using spectrophotometer and emissometer, respectively.

3.2 EXPERIMENTAL DETAILS

$Al_xO_y/Pt/Al_xO_y$ multilayer stacks of 900 Å Al_xO_y top layer, 70 Å Pt middle layer and 400 Å Al_xO_y base layer were deposited at room temperature onto corning 1737 glass (dimension 3 cm × 3 cm), Si (111) (1 cm×2 cm) and copper (3 cm×3 cm) substrates using 3 kW high vacuum e-beam evaporation system at a deposition pressure of 10^{-6} mbar. The schematic diagram of the $Al_xO_y/Pt/Al_xO_y$ multilayer absorber is shown in Fig. 1. Highly pure, Al_2O_3 pellets (purity 99.999% and 3 mm in diameter) and a Pt disc (purity 99.9% and 35 mm in diameter) target, which was purchased from Sigma–Aldrich, were placed on the crucibles for the deposition of the above mentioned films. Prior to deposition, the substrates were polished and cleaned by ultrasonic washing and degreased with methanol, ethanol, and trichloroethylene each for 15 min and finally cleaned using deionized water. The e-beam current was varied between 10 and 20 mA for Al_2O_3 layers and was 160 mA for the Pt layer. The deposition rates were monitored with a crystal quartz monitor during evaporation, which amounted to1.8 ± 0.6Å/s and 1.2 ± 0.6 Å/s for the Al_2O_3 and Pt layers, respectively.

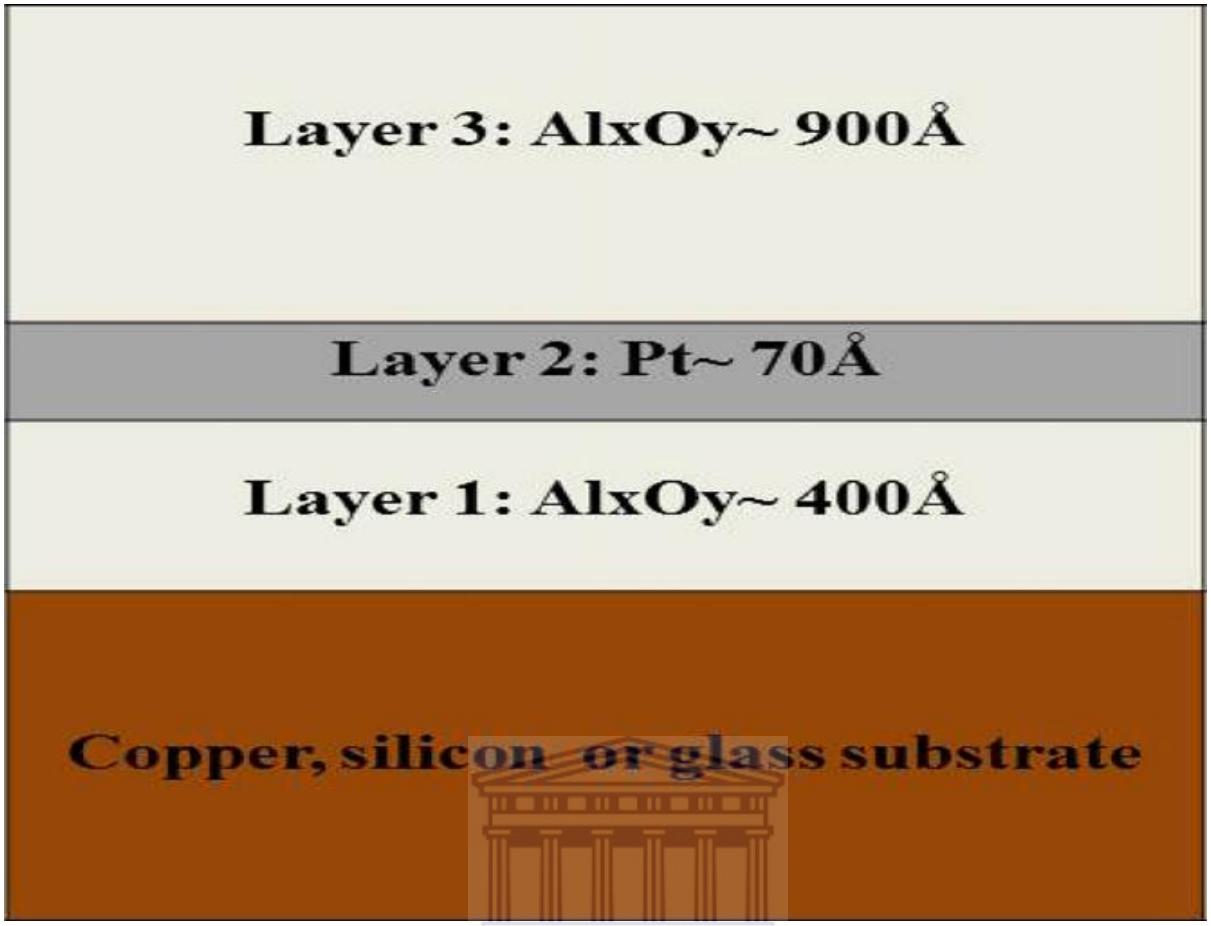

Figure 1: Schematic diagram of the $Al_xO_y/Pt/Al_xO_y$ absorber coating deposited on Cu, Si and corning glass substrates.

The above thicknesses were found the best to meet the criteria of solar absorbers. Thicker Pt layers resulted in higher reflectance in both visible and IR regions, whereas thinner Pt layers were more transparent. Similarly the thickness of the dielectric Al_xO_y layers determines the position of reflectance curve. The thicker the layer, the more shift towards the longest wavelength; and the thinner the layer, the more transparent in the visible region.

The substrates were chosen deliberately due to the following: Copper was chosen particularly for measuring the optical performance, i.e. solar absorptance and thermal emittance, since it

has low visible and high IR reflectance, which is critical to obtain higher solar absorptance. In addition it has a high thermal conductivity (401 W/mK) and low emittance value (0.03) that plays a great role to measure lower thermal emittance. Moreover it is ideal for practical applications. Corning glass was chosen for optical transmittance and thickness measurements. In order to avoid the roughness replication of the substrate on the morphology and average roughness of the coatings, single-side polished (111) orientated Si substrates were chosen.

The thickness and composition of the evaporated multilayers were determined by Rutherford backscattering spectrometer (RBS), using a 2 MeV He^{2+} ion beam with a scattering angle of 165º. The film thickness, extracted from RBS, was confirmed using a Veeco© Dektak Profilometer. The crystalline structure was studied by using a Model Bruker AXS D8 advance X-ray diffraction (XRD) system using the radiation of Cu-k_α with wavelength 1.5406 Å. The morphology of the films was acquired using Leo-Stero Scan 440 scanning electron microscope (SEM). Elemental analysis was performed using an energy dispersive X-ray spectroscopy (EDS) system, at an accelerating voltage of 15 kV. The topography and surface roughness were studied using a Veeco® Nanoman atomic force microscope (AFM) operated in tapping mode along x, y and z directions of image surface area 9.01 μm^2.

Diffuse reflectance was measured with a Cary 5000 UV–vis–NIR spectrophotometer of Varian, Inc. model internal DRA-2500 in the wavelength range of 0.3–2.5 μm. The solar absorptance was calculated from the measured diffuse reflectance data and weighted by solar irradiance using standard AM1.5 solar spectrum in the above wavelength range. Thermal emittance spectra were acquired by an emissometer model AE1 at room temperature (300 K), which has an accuracy of ±0.01 emittance units. The detector portion of this instrument was electrically heated to 82ºC. Both measurements were performed on the films deposited on the Cu substrate.

Specular reflection and transmission spectra were measured simultaneously on the same spot of the stack, using a TF Companion UV/VIS system in the range 200–1000 nm. These measurements were performed on the films deposited on the corning glass.

3.3 RESULTS AND DISCUSION

3.3.1 Compositional characterization

Fig. 2 shows the RBS spectra of the top and bottom layers of the $Al_xO_y/Pt/Al_xO_y$ stack deposited on a Si (111) substrate. The simulated spectra were obtained using RUMP and Genplot software. The thickness of the multilayer was estimated to be 900 Å for the Al_xO_y top layer, 70 Å for the middle Pt layer and 400 Å for the base Al_xO_y layer, leading to growth rates of approximately 1.8 Å/s, 1.2 Å/s and 1.8 Å/s, respectively.

With an accuracy of 2–5% [3.25] in RBS, the top and bottom layers were found to exhibit dissimilar elemental concentrations. Fig. 2(a) shows the simulation of the top Al_xO_y layer using an e-beam current ~20 mA and found to be: oxygen 58.00 ± 0.02 at.%, aluminium 40.56 ± 0.32 at.%, platinum 0.86 ± 0.04 at.% and silicon 1.4 ± 0.29 at.%. Similarly simulation of the base Al_xO_y layer using an e-beam current ~10 mA is also shown in Fig. 2(b). It was found: oxygen 51.00 ± 0.01 at.%, aluminium 47.00 ±0.28 at.%, platinum 0.86 ± 0.01 at.% and silicon 1.2 ± 0.43 at.%. These results were confirmed by EDS analysis with minimal deviation, as seen from Fig. 2(c) and 2(d), respectively. In a pure Al_2O_3, the atomic ratio of Al to O is 2:3. Comparing this with the result obtained in this study by RBS and EDS, it is obvious that the Al_xO_y layers are nearly stoichiometric.

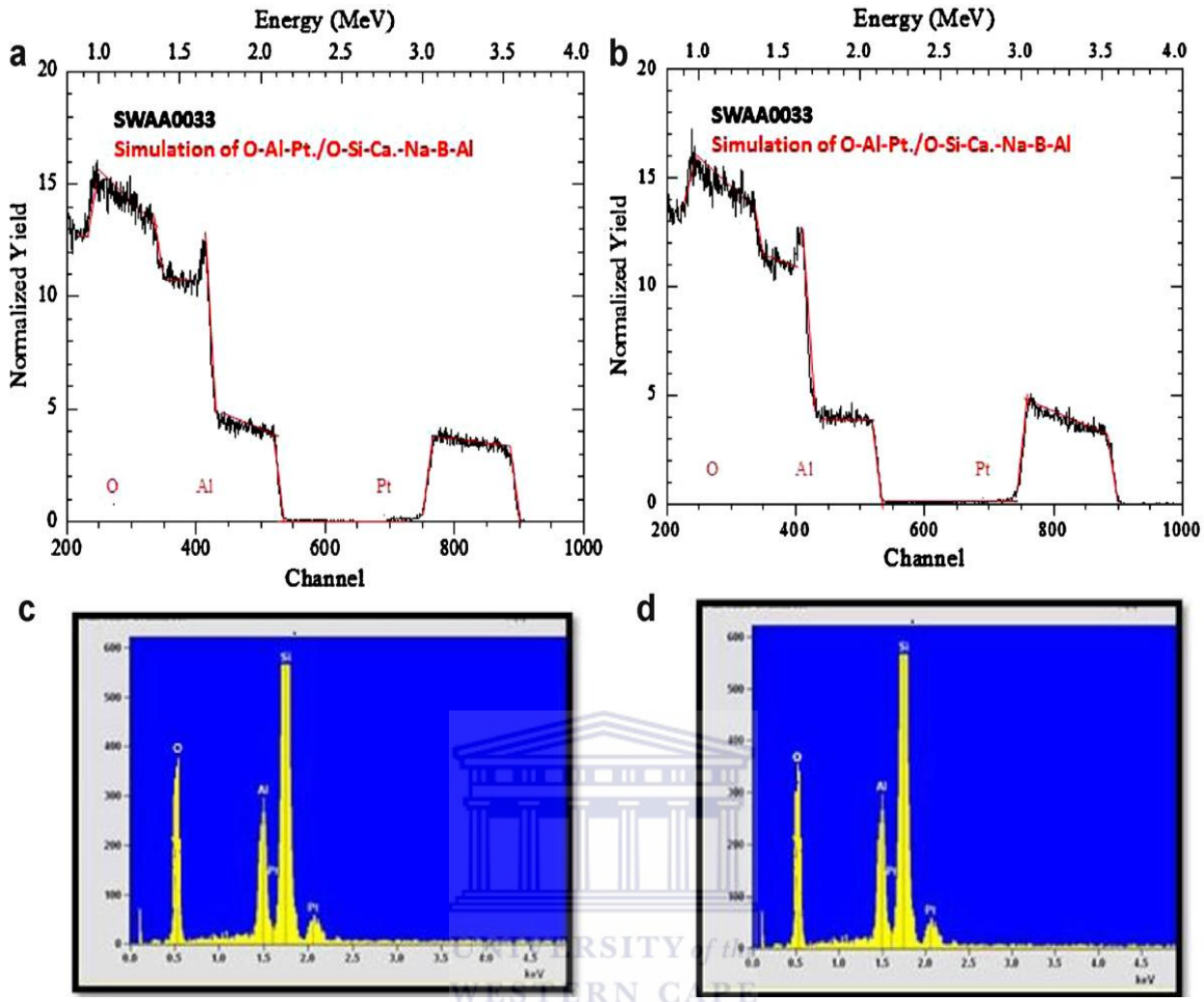

Figure 2: RBS spectra of (a) Al_xO_y top layer and (b) Al_xO_y base layer. EDS spectra of (c) Al_xO_y top layer and (d) Al_xO_y base layer.

3.3.2 Microstructural properties

The XRD patterns of the Al_xO_y/Pt/Al_xO_y film deposited on copper, silicon and corning glass substrates are shown in Fig. 3. As sustained by the data, copper and silicon substrates are highly crystalline fcc; with a net (200), (220) and (311) orientations for Cu and (111), (220), (311) and (400) orientations for Si. The top and base Al_xO_y layers are fully amorphous, as there is no corresponding Bragg peaks in the recorded 2θ angular range of 10–90º, which is

attributed to the fact that Al_2O_3 crystallizes at temperatures 900ºC. The Gaussian peak observed at ~40º is attributed to the (111) diffraction peak of fcc Pt. Further estimation of the crystallite size (D) and the d(111) spacing of Pt grains from the XRD data was done using Bragg's Law and Scherrer equation. The mean crystallite size and the d spacing obtained were about 250 Å and 2.265 Å, respectively.

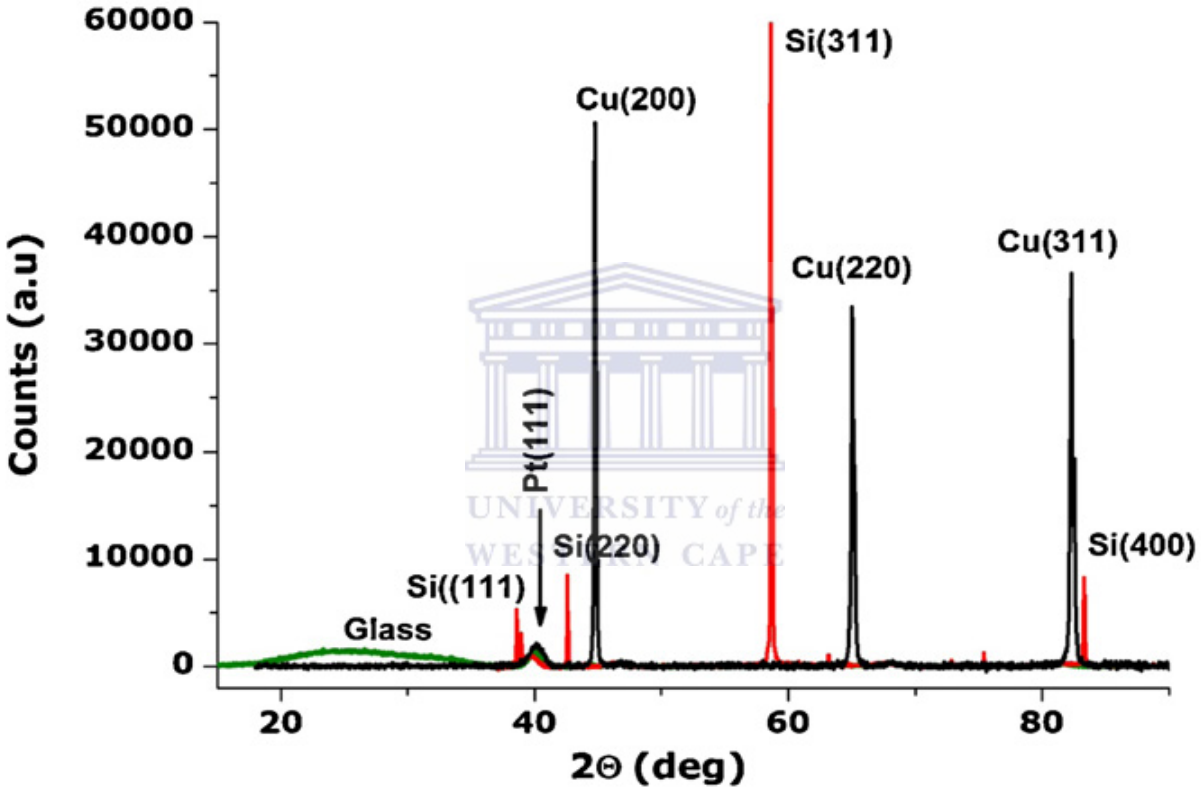

Figure 3: Typical XRD pattern of $Al_xO_y/Pt/Al_xO_y$ multilayer coatings deposited onto Cu, Si and corning glass substrates.

Two dimensional SEM micrographs of the $Al_xO_y/Pt/Al_xO_y$ multilayer films deposited on Si substrate are shown in Fig. 4(a)–(d). The corresponding multilayer film exhibits a flake-like surface morphology (Fig. 4(a)) with spherical Pt particles inlaid in and between the rims of Al_xO_y (Figs. 4(b) and 4(c)). To elucidate the characteristics of the microstructure of the

multilayer in detail, high resolution observation of the microstructure was performed, as shown in Fig. 4(d). The multilayer showed a microstructure consisting of some larger Pt grains with sizes 100–250 nm, and some small Pt grains with size less than 100 nm. The average diameter and interparticle distance are statistically calculated to be approximately 146 nm and 6–10 nm, respectively.

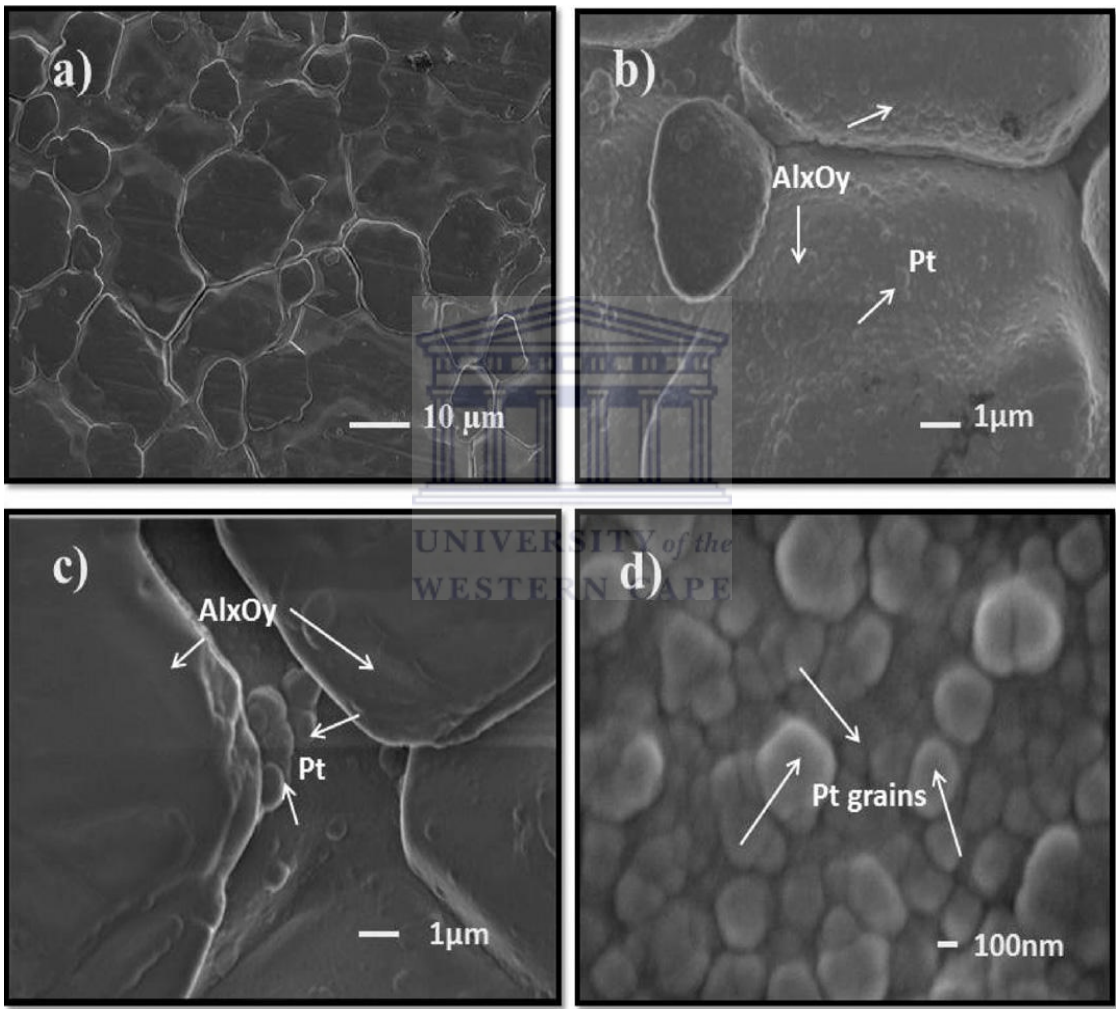

Figure 4: SEM images of the microstructure of $Al_xO_y/Pt/Al_xO_y$: deposited on Si substrate for different magnifications.

Fig. 5 shows a three-dimensional AFM topographic image of the $Al_xO_y/Pt/Al_xO_y$ multilayer coating deposited on a Si substrate. The surface exhibits a semi-ordered distribution, which has an average length of about 37 nm and consists of crystallites with an average diameter of 220 ± 0.24 nm. The average roughness value was found to be 6.5 ± 0.13 nm. The roughness value and the average crystallite diameter were comparable to the inter-particle distance and to the grain diameter obtained from SEM analysis.

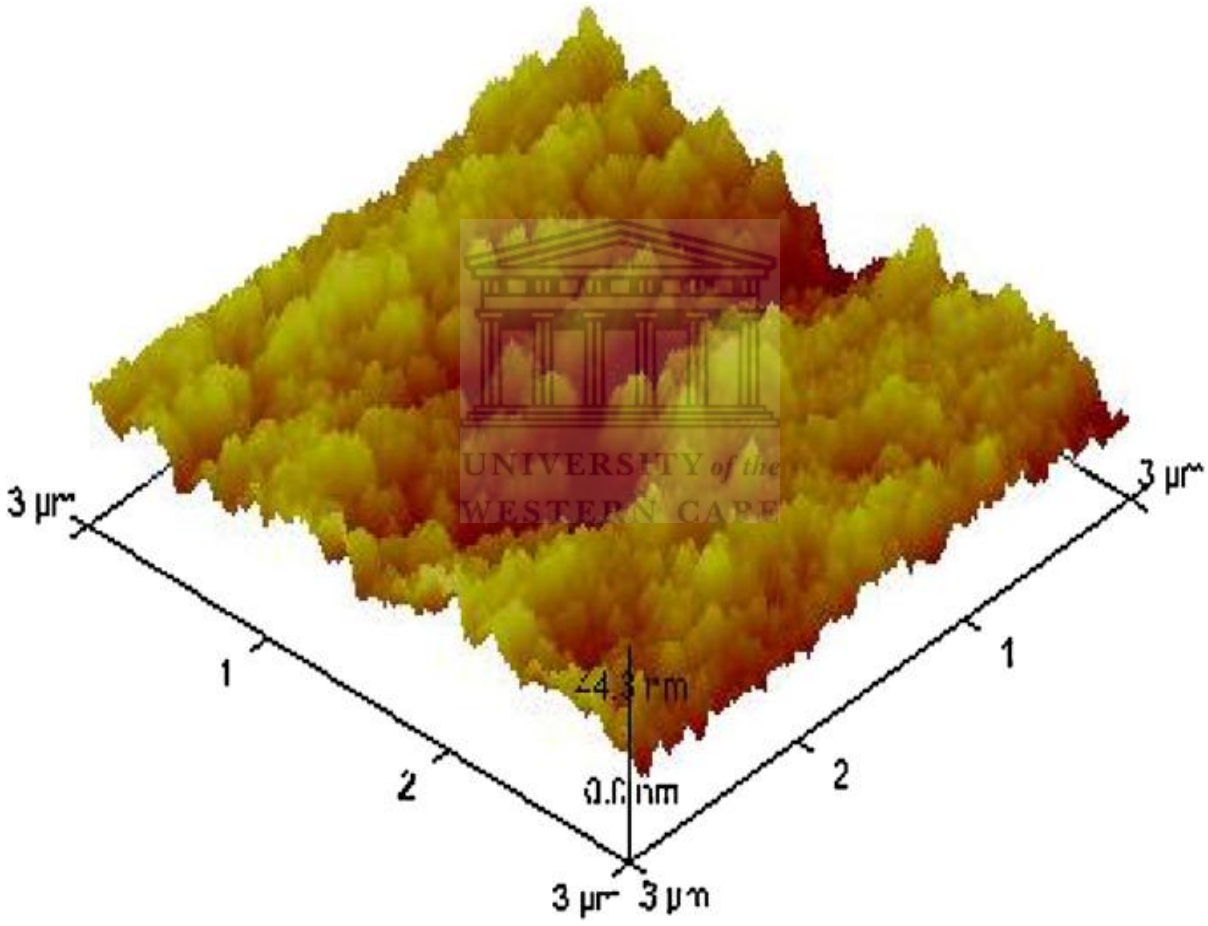

Figure 5: Three dimensional AFM topographic images of the $Al_xO_y/Pt/Al_xO_y$ multilayer coatings deposited on Si substrate.

3.3.3. Optical characterization

3.3.3.1 Spectrophotometer studies of the $Al_xO_y/Pt/Al_xO_y$ coating

The absorption spectrum for the absorber coating was calculated from the measured reflectance $R(\lambda)$ and transmittance $T(\lambda)$ spectra as:

$$A = 1 - (R + T)$$

Fig. 6 shows the resultant absorption spectrum $A(\lambda)$ for the multilayer coating. The absorption peaks centred at 236 nm and 404 nm in the visible solar radiation are attributed to the multiple reflections from the layers. The absorption decreases with an increase in the wavelength, which confirms the metallic behaviour of the semi-transparent Pt layer.

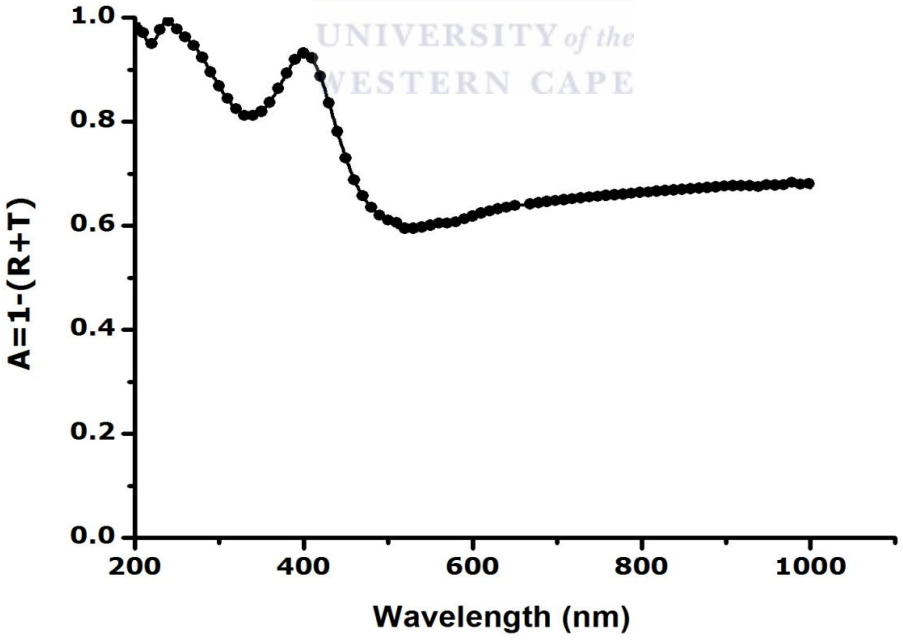

Figure 6: A typical absorption spectra $A(\lambda)$ for the $Al_xO_y/Pt/Al_xO_y$ multilayer absorber coating prepared at the optimized parameter.

3.3.3.2. Optical constants (n and k) of the $Al_xO_y/Pt/Al_xO_y$ coating

The reflectance and transmittance method was used for determining *n* and *k* for the evaporated $Al_xO_y/Pt/Al_xO_y$. The calculations have been performed by the optical spectrum simulation programme called SCOUT [3.26]. The dielectric constants of the thin films and the film thickness were fitted simultaneously to the measured reflectance and transmittance spectra. The software uses Fresnel formalism to calculate the reflectance of multilayer films. This programme uses a downhill simplex method to minimize the fit deviation.

As reported in Fig. 7, the simulation demonstrates a prominent feature of the optical constants calculated from the above mentioned software. It indicates that the refractive index is greater than the extinction coefficient, while both of them are positive. This indicates that, in the UV–VIS–NIR spectral region, light is not rejected but absorbed. This is different from the equivalent coatings of pure Pt and Al_2O_3 that light is reflected and transmitted, respectively. The absorptivity effect on the multilayer coatings is due to the decrease in the visible reflectance by Al_xO_y dielectric layers. This visible reflectance originates from the semi-transparent Pt layer used in the coatings, which has a measured reflectivity of about 60 % and 35–40 % in the IR and visible regions, respectively.

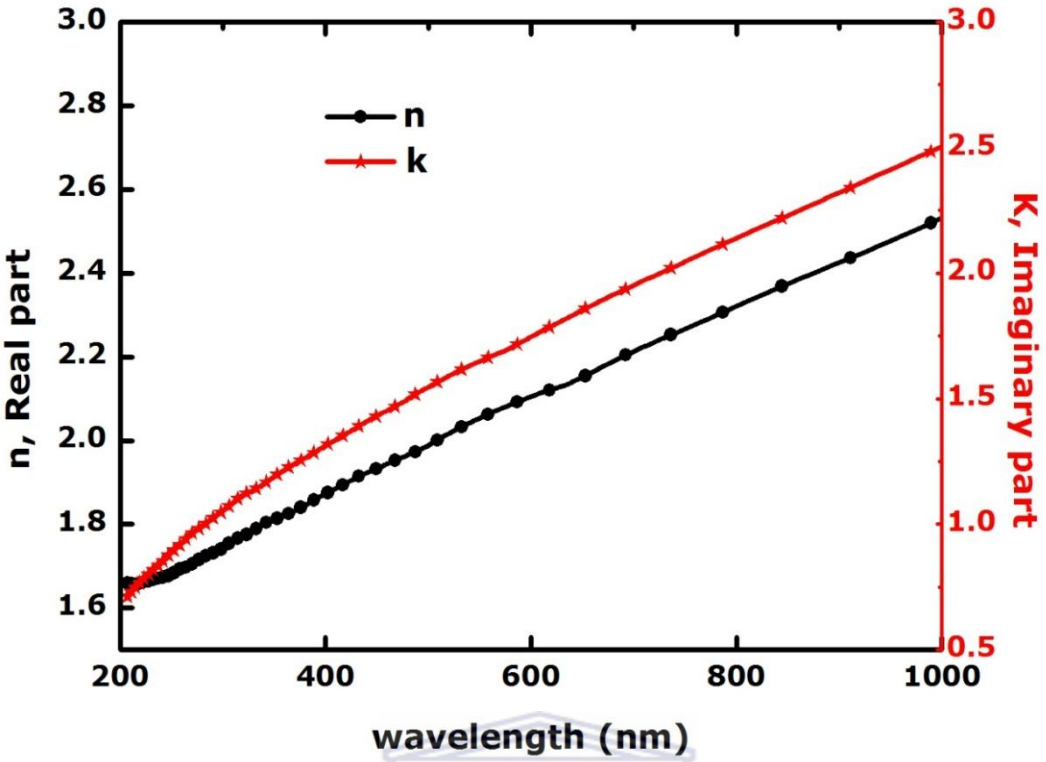

Figure 7: The real and imaginary parts of the refractive index for the optimized $Al_xO_y/Pt/Al_xO_y$ multilayer coatings.

3.3.3.3 Diffuse reflectance measurements of the $Al_xO_y/Pt/Al_xO_y$ coating

The experimental and simulated diffuse reflectance spectra of the multilayer coating are shown in Fig. 8. The light scattered by the films can be neglected, since the substrates were polished prior to deposition. It is observed that the coatings absorb maximum incoming solar radiation in the VIS–NIR region, ranging from 300 to 1100 nm and decreases as it goes to the longer wavelengths. Hence the multilayer coating corresponds to a solar absorptance of 0.94 ± 0.01 and a thermal emittance of 0.06 ± 0.01, having a spectral selectivity, $f = \alpha/\varepsilon \sim 15.33$. This selectivity is due to the multiple reflectance that pass through the layers. The solar performance; i.e. absorptivity and emissivity values, which demonstrate the feasibility of the

current considered multilayer stack, is attributed not only to the optimized nature of the multilayer interference stacks but also to the specific surface morphology and texture of these coatings as well.

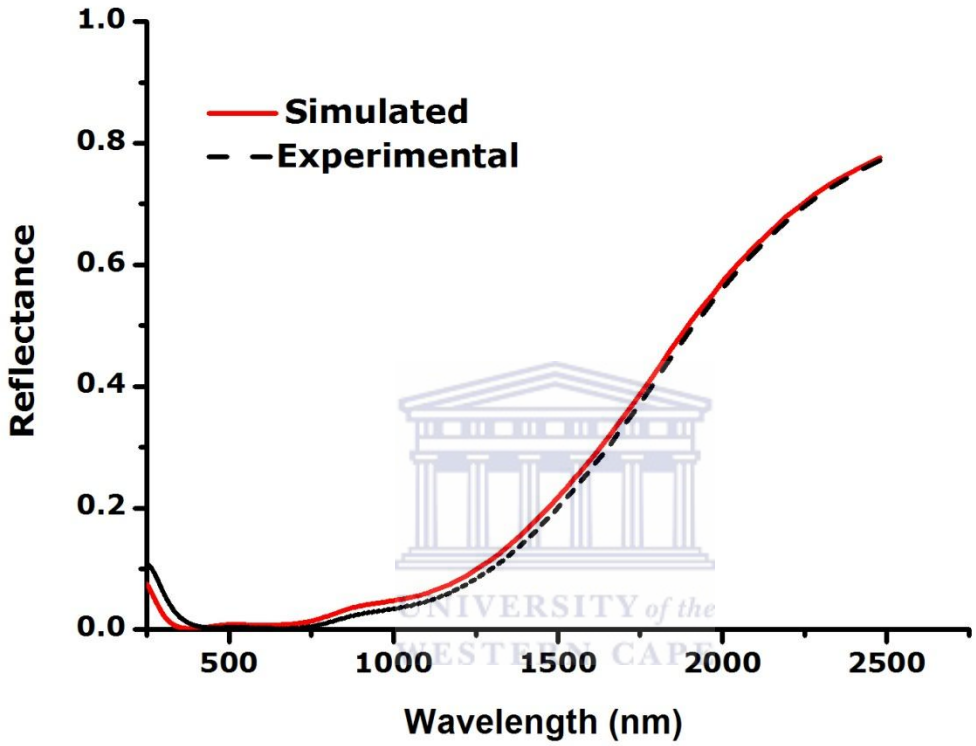

Figure 8: Spectral reflectance of the evaporated $Al_xO_y/Pt/Al_xO_y$ solar selective multilayer coating deposited on copper substrate.

3.4. CONCLUSION

We present in this chapter, an $Al_xO_y/Pt/Al_xO_y$ interference-type multilayer films deposited onto corning 1737glass, silicon (111) and copper substrates at room temperature using e-beam vacuum evaporator. The thickness was optimized to achieve high solar absorptance $\alpha \sim 0.94$

± 0.01 and low thermal emittance ε ~0.06 ± 0.01. RBS and EDS analysis confirmed that Al_xO_y layers used in the corresponding coating was non-stoichiometric. SEM and XRD analysis showed the Pt grains are in the fcc crystalline phase with a broad size distribution and spheroidal shape in and between the rims of Al_xO_y. The surface roughness of the stack was found to be comparable to the interparticle distance and it was negligible in comparison with the film thickness. Optical measurements confirmed that light absorption in the Al_xO_y/Pt/Al_xO_y multilayer coatings was due to the multiple reflectance from the layers.

3.5 REFERENCES

3.1 B. O. Seraphin, Topics in Applied Physics 31 (1979) 24–35.

3.2 T. Rictchie, B. Window, Applied Optics 16 (1977) 1438–1443.

3.3 Q. C. Zhang, D. R. Mills, Journal of Applied Physics 72 (1992) 3013–3021.

3.4 H. C. Barshilia, N. Selvakumar, K. S. Rajam, D.V.S. Rao, K. Murajeedharan, A. Biswas, Applied Physics Letters 89 (2006) 191909–191911.

3.5 J. A. Thornton, J. L. Lamb, Thin Solid Films 96 (1982) 175–183.

3.6 J. H. Schon, G. Binder, E. Bucher, Solar Energy Materials & Solar Cells 33 (1994) 403–416.

3.7 T. K. Bostrom, E. Wackelgard, G. Westin, Solar Energy Materials & Solar Cells 84 (2004) 183–191.

3.8 Q. C. Zhang, Y. Yin, D.R. Mills, Solar Energy Materials & Solar Cells 40 (1996) 43–53.

3.9 D. Xinkang, W. Cong, W. Tianmin, Z. Long, C. Buliang, R. Ning, Thin Solid Films 516 (2008) 3971–3977.

3.10 B. W. Woods, D.W. Thompson, J. A. Woollam, Thin Solid Films 469 (2004) 31–37.

3.11 H. C. Barshilia, P. Kumar, K. S. Rajam, A. Biswas, Solar Energy Materials & Solar Cells 95 (2011) 1707–1715.

3.12 A. Antonaia, A. Castaldo, M. L. Addonizio, S. Esposito, Solar Energy Materials & Solar Cells 94 (2010) 1604–1611.

3.13 G. A. Niklasson, C. G. Granqvist, Journal of Applied Physics 55 (1984) 3382.

3.14 C. Sella, A. Kaba, S. Berhier, J. Lafait, Solar Energy Materials and Solar Cells 16 (1987) 143–154.

3.15 J. A. Thornton, J. L. Lamb, Thin Solid Films 83 (1981) 377–385.

3.16 C. Sella, T. K. Vien, J. lafait, S. Berthier, Thin Solid Films 90 (1982) 425–431.

3.17 J. Lafait, S. Berthier, C. Sella, T. K. Vien, Vacuum 30 (1986) 125–127.

3.18 M. Maaza, O. Nemraoui, C. Sella, J. Lafait, A. Gibaud, V. Pischedda, Physics Letters A 344 (2005) 57–63.

3.19 M. Maaza, O. Nemraoui, C. Sella, J. Lafait, A. Gibaud, B. Baruch-Barak, A. C. Beye, Solid State Communications 137 (2006) 166–170.

3.20 C. E. Kennedy, ‘‘Review of mid- to high-temperature solar selective absorber Materials’’, NREL/TP-520-31267, (2002).

3.21 J. A. Thornton, A. S. Penfold, J. L. Lamb, Thin Solid Films 72 (1980) 101–110.

3.22 H. C. Barshilia, N. Selvakumar, K. S. Rajam, Journal of Applied Physics 103 (2008) 023507(1)–023507(11).

3.23 H. C. Barshilia, N. Selvakumar, G. Vignesh, K.S. Rajam, A. Biswas, Solar Energy Materials & Solar Cells 93 (2009) 315–323.

3.24 N. Selvakumar, H. C. Barshilia, K. S. Rajam, A. Biswas, Solar Energy Materials & Solar Cells 94 (2010) 1412–1420.

3.25 J. A. Van Kan, J. H. Rector, B. Dam, R. D. Vis, Nuclear Instruments & Methods in Physical Research B 89 (1994) 204–207.

3.26 W. Theiss, ‘‘SCOUT Optical Spectrum Simulation, W. Theiss Hard- and Software’’, Achen,(2002).

CHAPTER FOUR

THERMAL STABILITY OF ELECTRON BEAM EVAPORATED $Al_xO_y/Pt/Al_xO_y$ MULTILAYER SOLAR ABSORBER COATINGS

ABSTARCT

This chapter reports the effect of thermal annealing on $Al_xO_y/Pt/Al_xO_y$ multilayer solar absorber coatings deposited by electron beam (e-beam) vacuum evaporator onto copper substrate at room temperature. The samples were annealed at different temperatures for different duration in air. The samples were characterized by X-ray diffraction (XRD), scanning electron microscopy (SEM), energy dispersive x-ray spectroscopy (EDS), Atomic force microscopy (AFM), Raman spectroscopy, UV-vis spectrophotometer and emissometer. The results showed changes in morphology, structure, composition, and optical properties depend on both temperature and duration of annealing. The XRD pattern showed the intensity of Pt decreased with increasing annealing temperature and therefore, disappeared at high temperature. With increasing annealing temperature, an increase in the size of Pt particles was observed from SEM. The $Al_xO_y/Pt/Al_xO_y$ multilayer solar absorber coatings deposited onto Cu substrate were found to be thermally stable up to 500^oC in air for 2 h with good spectral

selectivity α/ε of 0.951/0.09. At 600°C and 700°C, the spectral selectivity decreased to 0.92/0.10 and 0.846/0.11 respectively, which is attributed to the diffusion of Cu and formation of CuO and Cu_2O phases. The formation of CuO and Cu_2O phases were confirmed by XRD, Raman spectroscopy and optical modeling. Long term thermal stability study showed the coatings were thermally stable in air up to 450°C for 24 h.

The content of this chapter was published in: Solar Energy Materials & Solar Cells120 (2014) 473-480.

4.1 INTRODUCTION

Currently the world relies on fossil fuels to produce 86% of its energy. However, the combustion of fossil fuels generates greenhouse gas, which is the major factor responsible for global warming [4.1]. To overcome the environmental problems and to fulfill the ever increasing demand of energy, mankind should use renewable energy sources. The sun, one of renewable sources, is the vast majority of energy used by people on earth. The sun's energy is environmental friendly and can be converted to heat and electricity. Hence to harness this inexhaustible energy, solar-thermal systems are the most important candidates. The critical part of these systems is the absorber surface, which attracts considerable attention for photo-thermal conversion [4.2-4.7]. To increase the photo-thermal conversion efficiency, the solar absorber surface should capture the maximum solar energy in the high intensity visible and near infrared spectral regions and should have minimum emittance for thermal IR radiation [4.8]. Moreover, it should be thermally stable at high temperatures (>400^{o}C) in air for concentrating solar power systems [4.9]. Therefore, to enhance its operating efficiency and withstand degradation performance, the thermal stability of the optical properties and microstructure of the absorber surface are critical.

Some selective solar absorber coatings for high temperature applications have been reported [4.10-4.12]. Okuyama *et.al* [4.10] developed graded Ni-MgO and Ni- SiO_2 cermets onto quartz using vacuum evaporation and was thermally stable in vacuum at 420^{o}C and 515^{o}C, respectively. Double cermet Mo-AlN deposited by sputtering on copper substrate was thermally stable in vacuum up to 500^{o}C [4.11]. Graded W-Al_2O_3 was deposited onto stainless steel using sputtering and found to be thermally stable up to 580^{o}C in vacuum [4.12]. These coatings are stable in vacuum for high temperature solar-thermal applications. However,

coatings need to be stable in air in case the vacuum is breached [4.13]. Meanwhile, there are some recently reported solar selective materials, which are thermally stable in air at high temperature [4.14-4.18]. Brashilia *et.al* [4.14] deposited a multilayer of $Al_xO_y/Al/Al_xO_y$ onto copper substrates, and found to be stable up to 400^oC. Selvakumar *et.al* [4.15] reported that multilayer of $HfO_x/Mo/HfO_2$ deposited onto copper substrates exhibited thermal stability up to 400^oC. $Al_2O_3/Mo/Al_2O_3$ deposited onto stainless steel substrates exhibited thermal stability up to 550^oC [4.16]. TiAl/TiAlN/TiAlON/TiAlO was developed onto copper substrates and exhibited thermal stability at 650^oC [4.17]. Lei *et.al* developed double cermet Ti_xAl_{1-x}/TiN/ (TiN-AlN)/AlN onto stainless steel and found to be thermally stable up to 400^oC [4.18].

The main reasons resulting in degradation of the selective solar absorber coatings at high temperature are oxidation and interfacial diffusion of the layers and the substrate [4.19]. Aluminium oxide (Al_2O_3) coatings have high hardness, excellent dielectric properties, refractoriness and good thermal properties and Pt has the capacity to resist oxidation even at high temperature [4.20]. Due to these properties, the composite of Pt and Al_2O_3 coatings was found the most promising solar absorber materials for high temperature concentrating solar-thermal applications. It has been found to be stable up to 600^oC in air [4.21-4.25]. Hence, due to this reason, alternative layer of vacuum evaporated Al_2O_3 and Pt has better thermal stability in air at high temperature than the reported multilayer solar absorber coatings even though most of the reported materials, which have good thermal stability, are either graded or double cermet coatings. Vacuum evaporated Co-Al_2O_3, Au- Al_2O_3, Ag-Al_2O_3, and Cr-Al_2O_3 have also been developed for evacuated tube collectors [4.26].

A number of materials such as TiAlN/TiAlON/Si_3N_4 [4.27], TiAlN/AlON [4.28], NbAlN/CrAlON/Si_3N_4 [4.29], HfMoN/HfON/Al_2O_3 [4.30], and TiAlN/TiAlON/SiO_2 [4.31]

have been developed recently for high temperature solar-thermal applications using sputtering and put forward to meet the basic characteristics of solar absorber materials. These studies still need to focus on the thermal stability of the microstructure, component distribution, interlayer diffusion and their mechanism under high temperature [4.32].

We developed a new spectrally selective $Al_xO_y/Pt/Al_xO_y$ multilayer solar absorber using e-beam evaporation. The structural and optical properties of the multilayers have been reported elsewhere [20, 33]. In this chapter, we present the effect of annealing on the microstructural, morphology, composition, optical properties and thermal stability of $Al_xO_y/Pt/Al_xO_y$ multilayer absorber deposited by e-beam evaporation, which was heated in air at different temperatures and durations.

4.2 EXPERIMENTAL DETAILS

$Al_xO_y/Pt/Al_xO_y$ multilayer stacks of 900Å Al_xO_y top layer, 70Å Pt middle layer and 400Å Al_xO_y base layer were deposited onto copper ($3 \times 3cm^2$) substrates using 3 kW high vacuum e-beam evaporation system at room temperature. The experimental details have been described in detail elsewhere [4.20, 4.33].

To study the thermal stability of the multilayer coatings, they were heated in air in an ultra-Furnace of Wirsam scientific type UF12/40/200 in the range of 300-700^oC at an increment of 100^oC for 2 h. The temperature was increasing from room temperature to the desired temperature at a rate of 5^oC/min and was cooled down at a rate of 2^oC/min. The accuracy of the set temperature was $\pm 7^oC$. Similarly, we also tested long term thermal stability of the

multilayer absorbers in air at 350^{o}C, 450^{o}C and 550^{o}C for 24 h. Thereafter the required analytical techniques were used to characterize the coatings.

The microstructure of the as- grown and annealed coatings were recorded by using X-ray diffraction (XRD) Model Bruker AXS D8 advance of radiation Cu (K_{α} = 1.5406Å) and a DILOR-JOBIN-YVON-SPEX integrated Raman spectoscopy . The morphology of the films was acquired using Leo-Stero Scan 440 Scanning electron microscope (SEM). The chemical composition was studied using energy-dispersive X-ray spectroscopy (EDS) using an accelerating voltage of 15 kV. Heavy Ion Elastic Recoil Detection analysis (HI-ERDA) was used as compliment to the EDS results. The surface roughness was studied using Veeco nanoman Atomic force microscopy (AFM) V operated in tapping mode.

Spectral reflectance was measured with a Cary 5000 UV–vis–NIR spectrophotometer of Varian, Inc. model internal DRA-2500 in the wavelength range of 0.3–2.5 μm. The solar absorptance was calculated from the measured reflectance data and weighted by solar irradiance using standard AM1.5 solar spectrum in the above wavelength range. Thermal emittance spectra were acquired by an emissometer model AE1, which has an accuracy of ± 0.01 emittance units. The solar absorptance and thermal emittance values of bare copper substrate was 0.203 and 0.03 respectively. In order to understand the degradation mechanism, an optical spectrum simulation program called SCOUT [4.34] was also used.

4.3 RESULTS AND DISCUSION

4.3.1 Structural properties

Fig.1 shows the XRD patterns of the as-deposited and annealed $Al_xO_y/Pt/Al_xO_y$ multilayer solar absorber coating deposited onto copper substrate. The prominent diffraction peaks of the as-deposited films at $2\theta = 40.01^o$, 43.3^o, 50.44^o and 74.08^o correspond to (111) plane of fcc Pt (JSPDS no. 00-001-1190) and (111), (200) and (220) plane of highly crystalline fcc Cu (JSPDS no. 00-004-0836) substrate, respectively. It is observed that annealing in air from 300-600^{o}C for 2 h shows a decrease in the intensity of the Pt (111) peak, which is due to the decrease in thickness of Pt layers, as probed by the HI-ERDA and optical modelling. Further increase of annealing temperature to 700°C in air leads to a complete disappearance of Pt diffraction peak, and to the formation of weak diffraction intensities of CuO and Cu_2O phases. The Pt peak position shifts from 40.01^o to higher angles and reaches 40.63^o after annealing at 600^{o}C in air. This is mainly due to the fact that heating decreases the stress, which was induced during the deposition process. No diffraction peaks corresponding to Al_xO_y were observed, which shows Al_xO_y is X-ray amorphous.

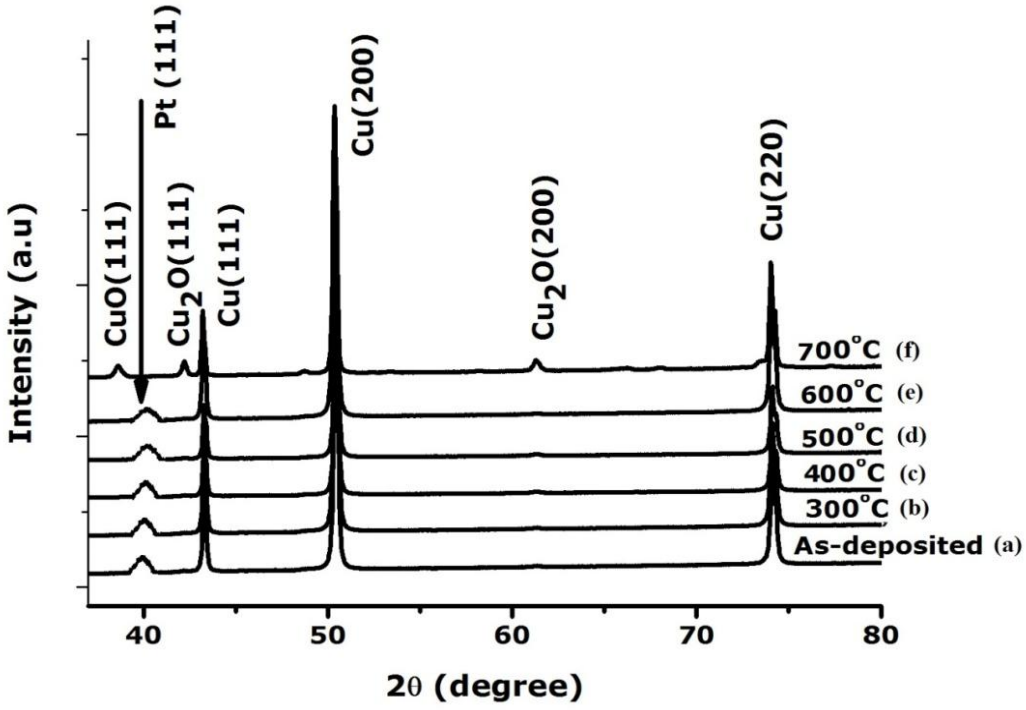

Figure 1: XRD pattern of $Al_xO_y/Pt/Al_xO_y$ multilayer solar absorber coatings as-grown (a) and annealed at different temperatures in air for 2 h: 300°C (b), 400°C (c), 500°C (d), 600°C (e), and 700°C (f).

The Raman spectrum of the as-deposited and annealed up to 700°C, which will be discussed later (see figs. 6 and 10), showed two broad bands centered at approximately 190 and 833cm $^{-1}$. These bands don't correspond to any Al_2O_3 phases rather corresponds to the vibration of aluminium and oxygen atoms, respectively [4.35]. Al_2O_3 exists in several crystalline phases such as $\gamma - Al_2O_3$ with *Fd 3 m* space group and $\alpha - Al_2O_3$ with R *3 c* space group. The former doesn't exhibit any active Raman modes [4.36] but the latter one exhibits seven Raman active phonon modes: $2A_{1g}$ (418 cm $^{-1}$, 648 cm $^{-1}$) and $5E_g$ (332, 431, 450, 526 and 745 cm^{-1}) [4.37]. Hence, the Raman data confirms the XRD result.

4.3.2 Surface morphology

Fig. 2(a)-(f) represent the surface morphology of the $Al_xO_y/Pt/Al_xO_y$ multilayer solar absorber deposited onto Cu substrates in the as-deposited and annealed at 300^{o}C, 400^{o}C, 500^{o}C, 600^{o}C and 700^{o}C in air for 2 h respectively. The as-deposited multilayer solar absorber surface depicts dense spherical Pt particles consisting of some larger Pt particles with sizes 100 – 250 nm, and some small Pt particles with size less than 100 nm. After annealing at 300^{o}C, 400^{o}C and 500^{o}C as shown in Fig. 2 (b), (c) and (d) respectively, an increase in the size of Pt particles has been observed. At 600^{o}C the Pt particles become irregular and agglomerate into larger particles (see Fig. 2(e)). Further increase of annealing temperature to 700^{o}C (Fig. 2(f)) leads to the formation of only CuO on the surface. It should be noted that the formation of larger Pt particles plays a significant role in atomic diffusion by acting as a path for Cu atomic movement towards the surface, which has been oxidized. No cracks were observed on the surface of the $Al_xO_y/Pt/Al_xO_y$ multilayer solar absorber, even after annealed at 700^{o}C.

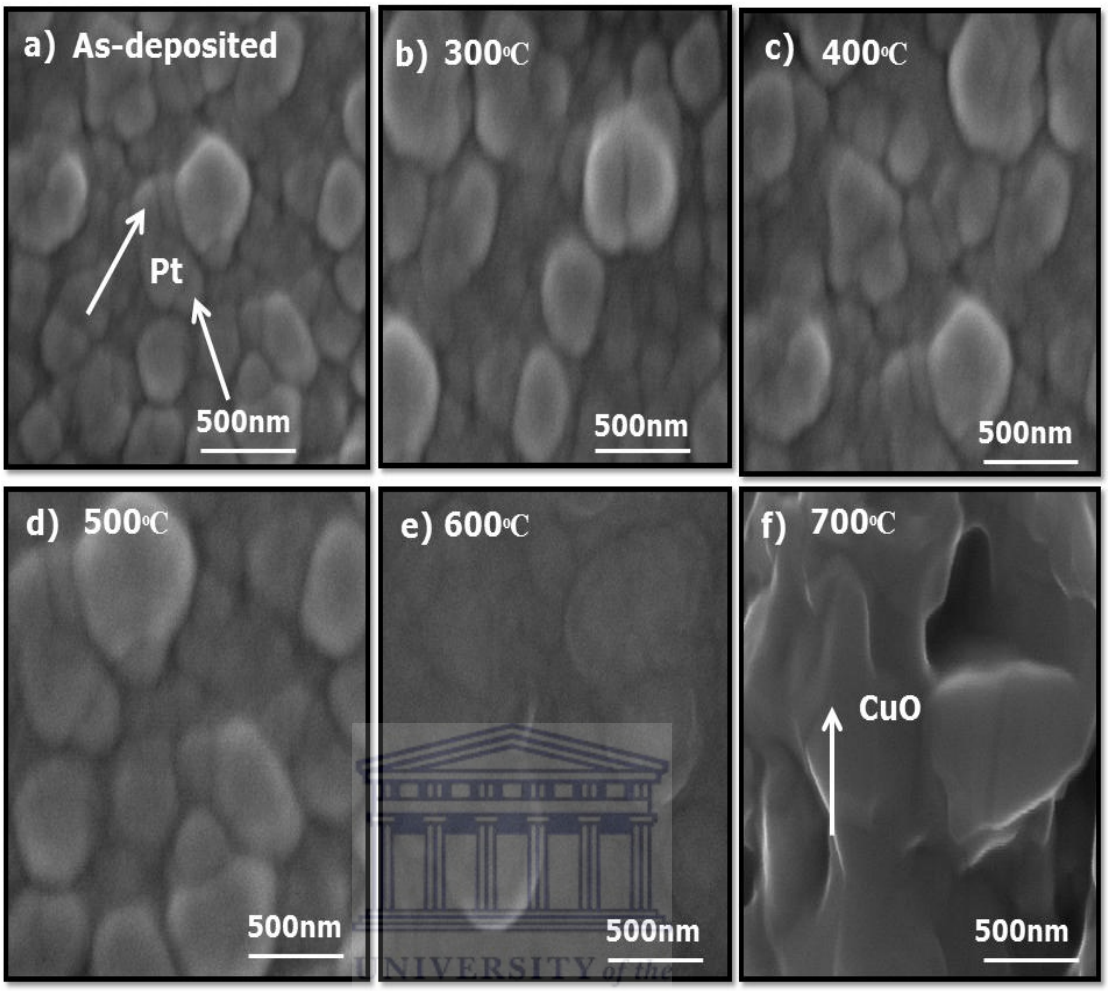

Figure 2: SEM images of $Al_xO_y/Pt/Al_xO_y$ multilayer solar absorber coatings as-grown (a), and annealed at different temperatures in air for 2 h: 300^{o}C (b), 400^{o}C (c), 500^{o}C (d), 600^{o}C (e), and 700^{o}C (f).

Fig. 3(a)-(f) depicts the AFM images of $Al_xO_y/Pt/Al_xO_y$ multilayer solar absorber deposited onto Cu substrates in the as-deposited state and annealed at 300^{o}C, 400^{o}C, 500^{o}C, 600^{o}C and 700^{o}C in air for 2 h respectively. The images show columnar growth, as would be expected from evaporated coatings grown from vapour phase deposition at low substrate temperature [4.38]. The particle sizes and lengths in the annealed samples are larger than those of the as-deposited. With increasing annealing temperature, the average diameter as well as the average

surface roughness increased, as summarised in Table 1. The average roughness of the $Al_xO_y/Pt/Al_xOy$ multilayer solar absorber is relatively constant up to 500°C, after which a noticeable increase is observed at 600^{o}C and 700^{o}C, which is attributed to the noticeable increase in the particles size.

Annealing temperature(^{o}C) in air	Average diameter (nm)	Average surface roughness (nm)
As-deposited	220	6.57±0.12
300	221.3	6.61±0.01
400	224	6.67±0.13
500	227	6.69±0.01
600	287.8	18.6±0.04
700	358	35±0.12

Table 1: Average Pt particle size and surface roughness of $Al_xO_y/Pt/Al_xO_y$ multilayer solar absorber as-deposited and annealed at different temperatures in air.

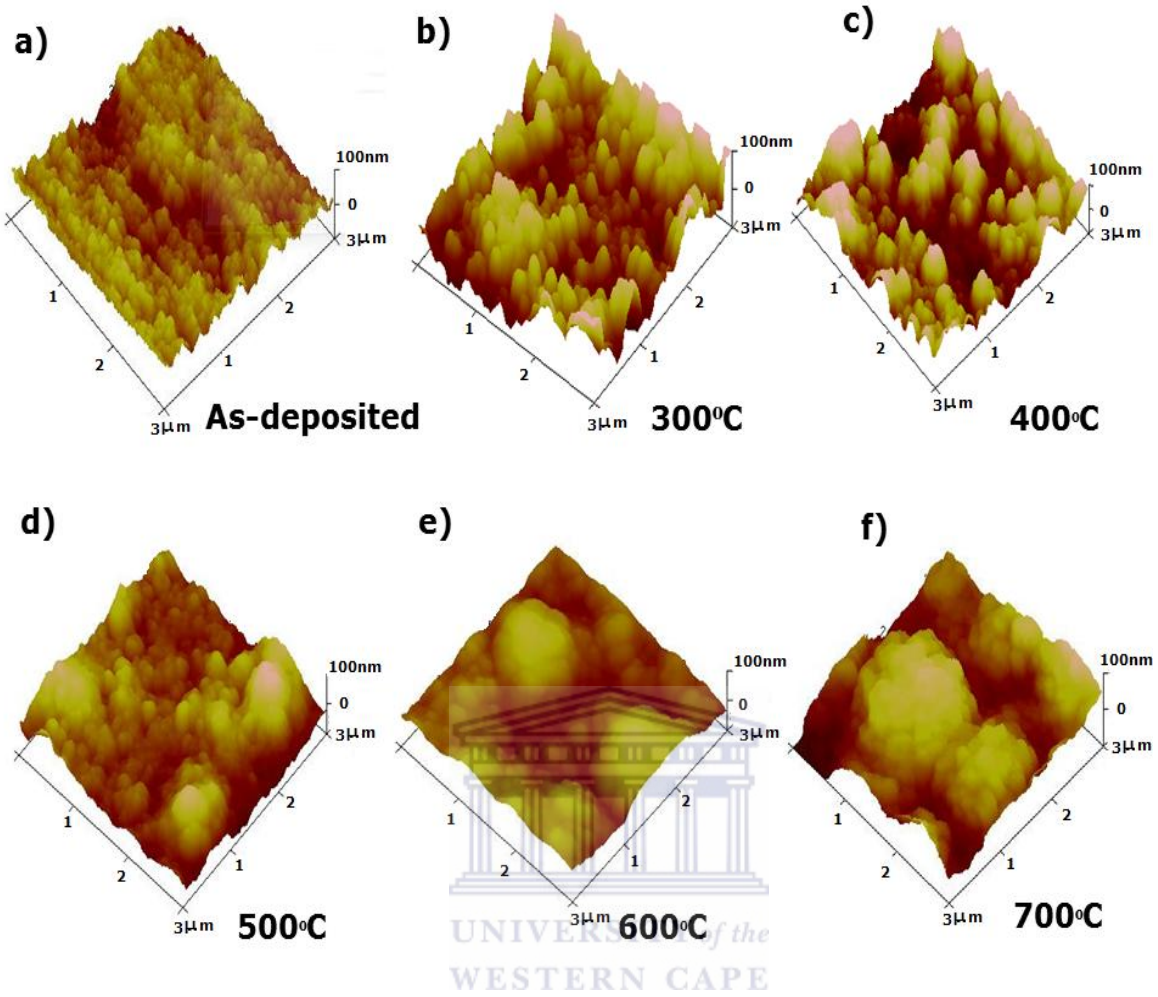

Figure 3: AFM images of $Al_xO_y/Pt/Al_xO_y$ multilayer solar absorber coatings as-grown (a), and annealed at different temperatures in air for 2 h: 300°C (b), 400°C (c), 500°C (d), 600°C (e), and 700°C (f).

4.3.3 Compositional properties

Fig.4(a)-(f) shows the EDS analysis of $Al_xO_y/Pt/Al_xO_y$ multilayer solar absorber deposited onto Cu substrates in the as-deposited state and annealed at 300°C, 400°C, 500°C, 600°C and 700°C in air for 2 h respectively. EDS spectra showed only sharp peaks from platinum, aluminium,

oxygen and from the copper substrate, confirming the pure nature of the prepared $Al_xO_y/Pt/Al_xO_y$ multilayer solar absorber coatings. It is observed that annealing of the films leads to a change in composition. The intensity of the platinum and aluminium peaks decreased slightly up to 500°C and diminishes gradually at 600°C, and finally disappears at 700°C. On the other hand, the signal of copper and oxygen increased as annealing temperature increased.

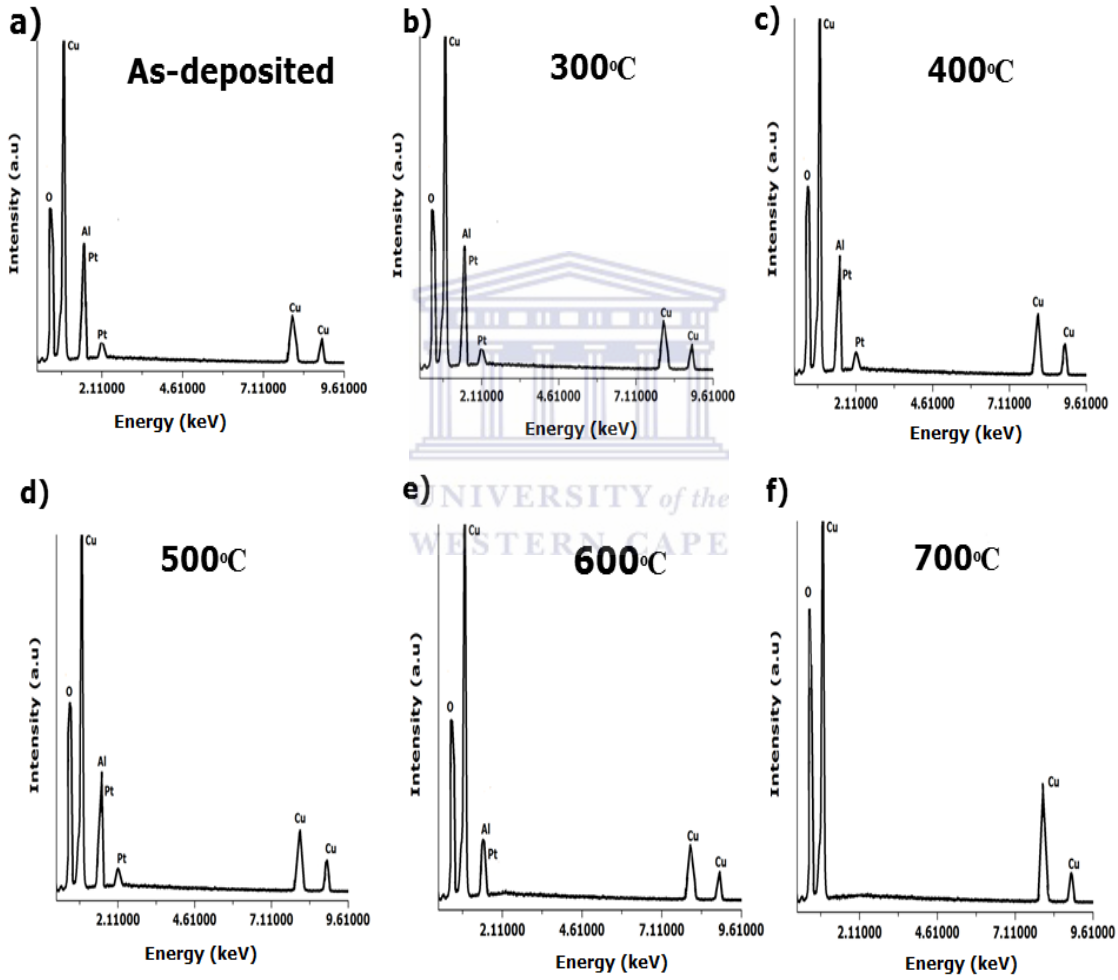

Figure 4: EDS spectra of $Al_xO_y/Pt/Al_xO_y$ multilayer solar absorber coatings as-grown (a), and annealed at different temperatures in air for 2 h: 300°C (b), 400°C (c), 500°C (d), 600°C (e), and 700°C (f).

4.3.4 Thermal stability in air

It is known that thermal stability is critical for solar absorber materials as it affects the two basic characteristics; i.e. solar absorptance and thermal emittance of the solar absorber material. Fig. 5 shows the reflectance spectra of $Al_xO_y/Pt/Al_xO_y$ multilayer solar absorber in the as-deposited state and annealed at 300°C, 400°C, 500°C, 600°C and 700°C in air each for 2 h. The corresponding absorptance and emittance values of the multilayer coating are given in Table 2. To achieve high solar selectivity, the coatings should exhibit low reflectivity in the visible near infrared (vis-NIR) region but high in the infrared region.

Temperature (°C)	Absorptance α			Emittance (ε =82°C)		
	As-deposited	Annealed	$\Delta\alpha$	As-deposited	Annealed	$\Delta\varepsilon$
Room temperature	0.952	-	-	0.08	-	-
300	0.952	0.952	-	0.08	0.09	+0.01
400	0.952	0.951	-0.001	0.08	0.09	+0.01
500	0.952	0.951	-0.001	0.08	0.09	+0.01
600	0.952	0.920	-0.032	0.08	0.10	+0.02
700	0.950	0.846	-0.104	0.08	0.11	+0.03

Table 2: Effect of annealing in air for 2 h on solar absorptance and thermal emittance values of the $Al_xO_y/Pt/Al_xO_y$ multilayer solar absorber deposited onto Cu substrate.

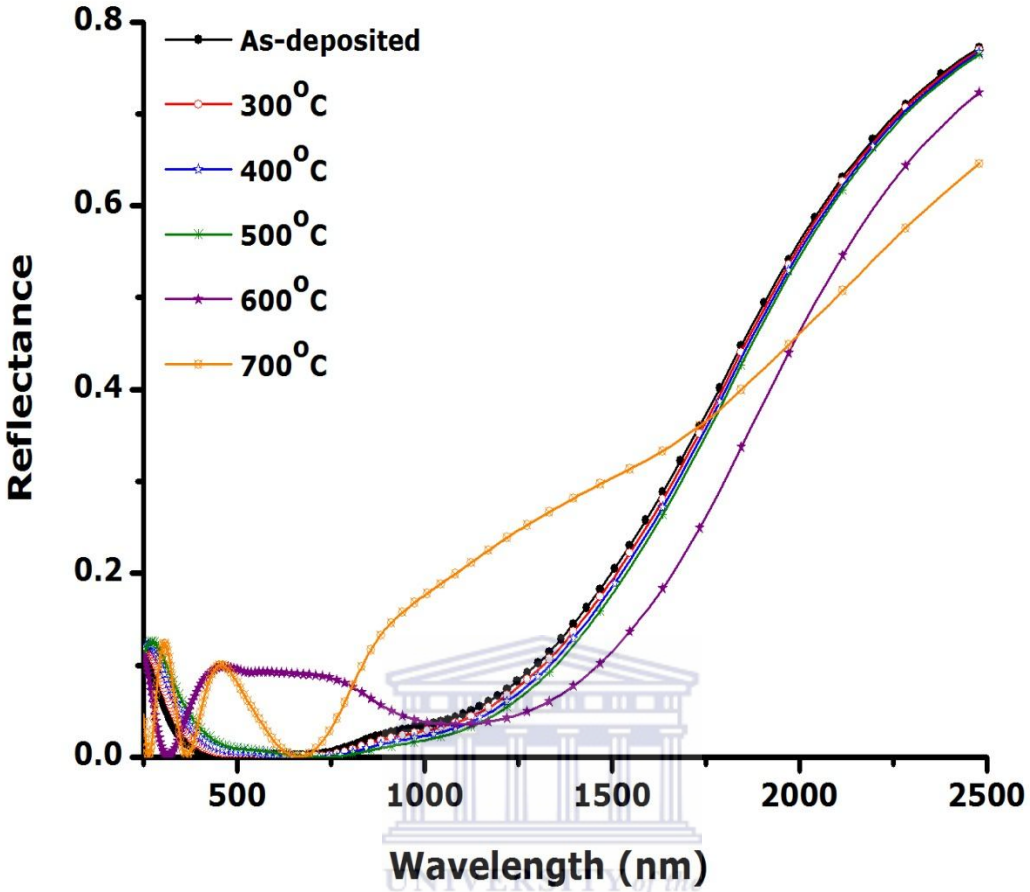

Figure 5: Reflectance spectra of $Al_xO_y/Pt/Al_xO_y$ multilayer solar absorber coatings as-grown and heat treated in air for 2 h.

The reflectance of the as-deposited multilayer solar absorber was about 5% in the visible near infrared region and increased sharply from 1100 nm and reflected 80% at around 2500 nm. The reflectance of the coating annealed at 300ºC showed absorptance $(\Delta\alpha = 0)$ and emittance $(\Delta\varepsilon = +0.01)$. With the increase of heat treatment temperature up to 500ºC, the spectral reflectance exhibited no significant change in the vis-NIR wavelengths with a change in absorptance $(\Delta\alpha = -0.001)$ and emittance $(\Delta\varepsilon = +0.01)$ values. This indicates that $Al_xO_y/Pt/Al_xO_y$ multilayer solar absorber have good thermal stability up to 500°C in air, which

is attributed to the high temperature thermal stability of Al_2O_3 that acts as a diffusion barrier for oxygen and to the unreactive Pt metal, which resist oxidation and chemical reaction [4.32]. According to Barshilia *et.al* [4.14], Al_2O_3 based solar selective coatings deposited onto quartz, stainless steel, superalloy and molybdenum substrates are thermally stable in air up to 500°C. Hence it is worth to mention, $Al_xO_y/Pt/Al_xO_y$ multilayer solar absorber coatings deposited onto copper substrates appeared to be thermally stable in air up to 500°C.

The reflectance increase below 1000 nm and the cut off shifted towards the higher wavelength at 600°C. The absorptance value decreased $(\Delta\alpha = -0.032)$ and the emittance value increased $(\Delta\varepsilon = +0.02)$. At 700°C, it was found a total change in the shape and values of the reflectance. Consequently, the absorptance $(\Delta\alpha = -0.104)$ and emittance $(\Delta\varepsilon = +0.03)$ values of the multilayer coatings changed significantly, indicating the degradation of the multilayer absorber. Hence in order to elucidate the mechanism behind the degradation of the coatings above 500°C, the experimental reflectance spectra were fitted with an optical simulation program called SCOUT by using the model presented [4.20]. From the fit to the experimental reflectance curves the thickness and the constituents of the $Al_xO_y/Pt/Al_xO_y$ multilayer solar absorber coatings as-deposited and annealed up to 500°C didn't show significant change. The coatings were Al_xO_y ~ 90 nm / Pt ~ 8 nm / Al_xO_y ~ 39 nm/ Cu substrate. However for the multilayer solar absorbers annealed at 600°C and 700°C, the thickness and the constituents of the layers were different from the other samples. The sample annealed at 600°C was comprised of 37% Cu: 63% Al_xO_y top layer ~ 79 nm , 26% Cu: 84%Pt middle layer ~ 3 nm and 66% Cu: 34%Al_xO_y base layer ~ 28 nm and same goes to the sample annealed at 700°C. It was comprised of 49% Cu: O 51% top layer ~ 18 nm thick, 83% Cu: 17% Al_xO_y middle layer ~ 60 nm , and base 92% Cu: 8% Al_xO_y base layer ~ 28 nm. Hence one can observe that the main

degradation mechanism of the $Al_xO_y/Pt/Al_xO_y$ multilayer absorber is attributed to the diffusion of copper towards the surface.

The microstructural stability of the $Al_xO_y/Pt/Al_xO_y$ multilayer solar absorber coatings was studied using Raman spectroscopy. The Raman spectra of the as-deposited and annealed up to 700^oC in air are shown in Fig 6. The as-deposited multilayer absorber exhibited two broad bands centered at 190 and 833 cm^{-1}, which corresponds to the vibration of aluminium and oxygen atoms, respectively. The shape of Raman spectra didn't show significant change even after annealed the sample up to 600^oC, indicating the stable structure of the multilayer solar absorber coatings. However, at 700^oC, the two bands disappeared and three peaks centered at around 211, 296 and 621cm^{-1} appeared, which correspond to the formation of CuO and Cu_2O [4.39]. These phases of copper appeared due to the outward diffusion of copper in to the coating.

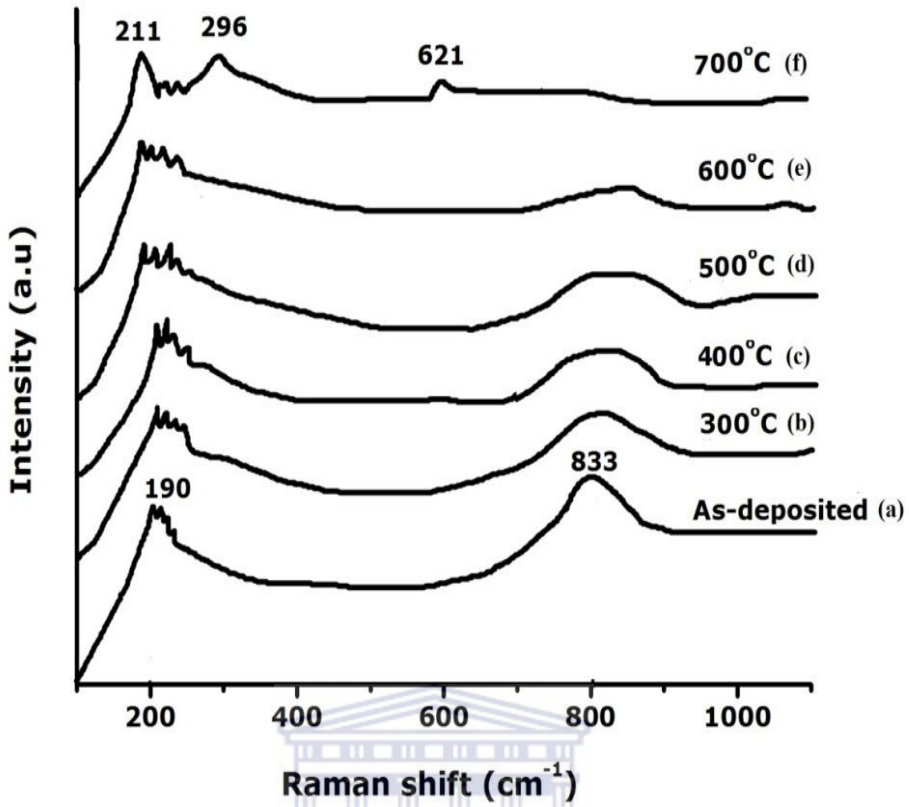

Figure 6: Raman spectra of $Al_xO_y/Pt/Al_xO_y$ multilayer solar absorber coatings as-grown (a), and annealed at different temperatures in air for 2 h: 300°C (b), 400°C (c), 500°C (d), 600°C (e), and 700°C (f).

4.3.5 Long term thermal stability in air

Long term thermal stability is also the most important criteria for use the solar absorber material for concentrating solar-thermal applications. The $Al_xO_y/Pt/Al_xO_y$ multilayer solar absorber coatings were heat treated in air at 350°C, 450°C and 550°C for 24 h. Fig. 7 shows the reflectance spectra of the multilayer coatings in the as-deposited state and annealed for 24 h. The absorptance and emittance values are shown in Table 3.

Temperature (°C)	Absorptance (α)			Emittance (ε at 82°C)		
	As-deposited	Annealed	$\Delta\alpha$	As-deposited	Annealed	$\Delta\varepsilon$
Room temperature	0.960	-	-	0.07	-	-
350	0.960	0.960	-	0.07	0.07	-
450	0.962	0.963	+0.001	0.07	0.08	+0.01
550	0.960	0.803	-0.157	0.07	0.09	+0.02

Table 3: Effect of annealing in air for 24 h on solar absorptance and thermal emittance values of the $Al_xO_y/Pt/Al_xO_y$ multilayer solar absorber deposited onto Cu substrate.

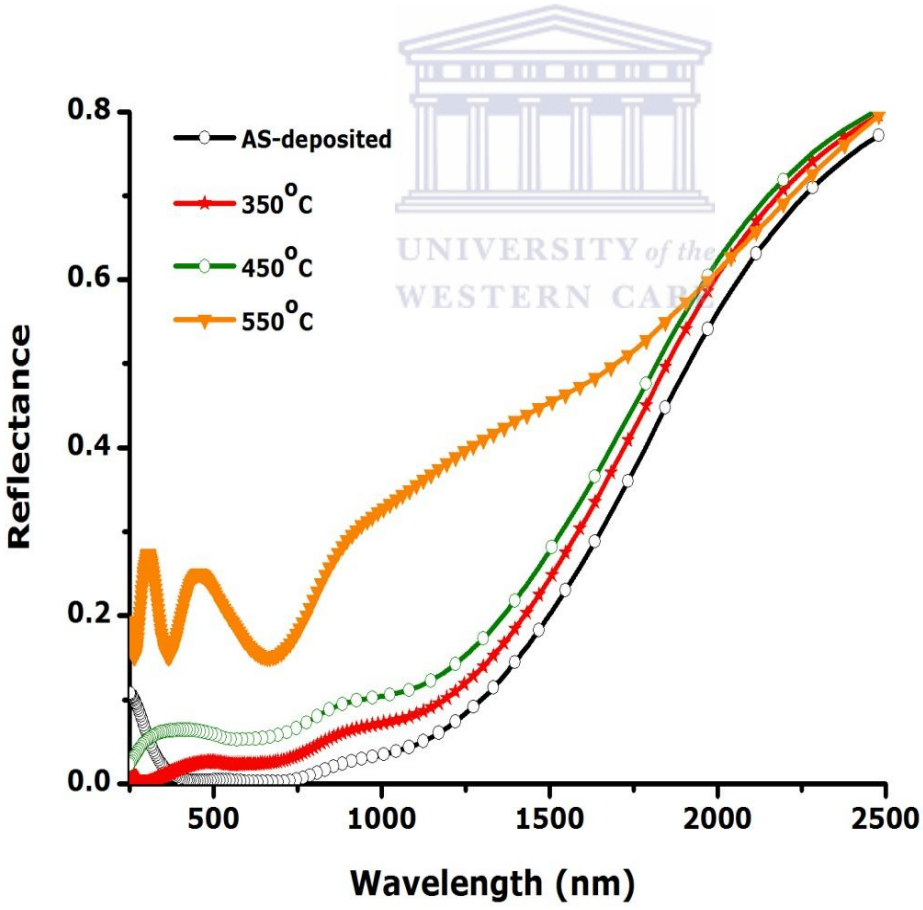

Figure 7: Reflectance spectra of $Al_xO_y/Pt/Al_xO_y$ multilayer solar absorber coatings as-grown and heat treated in air for 24 h.

It is evident from the table that the change in absorptance $(\Delta\alpha = 0.000, +0.001)$ and emittance $(\Delta\varepsilon = +0.00, +0.01)$ values of the coating at 350°C and 450°C respectively was not substantial. However, at 550°C the absorptance decreased $(\Delta\alpha = -0.157)$ and the emittance increased $(\Delta\varepsilon = +0.02)$ drastically. The XRD pattern showed formation of CuO and Cu_2O phases at 550 °C, which is shown in Fig. 8.

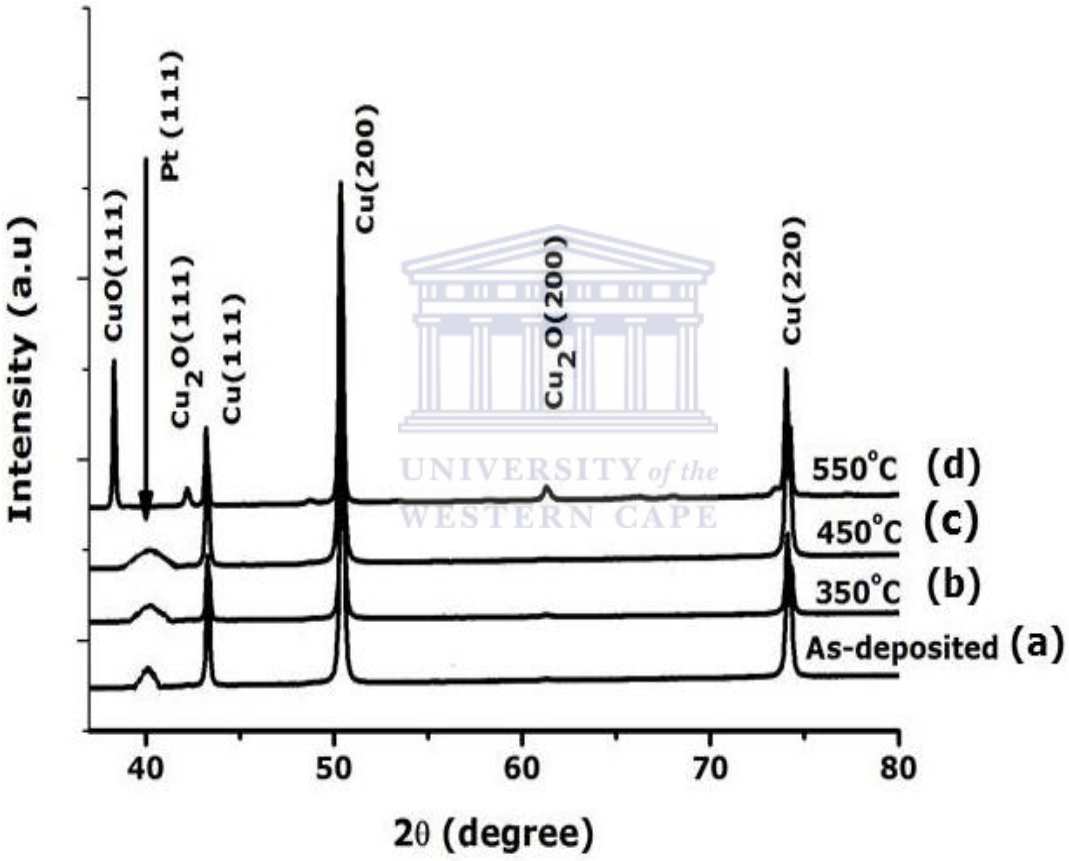

Figure 8: XRD pattern of $Al_xO_y/Pt/Al_xO_y$ multilayer solar absorber coatings as-grown (a) and annealed at different temperatures in air for 24 h: 350°C (b), 450°C (c) and 550°C (d).

The AFM images of $Al_xO_y/Pt/Al_xO_y$ multilayer solar absorber coating in the as-deposited state and heat treated at 350^{o}C, 450^{o}C, and 550^{o}C in air for 24 h showed a slight increase in average roughness value as shown in Fig. 9.

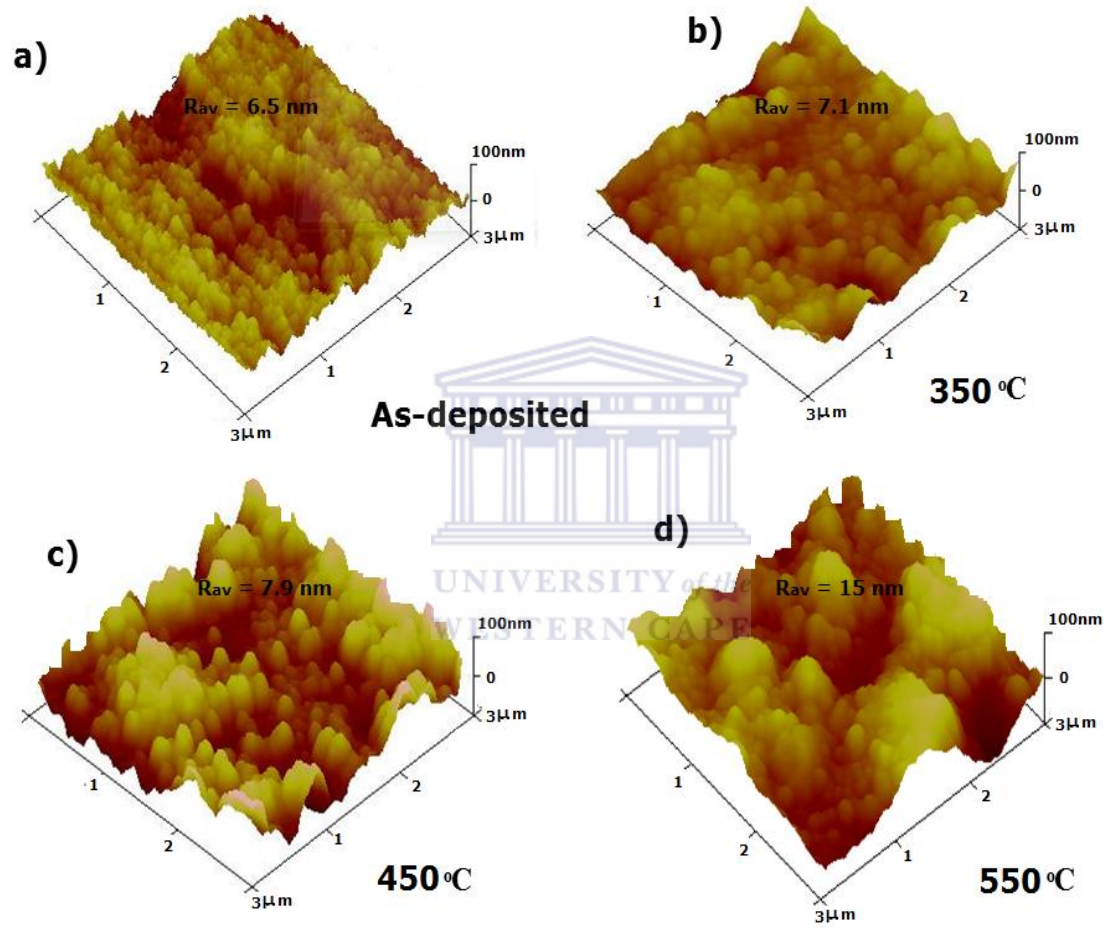

Figure 9: AFM images of $Al_xO_y/Pt/Al_xO_y$ multilayer solar absorber coatings as-grown (a) and annealed at different temperatures in air for 24 h: 350^{o}C (b), 450^{o}C (c) and 550^{o}C (d).

The representative Raman spectra (Fig. 10) also confirmed that there was no significant change in microstructure of the multilayer absorber up 450^{o}C but at 55^{o}C, CuO and Cu_2O was

appeared. Therefore, diffusion of Cu and formation of its oxide phases, are responsible for the degradation of $Al_xO_y/Pt/Al_xO_y$ multilayer solar absorber coatings.

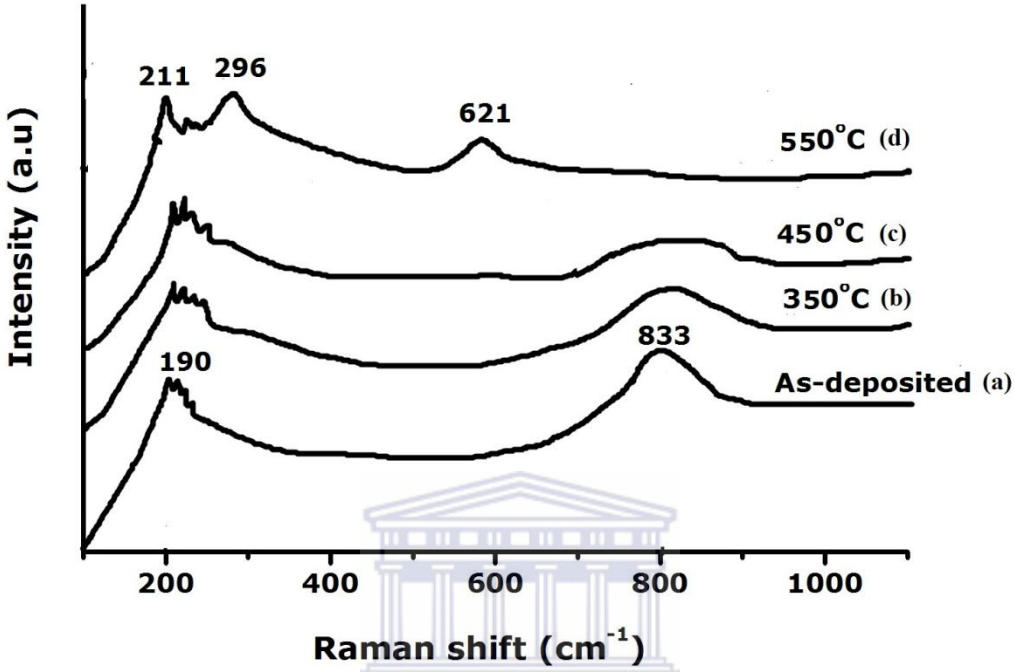

Figure 10: Raman spectra of $Al_xO_y/Pt/Al_xO_y$ multilayer solar absorber coatings as-grown (a) and annealed at different temperatures in air for 24 h: 350°C (b), 450°C (c) and 550°C (d).

In general, it is observed that the major degradation of $Al_xO_y/Pt/Al_xO_y$ multilayer solar absorber coatings was diffusion of copper towards the surface. Hence, it is worth to mention that this multilayer absorber could further improve its thermal stability if a diffusion barrier layer is deposited between the base Al_xO_y layer and copper substrate.

4.4 CONCLUSION

$Al_xO_y/Pt/Al_xO_y$ multilayer solar absorber films have been deposited onto a copper substrate at room temperature using e-beam vacuum evaporator. The multilayer absorber was annealed in air for different temperatures and durations. XRD analysis showed a decrease in the intensity of Pt grain for the multilayers heated from 300 – 600^{o}C in air for 2 h, and completely disappeared and formed CuO and Cu_2O phases at 700^{o}C. This was also confirmed by Raman spectroscopy. A slight increase in the mean size of Pt particles was observed from the samples heated from 300 – 500^{o}C in air for 2 h. The average surface roughness of the multilayers was found to increase slightly with annealing temperature. EDS and optical modelling spectra confirmed formation of oxidized copper and the disappearance of Pt. The optical property of $Al_xO_y/Pt/Al_xO_y$ in air for 2 h was found to be stable up to 500^{o}C, with solar selectivity α/ε of 0.951/0.09. At 600^{o}C and 700ºC, its selectivity decreased significantly to (0.92/0.10) and 0.846/0.11, respectively, which is attributed to the diffusion of copper and formation of CuO and Cu_2O phases. Long term annealing showed that the multilayer coating was stable up to 450^{o}C in air for 24 h and showed spectral selectivity of 0.963/0.08.

4.5 REFERENCES

4.1 M. A. signore, A. Sytchkova, A. Rizzo, opt. Mater. 34 (2011) 292-297.

4.2 M. Maaza, O. Nemraoui, C. Sella , J. Lafait, A. Gibaud, V. Pischedda, , Phys. Lett. A 344 (2005) 57-63.

4.3 M. Maaza, O. Nemraoui, C. Sella, J. Lafait, A. Gibaud, B. Baruch-Barak, A. C. Beye, Solid Sta. Comms. 137 (2006) 166-170.

4.4 Z. Y. Nuru, C. J. Arendse, R. Nemutudi, O. Nemraoui, M. Maaza, Physica B, 407 (2012) 1634–1637.

4.5 W. F. Bogaerts, C. M. Lampert, J. Mater. Sci. 18 (1983) 2847 – 2875.

4.6 Q. C. Zhang, D. R. Mills, Sol. Energy Mater. Sol. Cells 27 (1992) 273-290.

4.7 C. Nunes, V. Teixeira, M. Collares-Pereira, A. Monteiro, E. Roman, J. Martin-Gago, Vacuum 67 (2002) 623–627.

4.8 T. Tesfamichael, A. Roos, Sol. Energy Mater. Sol. Cells 54 (1998) 213-221.

4.9 C. E. Kennedy, ‘‘Review of Mid- to High-Temperature Solar Selective Absorber Materials’’, NREL/TP-520-31267, (2002).

4.10 M. Okuyama, K. Furusawa, Y. Hamakaa, Sol Energy 22 (1979).

4.11 Q. C. Zhang, Sol. Energy Mater. Sol. Cells, 62 (2000) 63-73.

4.12 A. Antonaia, A. Castaldo, M. L. Addonizio, S. Esposito, Sol. Energy Mater. Sol. Cells, 94 (2010) 1604-1611.

4.13 C. Kennedy and H. Price, ‘‘Development and testing of high- temperature solar selective coatings’’, NREL/CP-520-36581, (2005).

4.14 Harish C. Barshilia, N. Selvakumar, G. Vignesh, K. S. Rajam, A. Biswas, Sol. Energy Mater. Sol. Cells, 93 (2009) 315-323

4.15 N. Selvakumar, Harish C. Barshilia, K. S. Rajam, A. Biswas, Sol. Energy Mater. Sol. Cells, 94 (2010) 1412-1420.

4.16 J. A. Thornton, S. Alans. J. Penfold, L Lamb, Thin Solid Films 72 (1980) 101-110.

4.17 H. Lei, W. Shumao, J. Lijun, L. Xiaopeng, L. Hualing, L. Zhinian, Chinese Science Bulletin 54 (2009) 1451-1454.

4.18 H. Lie, D. Miao, L. Xiaopeng, W. Shumao, J. Lijun, L. Fang, L. Zhinian, M. Jing, Science china Technological sciences 53 (2010) 1507 – 1512.

4.19 Y. Liu, C. Wang, Y. xue, Sol. Energy Mater. Sol. Cells, 96 (2012) 131-136.

4.20 Z. Y. Nuru, C. J. Arendse, S. Khamlich, M. Maaza, Vacuum 86 (2012) 2129-2135.

4.21 H. G. Craighead, R. Bartynsky, R. A. Buhrman, Sol. Energy Mater. 1 (1979) 105 -124.

4.22 J. A. Thornton, J. L. Lamb,Thin Solid Films 96 (1982) 175-183.

4.23 J. A. Thornton and J. L. Lamb,Sol. Energy Mater. 9 (1984) 415-431.

4.24 C. Sella, T. K. Vien, J. Lafait, S. Berthier, Thin Solid films 90 (1982) 425-431.

4.25 T. K. Vien, C. Sella, J. Lafait, S. Berthier, Thin Solid Films 126 (1985) 17-22.

4.26 N. Selvakumar, H. C. Barshilia, Sol. Energy Mater. Sol. Cells, 98 (2012) 1-23.

4.27 H. C. Barshilia, N. Selvakumar, K. S. Rajam, Journal of Vacuum Science and Tec A 25 (2007) 383-390.

4.28 H. C. Barshilia, N. Selvakumar, K. S. Rajam, A. Biswas, Sol. Energy Mater. Sol. Cells, 92 (2008) 1425-1433.

4.29 H. C. Barshilia, N. Selvakumar, K. S. Rajam, A. Biswas, Narosa Publishing House, (2008), 469-477.

4.30 N. Selvakumar, N. T. Manikandanath, A. Biswas, Harish. C. Barshilia, Sol. Energy Mater. Sol. Cells, 102 (2012) 86- 92.

4.31 L. Rebouta' A. Pitães' M. Andritschky, P. Capela, M. F. Cerqueira, A. Matilainen, K. Pischow, Surface and Coatings Technology 211 (2012) 41-44

4.32 D. Xinkang, W. Cong, W. tianmin, Z. Long, C. Building, R. Ning, Thin Solid Films 516 9 (2008) 3971-3977.

4.33 Z. Y. Nuru, C. J. Arendse, T. F. G. Muller, M. Maaza, Mater. Sci. Eng., B 177 (2012) 1188-1193.

4.34 Theiss, W., ‘‘SCOUT optical spectrum simulation, M. Theiss Hard- and Software’’, Achen, (2002).

4.35 H. Arashi, J. Am. Ceram. Soc, 75 (1992) 844-847.

4.36 A. Mortensen, D. H. Christensen, O. F. Nielsen, E. Pedersen, J. Raman Spectosc. 22 (1991) 47 – 49.

4.37 A. Misra, H. D. Bist, M. S. Navati, R. K. Thareja, J. Narayan, Mater. Sci. Eng. B 79 (2001) 49-54.

4.38 R. B. Pettit, SAND-75-0079, Albuquerque, NM: Sandia National Laboratory, 1975.

4.39 Di Chen, Guozhen Shen, Kaibin Tang, Yitai Qian, J. Crys. Growth 254 (2003) 225–228.

CHAPTER FIVE

HEAVY ION ELASTIC RECOIL DETECTION ANALYSIS OF $Al_xO_y/Pt/Al_xO_y$ MULTILAYER SELECTIVE SOLAR ABSORBERS

ABSTRACT

An $Al_xO_y/Pt/Al_xO_y$ multilayer solar absorber for use in solar-thermal applications has been deposited onto copper substrate by electron beam (e-beam) vacuum evaporation at room temperature. Different samples were annealed at different temperatures in air and characterized by spectrophotometry, emissometry, Heavy Ion Elastic Recoil Detection Analysis (HI-ERDA), X-ray diffraction (XRD) and energy-dispersive X-ray spectroscopy (EDS). The $Al_xO_y/Pt/Al_xO_y$ multilayer solar absorbers heated up to 500^oC were found to exhibit good spectral selectivity α/ε of 0.951/0.08. However, beyond 500ºC the spectral selectivity decreased to 0.846/0.11, possibly due to thermally activated atomic interdiffusion profiles. HI-ERDA has been used to study depth-dependent atomic concentration profiles. These measurements revealed outward diffusion of the copper substrate towards the surface and therefore, the decrease in the constituents of the coating.

The content of this chapter was published in: Applied surface science (2014), http://dx.doi.org/10.1016/

5.1 INTRODUCTION

A spectrally selective $Al_xO_y/Pt/Al_xO_y$ multilayer solar absorber deposited using an electron beam (e-beam) evaporator onto a Cu substrate has previously been presented [5.1, 5.2]. The multilayer solar absorber consists of a middle Pt layer sandwiched between two layers of Al_xO_y. The Pt metal layer is semi-transparent to the incoming solar radiation and the Al_xO_y layers behave as a resonant cavity tuned to a band of solar radiation wavelengths. An ideal spectrally selective surface should have one solar absorptance and zero thermal emittance. The solar absorptance of the $Al_xO_y/Pt/Al_xO_y$ multilayer solar absorber coating is 0.94 and thermal emittance is about 0.06.

To enhance the energy conversion efficiency, thermal stability of selective solar absorbing coatings is critical. Some multilayer absorbers have been reported [5.3-5.6]. However, most of the coatings do not have the desired thermal stability and performance at high operating temperatures in air in case the vacuum is breached [5.7]. The main cause of degradation of multilayer solar absorber coatings at high temperature is thermally activated diffusion between the layers and the substrate [5.8]. Therefore, the main point of this study was to understand the diffusion process with a view to improve the thermal stability of the multilayer coatings. To investigate the depth profile of the $Al_xO_y/Pt/Al_xO_y$ multilayer solar absorber, a technique that measures both light and heavy element components was required, as the above mentioned multilayer solar absorber includes atoms ranging from an atomic weight of 15.9994 (oxygen) to 195.078 (Platinum).

Heavy Ion-Elastic Recoil Detection Analysis (ERDA) is a powerful technique to determine the depth profiles of light and heavy elements simultaneously [5.9-5.11]. A few selective solar

absorbers such as TiN_xO_y, $AlCu_xFe_y$ and Ni-Al_2O_3/SiO_2 have been studied using this technique [5.12, 5.13].

The aim of this chapter is to characterise the depth profile of $Al_xO_y/Pt/Al_xO_y$ multilayer solar absorber for use in high temperature concentrators in solar power applications. We present the effect of heat treatment on the depth profile and optical properties of spectrally selective $Al_xO_y/Pt/Al_xO_y$ multilayer coatings, which were heated in air at different temperatures. HI-ERDA, spectrophotometery and emissometery, and are used to characterize the multilayer solar absorber samples.

5.2 EXPERIMENTAL DETAILS

$Al_xO_y/Pt/Al_xO_y$ multilayer solar absorber stacks of 900 Å Al_xO_y top layer, 70 Å Pt middle layer and 400 Å Al_xO_y base layer were deposited onto copper ($3 \times 3cm^2$) substrates using a 3 kW high vacuum e-beam evaporation system at room temperature. The experimental details are described elsewhere [5.1, 5.2].

To study the thermal stability of the multilayer solar absorber coatings, five sample pieces were heated in air in an ultra-Furnace of Wirsam Scientific type UF12/40/200, for 2 h each. The annealing temperature ranged from 300 to 700^oC at an increment of 100^oC. The temperature was ramped up from room temperature to the desired temperature at a rate of 5^oC/min and was cooled down at a rate of 2 ^oC/min. The accuracy of the set temperature was ± 7 ^oC.

For optical characterization, spectral reflectance of the heat treated multilayers was measured with a Cary 5000 UV–vis–NIR spectrophotometer of Varian, Inc. model internal DRA-2500 in

the wavelength range of 0.3–2.5 µm. The solar absorptance was calculated from the measured reflectance data and weighted by solar irradiance using standard AM1.5 solar spectrum in the above wavelength range. Thermal emittance spectra were acquired by an emissometer model AE1, which has an accuracy of ± 0.01 emittance units. X-ray diffraction (XRD) data of the annealed coatings were recorded by using Model Bruker AXS D8 advance of radiation Cu (K_α = 1.5406 Å). The chemical composition was studied using energy-dispersive X-ray spectroscopy (EDS) using an accelerating voltage of 15kV.

Key structural characterization entailed using Heavy Ion ERDA to monitor the change with temperature in the multilayer solar absorber elemental depth profile. The Heavy Ion ERDA technique consists in the detection of recoil ions knocked off the surface region of a target sample by a (heavy) projectile beam coming in at a grazing incidence angle to the sample surface. In our experimental set up, coincident measurement of the time of flight and energy of the recoil ions leads to their separation according to mass. The result is that of 2-D scatter plots showing different contour lines (see Fig. 1) each corresponding to a particular ion mass, from which elemental energy spectra and thence depth profiles can be extracted [5.14].

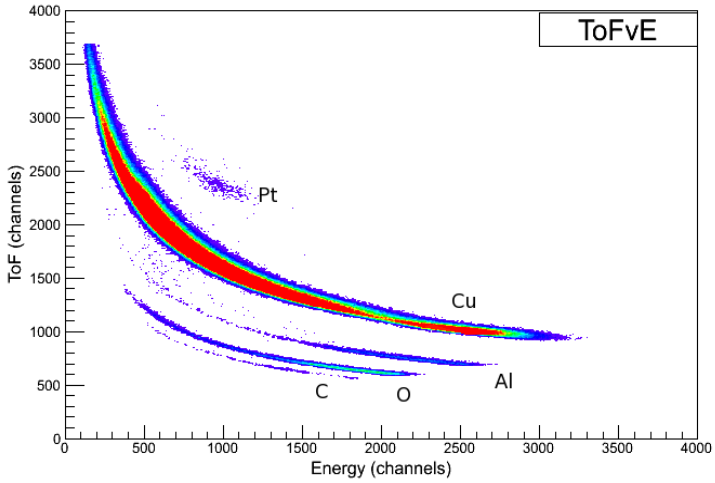

Figure 1: A 2-D ToF-Energy scatter plot of raw counts from the measurement of $Al_xO_y/Pt/Al_xO_y$ multilayer absorber heated at 300^oC in air for 2 h.

Fig. 1 shows raw data in the form of a 2-D Time of Flight vs. Energy scatter plot of atomic species from the Al_xO_y / Pt /Al_xO_y multilayer heated at 300^oC in air for 2 h. Data processing involves selecting regions of individual mass contours and projecting each onto the ToF axis to get elemental time of flight spectra. Knowing the mass of each atomic species and the length of the flight path (0.60 m), the individual ToF spectra are then converted to energy spectra.

Depth profiles are obtained through a direct conversion code, KONZERD [5.15]. In brief KONZERD employs a method known as slab analysis, where a sample structure is divided into a large number of slabs of equal thickness in which sample composition, stopping power and recoil and scattering cross-sections are all assumed to be constant across each slab, but varying from slab to slab. Starting from the surface an arbitrary elemental composition is assumed in the first slab layer and an energy bin corresponding to the slab thickness calculated for each detected recoil species. In the calculation Bragg's additivity rule is used to determine effective stopping powers using the assumed proportions of the different elements present in the slab layer. The experimental yield for each ion species within this calculated energy bin is then used to calculate new values of the elemental concentrations in the same slab layer using Rutherford cross-sections. The new concentrations are then used to re-do the calculation from the beginning. This procedure is repeated until convergence to self-consistent concentration values and then the whole process is repeated for all the subsequent slabs. In this way the concentration profiles are calculated directly.

The one limitation of this method is that the profiles derived are, strictly speaking, not purely concentration depth profiles since they still have the system energy resolution convoluted and so one has to live with the limited depth resolution given by the experimental conditions. In our

iThemba LABS set up, the surface depth resolution currently ranges from about 4.0 to 10 nm for light to heavy ions, respectively.

The current beam transport settings at our iThemba LABS Gauteng tandem accelerator limit the heaviest incident beam available for ERD analyses to 26 MeV $^{63}Cu^{7+}$, and this is the beam that was used, at 15° grazing incidence angle. The detector system, a mass dispersive ToF–energy spectrometer, was mounted at 30° ± 0.5^{o} to the incident beam direction. To circumvent the problem of interference of Cu signals due to the scattered beam ions with those due to the recoiled Cu substrate atoms there was need to separate the contributions of the scattered and recoil ions to the total Cu spectrum. The ratio of the scattering σ_s to the recoil σ_r cross-section at the same angle ϑ, for identical projectile and target atoms, works out to be a function of that angle;

$$\frac{\sigma_s}{\sigma_r} = f(\vartheta) = \frac{\cos^4 \vartheta}{\sin^4 \vartheta} \qquad 5.1$$

For ϑ = 30^{o}, $f(\vartheta) = 9$, and this ratio was used to calculate the recoil portion of the total Cu spectrum. The uncertainty in the scatter/recoil angle leads to an upper limit of 8.4% in the uncertainty of the Cu recoil yield calculated this way.

5.3 RESULTS AND DISCUSSION

Thermal stability is critical for solar absorber materials as it affects the two basic characteristics i.e. solar absorptance and thermal emittance of the solar absorber material.

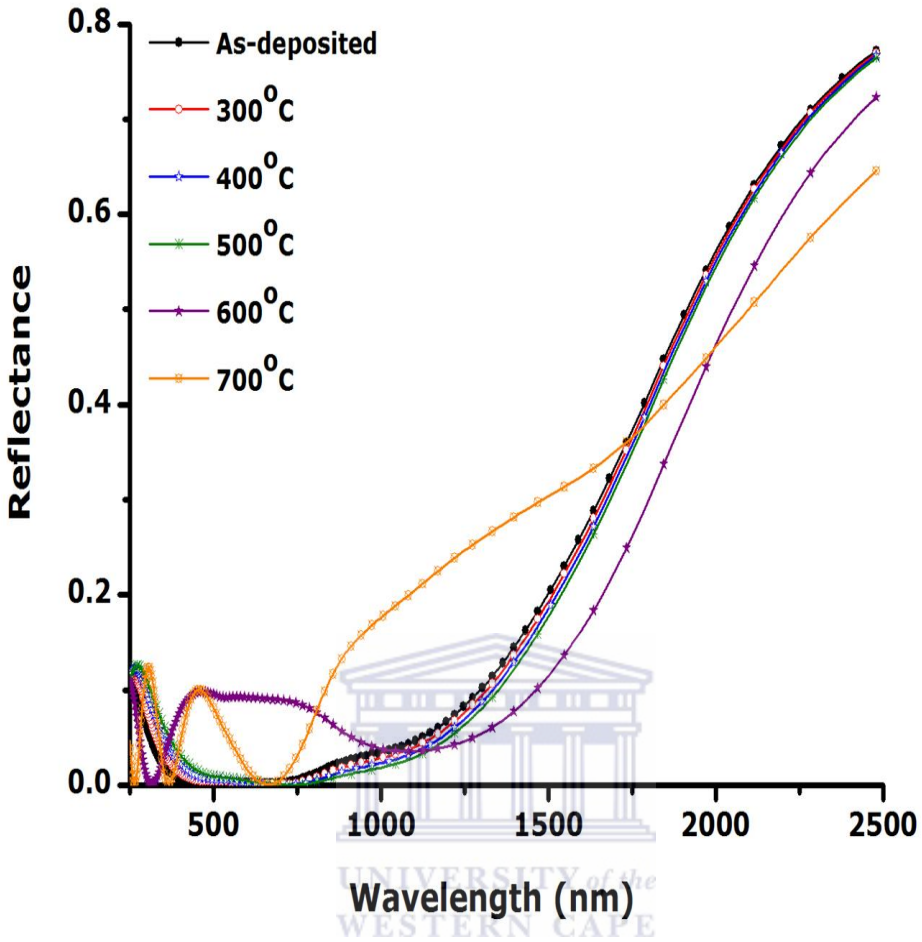

Figure 2: Reflectance spectra of $Al_xO_y/Pt/Al_xO_y$ multilayer absorber as-deposited and heat treated in air for 2 h.

The corresponding absorptance and emittance values of the multilayer coatings are given in Table 1. To achieve high solar selectivity, the coatings should exhibit low reflectivity in the visible near infrared (vis-NIR) region but high in the infrared region.

Temperature (°C)	Absorptance (α)			Emittance (ε, at 82°C)		
	As-deposited	Annealed	Δ	As-deposited	Annealed	Δε
Room temperature	0.952	-	-	0.08	-	-
300	0.952	0.952	-	0.08	0.09	+0.01
400	0.952	0.951	-0.001	0.08	0.09	+0.01
500	0.952	0.951	-0.001	0.08	0.09	+0.01
600	0.952	0.920	-0.032	0.08	0.10	+0.02
700	0.950	0.846	-0.104	0.08	0.11	+0.03

Table 1: Effect of annealing in air for 2 h on solar absorptance and thermal emittance values of the $Al_xO_y/Pt/Al_xO_y$ multilayer solar absorber deposited onto Cu substrate.

In Fig. 2, the reflectance of the as-deposited multilayer solar absorber coatings was about 5% in the visible near infrared region, ranging from 300-1000 nm and increased sharply from 1100 nm and reflected 80% at around 2500 nm. The reflectance of the coating annealed at 300 °C showed absorptance $(\Delta\alpha = 0)$ and emittance $(\Delta\varepsilon = +0.01)$. With the increase of heat treatment temperature up to 500 °C, the spectral reflectance exhibited no change in the vis-NIR wavelengths with a change in absorptance $(\Delta\alpha = -0.001)$ and emittance $(\Delta\varepsilon = +0.01)$ values.

On the other hand, the reflectance increase below 1000 nm and the cut off shifted towards the higher wavelength at 600°C. The absorptance value decreased $(\Delta\alpha = -0.032)$ and the emittance value increased $(\Delta\varepsilon = +0.02)$. And at 700°C, it was found that there was a total change in the shape and values of the reflectance. Consequently, the absorptance $(\Delta\alpha = -0.104)$ and emittance $(\Delta\varepsilon = +0.03)$ values of the multilayer coatings changed significantly, indicating the degradation of the multilayer solar absorber. Hence in order to gain more insight into the degradation mechanism of the $Al_xO_y/Pt/Al_xO_y$ multilayer absorber

coatings, it was of interest to use Heavy Ion -ERDA to determine the depth profile of the coatings.

Fig. 3 shows Heavy Ion -ERDA relative atomic depth profile of the Al_xO_y / Pt /Al_xO_y multilayer solar absorber deposited onto Cu substrate, heated at 300^oC, in air for 2 h. It can be seen from Fig 3 the average atomic fraction ratio of aluminum –to- oxygen relation at the first 90 nm of Al_xO_y/Pt/Al_xO_y multilayer absorber is roughly 0.38:0.6 and thereafter, reduction of the relative atomic fraction with depth is observed. What can be noted in Fig. 3 is that a mixed layer of aluminum, oxygen and platinum with an atomic fraction of about 20 % , 45 % and 5 % respectively is found at around 100-130 nm. This is due to the slight bilayer diffusion of the layers, which formed a Pt-Al_2O_3 composite that keeps the absorptivity of the material. Since the base Al_xO_y is thinner, the reduction in atomic fraction of aluminum and oxygen can be expected. Apparently, the base Al_xO_y layer was not able to prevent diffusion of copper. As a result, a small amount of copper substrate diffused towards the interface to the base Al_xO_y layer. However, this small amount of copper did not affect the absorptivity and emissivity of the coatings. The carbon atomic fraction (10 %) appearing at the surface and at the interface of the substrate (5 %) is attributed to the exposure to an ambient air and it does not affect the optical property of the multilayer solar absorber.

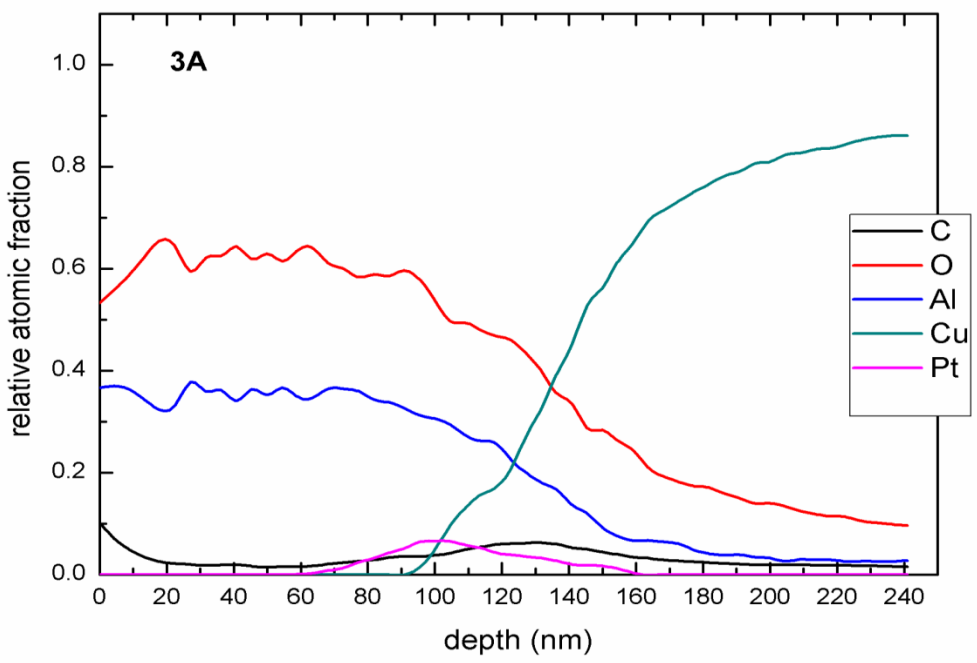

Figure 3: Elemental depth analysis of $Al_xO_y/Pt/Al_xO_y$ multilayer absorber heated at 300^oC in air for 2 h.

The depth profile analysis of the $Al_xO_y/Pt/Al_xO_y$ multilayer solar absorber heated at 400^oC in air is shown in Fig. 4. Similarly the relative atomic fraction ratio of aluminum-to-oxygen in the first 90 nm was about 0.36:0.61 ± 0.03 and then a reduction in concentration with depth were also observed, but to lesser extent as oxygen and aluminum seem to have diffused slightly into the substrate. Compared to the sample heated at 300^oC, no significant changes were observed.

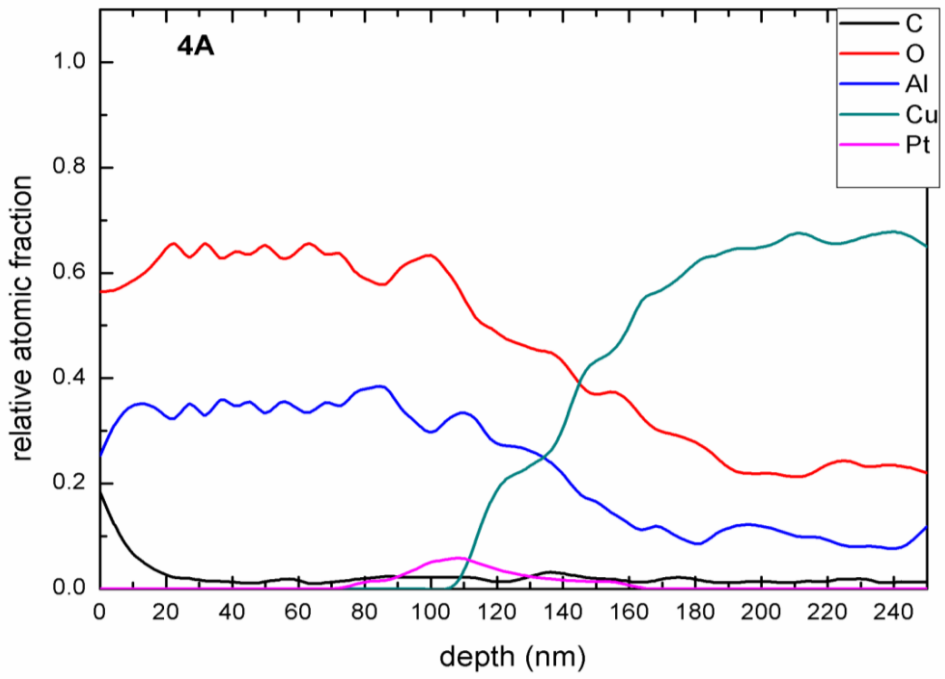

Figure 4: Elemental depth analysis of $Al_xO_y/Pt/Al_xO_y$ multilayer absorber heated at 400°C in air for 2 h.

The change of relative atomic fraction with depth for the 500°C heat-treated sample is shown in Fig. 5. After heat treatment at 500°C, the profiles of aluminum, oxygen and platinum showed the same behavior like the coatings heated at 300°C and 400°C. When looking at copper though, it has slowly migrated toward the surface of the multilayer coating. This relatively small diffusion of copper still does not result in any significant change on the optical property of the coating (Fig. 2).

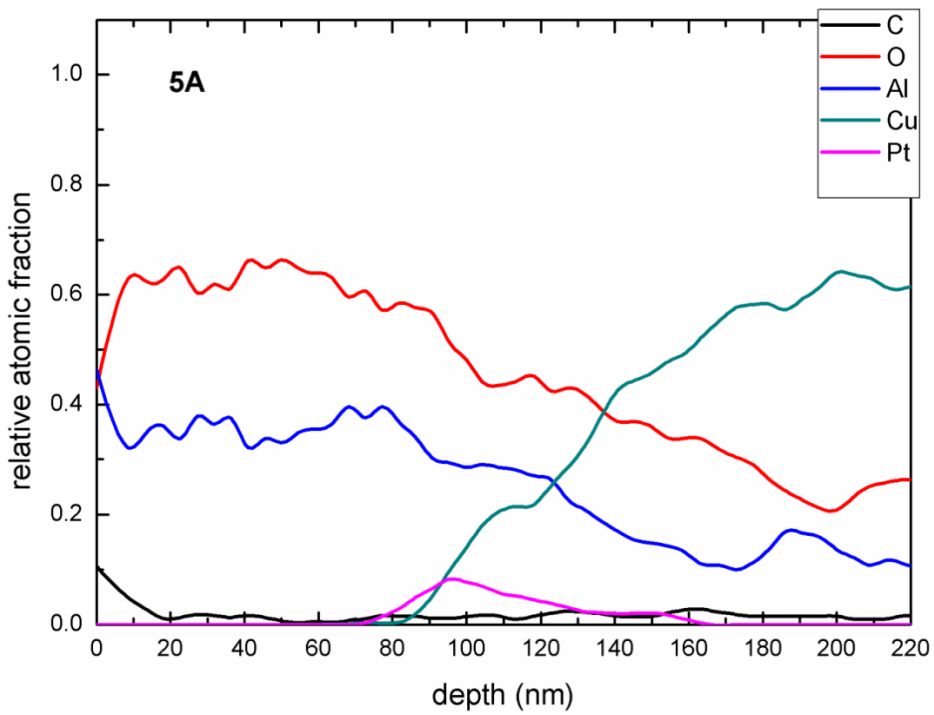

Figure 5: Elemental depth analysis of $Al_xO_y/Pt/Al_xO_y$ multilayer absorber heated at 500^oC in air for 2 h.

Fig. 6 depicts the depth profile of the sample heated at 600^oC in air for 2 h. It can be seen that after annealing at 600^oC, the surface layer, though still Al_xO_y rich, now contains some copper, and below the surface the copper concentration increases gradually. This means that the base Al_xO_y and the middle Pt layer are dominated by the concentration of copper substrate, due to the outward diffusion of copper. Consequently the reflectance curve (Fig. 2) of the multilayer coating increases in the solar spectrum region, which leads to a decrease in solar absorptance, which is attributed to metallic behavior.

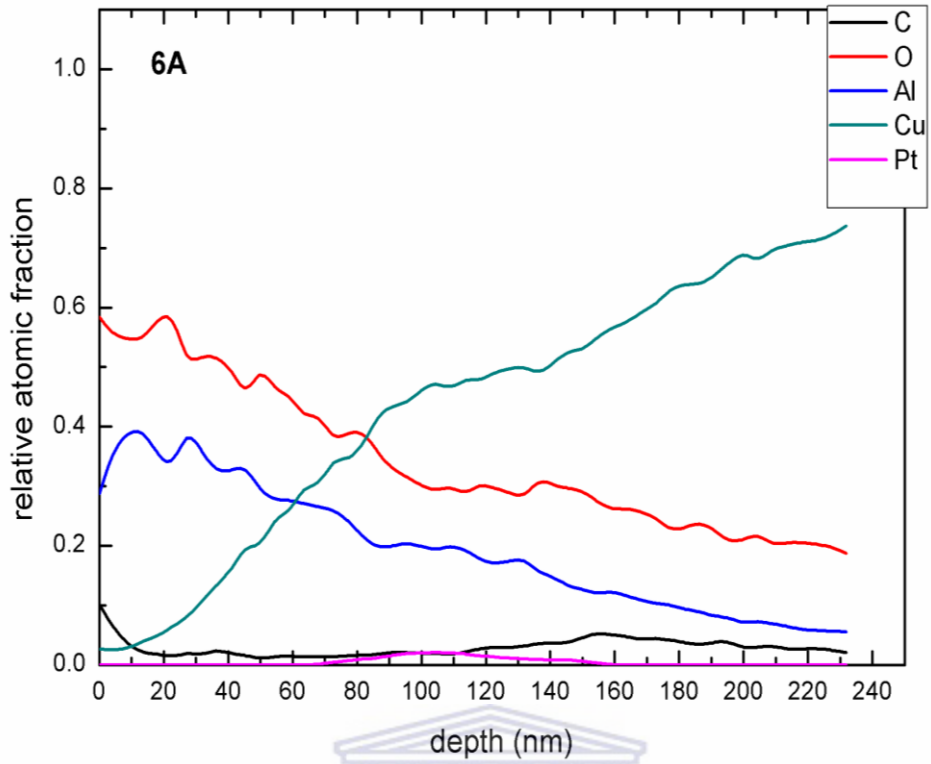

Figure 6: Elemental depth analysis of $Al_xO_y/Pt/Al_xO_y$ multilayer absorber heated at 600°C in air for 2 h.

Fig. 7 displays the depth profile obtained for the sample annealed at 700ºC. It is evident that the obtained result is somewhat similar to the coatings heated at 600ºC. A combination of aluminum, oxygen and copper is formed at the surface of the coatings. The middle Platinum layer has almost vanished, a consequence of the relatively large amount of copper diffusion towards the surface. Hence, the optical properties change drastically (Fig.2), which is attributed to the reflectivity property of the metallic behavior of copper.

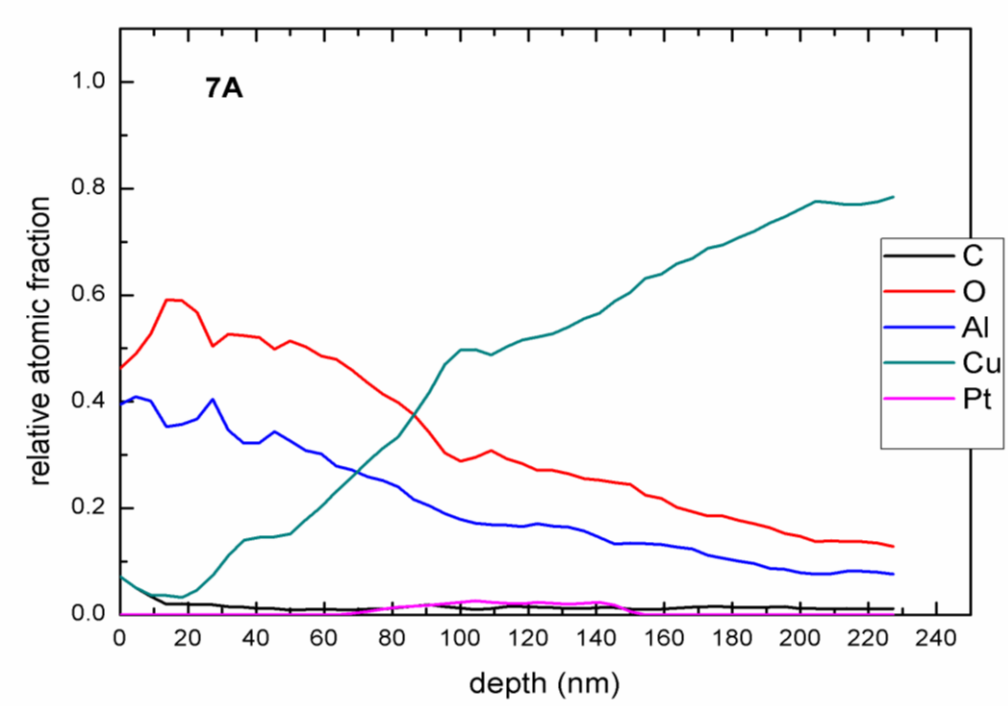

Figure 7: Elemental depth analysis of $Al_xO_y/Pt/Al_xO_y$ multilayer absorber heated at 700^oC in air for 2 h.

From XRD analysis of the coatings shown in chapter four, we found that annealing in air from 300-600 ^oC for 2 h shows a decrease in the intensity of X-ray diffraction pattern of Pt grains. Further increase of annealing temperature to 700^oC leads to complete disappearance of Pt diffraction peak and to the formation of weak diffraction intensities of CuO and Cu_2O phases. Moreover, the EDS analysis spectra shown in chapter four, also confirm a slight decrease in the intensity of platinum and aluminium peaks up to 500^oC and 600^oC. The peaks finally disappear at 700^oC. On the other hand, the copper and oxygen signals increase as annealing temperature increases. The observed composition matches with the result obtained from XRD analysis, which matches with the elemental depth profile analysis.

These results lead us to the conclusion that the main degradation mechanism of the $Al_xO_y/Pt/Al_xO_y$ multilayer solar absorber was diffusion of copper towards the surface of the

coating. Thus, it is clear that this multilayer solar selective absorber may improve its thermal stability through deposition of a thin diffusion barrier layer between the base Al_xO_y layer and copper substrate, which is the subject of the next chapter.

5.4 CONCLUSION

$Al_xO_y/Pt/Al_xO_y$ multilayer films have been deposited onto copper substrate at room temperature using an e-beam vacuum evaporator. The multilayer absorbers were annealed in air at different temperatures and characterised using spectrophotometry, emissometry, and Heavy Ion ERDA. The samples heated up to 500 ^oC were found to exhibit good spectral selectivity α/ε of 0.951/0.09. However, beyond 500 ºC the spectral selectivity decreased to 0.846/0.11, possibly due to thermally activated atomic interdiffusion profiles. The Heavy Ion ERDA measurement showed outward diffusion of copper substrate towards the surface and therefore, the decrease in the constituents of the absorber coating. It also confirmed that the average atomic fraction ratio of aluminum-to-oxygen at the first 90 nm of $Al_xO_y/Pt/Al_xO_y$ multilayer solar absorber heated up to 500 ºC was roughly 0.38:0.6 and beyond that, reduction of the relative atomic fraction with depth was observed as would be expected due to the thinner base Al_xO_y layer. XRD and EDS results confirmed the decrease in the intensity of Pt grains and the formation of oxidized Cu phases.

5.5 REFERENCES

5.1 Z. Y. Nuru, C. J. Arendse, T. F. G.Muller, M. Maaza, Mate scie and Engi B 177 (2012) 1188.

5.2 Z. Y. Nuru, C. J. Arendse, S. Khamlich, M. Maaza, Vacuum 86 (2012) 2129.

5.3 A. Jhon. Thornton, S. Alans Penfold, L Lamb James, Thin Solid Films 72 (1980) 101.

5.4 Harish C. Barshilia, N. Selvakumar, K. S. Rajam, Appl. Phys. 103 (2008) 023507(1).

5.5 Harish C. Barshilia, N. Selvakumar, G. Vignesh, K. S. Rajam, A. Biswa, Sol. Energy Mater. Sol. Cells, 93 (2009) 315.

5.6 N. Selvakumar, Harish C. Barshilia, K. S. Rajam, A. Biswas, Sol. Energy Mater. Sol. Cells, 94 (2010) 1412.

5.7 C. Kennedy, H. Price, NREL/CP-520-36581, (2005).

5.8 Y. Liu, C. Wang, Y. xue, Sol. Energy and solar Cells 96 (2012) 131.

5.9 J. R. Tesmer, M. Nastasi, ‘‘Hand book of Modern Ion Beam Materials Analysis’’, Materials Research Society, (1995).

5.10 M. J. F. Heal, Nucl. Instr, and Meth. B 129 (1997) 130.

5.11 E. F. Aguilera, P. Rosales, E. M. Quiroz, G. Murillo, M. C. Fernandez, Nucl. Instr, & Meth. B 244 (2006) 427.

5.12 W. Assmann, T. Reichelt, T. Eisenhammer, H. Huber, A. Mahr, H. Schellinger, R. Wohlgemuth, Nucl. Instr. & Meth. Phys. Res. B 113 (1996) 303.

5.13 T. Bostrom, J. Jensen, S. Valizadeh, G. Westin, E. Wackelgard, Sol Energy & solar Cells 92 (2008) 1177.

5.14 S. Khamlich, M. Msimanga, C. A. Pineda-Vargas, Z. Y. Nuru, R. McCrindle, M. Maaza, Mater. Char 70 (2012) 42.

5.15 A. Bergmaier, G. Dollinger, C. M. Frey, Nucl. Instr. & Meth. B 99 (1995) 488.

CHAPTER SIX

A TANTALUM DIFFUSION BARRIER LAYER TO IMPROVE THE THERMAL STABILITY OF $Al_xO_y/Pt/Al_xO_y$ SOLAR ABSORBER COATINGS

ABSTRACT

The incorporation of a Ta diffusion barrier layer on the thermal stability of $Al_xO_y/Pt/Al_xO_y$ multilayer solar absorber coatings has been investigated. The samples were annealed at temperatures up to 800°C for different durations in air. These were characterized by X-ray diffraction (XRD), scanning electron microscopy (SEM), energy dispersive x-ray spectroscopy (EDS), Atomic force microscopy (AFM), Raman spectroscopy, UV-vis spectroscopy and emissometry. The $Cu/Ta/Al_xO_y/Pt/Al_xO_y$ multilayer solar absorber coatings were found to be thermally stable up to 700°C in air for 2 h with good spectral selectivity α/ε of 0.937/0.10. At 800°C, the spectral selectivity decreased to 0.870/0.12, which is attributed to the diffusion of Cu and formation of CuO phase. The formation of CuO phase was confirmed by XRD, EDS and Raman spectroscopy. Long term thermal stability study showed the coatings were thermally stable in air up to 550°C for 24 h.

The content of this chapter is submitted to: Solar Energy

6.1 INTRODUCTION

The efficiency of conversion of solar energy into heat is mainly determined by the optical properties of the absorber surface. An efficient selective surface should have good optical properties i.e. high absorption over the spectral range of solar spectrum (0.3-2.5 μm) combined with low thermal losses because of the re-radiation at longer wavelengths (beyond 2.5 μm) and thermal stability of the component materials used [6.1]. Several solar absorber materials based on cermets and multilayer coatings: Pt–Al_2O_3 [6.2-6.6], Cr-Al_2O_3 [6.7], Ni-MgF_2 [6.8] and Al_2O_3/Mo/Al_2O_3 [6.9], Al_2O_3/ (Pt-Al_2O_3)/Al_2O_3 [6.10], Al_2O_3/ (Ni, Cr, Ta, Pt)/Al_2O_3 [6.11] have been reported respectively by various authors.

Due to its high thermal conductivity, low resistivity and high infrared reflectance, copper is mostly used as a substrate for solar selective absorbers such as TiAlN/TiAlON/Si_3N_4 [6.12], TiAlN/AlON [6.13], NbAlN/NbAlON/Si_3O4 [6.14], TiAlN/CrAlON/Si_3N_4 [6.15], Al_xO_y/Al/Al_xO_y [6.16], Mo/HfO_x/Mo/HfO_2 [6.17], Mo-AlN [6.18], Mo-Al_2O_3 [6.19] and Al_xO_y/Pt/Al_xO_y [6.20, 6.21]. The infrared reflectance of a metal is determined by free charge carriers that effectively conduct electrical current and heat [6.22]. As the electrons conduct low frequency longitudinal alternating currents, they are easily polarized under the influence of high frequency transverse electric field of light. This polarization results in a high infrared reflectance (low thermal emittance). However at temperatures above 300^oC, copper gets oxidized and diffuses into the absorber layer, resulting in the degradation of the solar selective absorber [6.23]. Therefore, to prevent the diffusion of copper towards the absorber, a suitable , thin and efficient diffusion barrier layer with high thermal stability and good optical properties is mandatory [6.24-6.26]. The properties required for an efficient diffusion barrier have been reviewed by Nicolet *et al* [6.27] and Wittmer *et.al* [6.28].

Refractory metals have been studied for application as diffusion barriers [6.29]. The leading diffusion barrier material now is tantalum and its alloys, due to its good adhesion [6.30], high melting point (3017^{o}C) [6.31], does not react with copper [6.31, 6.32]. The solubility of Ta in Cu and vice versa is very low in solid state [6.32]. Thus, Ta-based layers have been used as an excellent diffusion barrier in Cu metallization [33-35]. In this chapter, based on the advantage of Ta barrier, the $Al_xO_y/Pt/Al_xO_y$ multilayer absorber was deposited onto Ta coated Cu substrate using e-beam evaporation. We present the effect of Ta diffusion barrier on the structural, optical properties and thermal stability of $Al_xO_y/Pt/Al_xO_y$ multilayer absorber deposited by e-beam evaporation, which was heated in air at different temperatures and durations.

6.2 EXPERIMENTAL DETAIL

$Al_xO_y/Pt/Al_xO_y$ multilayer stacks of 900 Å Al_xO_y top layer, 70 Å Pt middle layer and 400 Å Al_xO_y base layer were deposited onto Ta coated copper ($3 \times 3cm^2$) substrates using 3 kW high vacuum e-beam evaporation system at room temperature. The experimental details without Ta diffusion barrier have been described in elsewhere [6.20, 6.21]. In addition, Ta disc (purity 99.9%) (40 mm in diameter) targets were placed on Cu crucibles for the deposition of Ta films. The e-beam current, pressure and deposition rate was 260 mA, 10^{-7} mbar, and 2.4 Å/s ± 0.6 Å/s respectively for Ta layers.

To study the thermal stability of the multilayer coatings, they were heated in air in an ultra-Furnace of Wirsam scientific type UF12/40/200 in the range of 400-800^{o}C at an increment of 100^{o}C for 2 h. The temperature was increasing from room temperature to the desired temperature at a rate of 5 ^{o}C/min and was cooled down at a rate of 2^{o}C/min. The accuracy of

the set temperature was ±7^{o}C. Similarly, we also tested long term thermal stability of the multilayer absorbers in air at 450^{o}C, 550^{o}C and 650^{o}C for 24 h. Thereafter the required analytical techniques were performed.

The microstructure of the as- grown and annealed coatings were recorded by using X-ray diffraction (XRD) Model Bruker AXS D8 advance of radiation Cu (K_{α} = 1.5406 Å) and a DILOR-JOBIN-YVON-SPEX integrated Raman spectroscopy. The morphology of the films was acquired using Leo-Stero Scan 440 Scanning electron microscope (SEM). The chemical composition was studied using energy-dispersive X-ray spectroscopy (EDS) of accelerating voltage of 15 kV. The surface roughness was studied using Veeco nanoman Atomic force microscopy (AFM) V operated in tapping mode.

Spectral reflectance was measured with a Cary 5000 UV–vis–NIR spectrophotometer of Varian, Inc. model internal DRA-2500 in the wavelength range of 0.3–2.5 μm. The solar absorptance was calculated from the measured reflectance data and weighted by solar irradiance using standard AM1.5 solar spectrum in the above wavelength range. Thermal emittance spectra were acquired by an emissometer model AE1, which has an accuracy of ± 0.01 emittance units.

6.3 RESULTS AND DISCUSION

6.3.1 Structural properties

Fig. 1 shows XRD pattern of the as-deposited and annealed Cu/Ta/Al_xO_y/Pt/Al_xO_y multilayer solar absorber coatings for 2 h in air. The XRD data showed strong peaks at 2θ = 43.3^{o}, 50.44^{o} and 74.08^{o}, which correspond to (111), (200) and (220) reflections of Cu substrate. The low

and broadened peak cantered at about $2\theta = 40.2^{o}$ is attributed to the fcc Pt (111). Annealing samples from 400-700^{o}C showed a decrease in the intensity of Pt intensities, which could be due to the decrease in thickness of Pt layers. No diffraction peaks pertaining to any phases of copper or any reaction products were formed, which shows that Ta acted as an effective diffusion barrier. However at 800^{o}C, weak diffraction intensity of CuO at $2\theta = 38.2^{o}$ appears, which is attributed to the polycrystalline nature of the thin Ta, which allows Cu atoms to move towards the surface at high temperature. No diffraction peaks of Ta was appeared, which could be due to the thickness of the layer, and Al_xO_y films are amorphous.

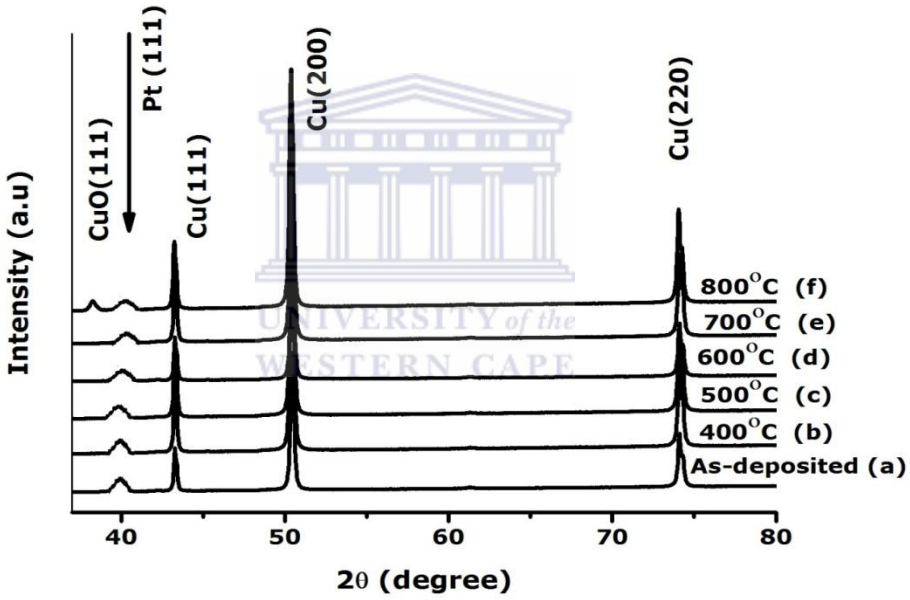

Figure 1: XRD pattern of Cu/Ta/Al_xO_y/Pt/Al_xO_y multilayer solar absorber coatings as-deposited (a) and annealed at different temperatures in air for 2 h: 400^{o}C (b), 500^{o}C (c), 600^{o}C (d), 700^{o}C (e), and 800^{o}C (f).

The Raman spectrum of the as-deposited and annealed up to 800^{o}C, which will be discussed later, showed two broad bands centred at approximately 190 and 833 cm^{-1}. These bands do not correspond to any Al_2O_3 phases, but rather corresponds to the vibration of aluminium and

oxygen atoms, respectively [6.37]. Al_2O_3 exists in several crystalline phases such as $\gamma - Al_2O_3$ with *Fd 3m* space group and $\alpha - Al_2O_3$ with *R 3 c* space group. The former does not exhibit any active Raman modes [6.38] but the latter one exhibits seven Raman active phonon modes: $2A_{1g}$ (418 cm^{-1}, 648 cm^{-1}) and $5E_g$ (332, 431, 450, 526 and 745 cm^{-1}) [6.39]. No bands correspond to any oxide phases of Ta and any phases of Al_xO_y were observed that matches with XRD result.

6.3.2 Surface morphology

Fig. 2(a)-(f) shows the surface morphology of Cu/Ta/ Al_xO_y/Pt/Al_xO_y multilayer solar absorber as deposited and heat treated at different temperatures in air for 2 h: (a) as-deposited, (b) 400ºC,(c) 500ºC, (d) 600ºC, (e) 700ºC and (f) 800ºC. The as-deposited multilayer solar absorber surface (Fig. 2(a)) is stacked by many small spherical like particles that have well defined boundaries. After annealing the samples up to 700ºC, a growth in the particle size is observed with increasing temperature. At 800°C (Fig. 2(f)), the particles agglomerate and forms larger particles. The increase in the size of the particles did not allow the outward diffusion of copper towards the surface up to 700°C as probed by EDS (as shown in the next section), which is attributed to the properties of Ta that acted as an effective diffusion barrier layer in the Cu/Ta/Al_xO_y/Pt/Al_xO_y multilayer solar absorbers. No voids or cracks were observed from the SEM images.

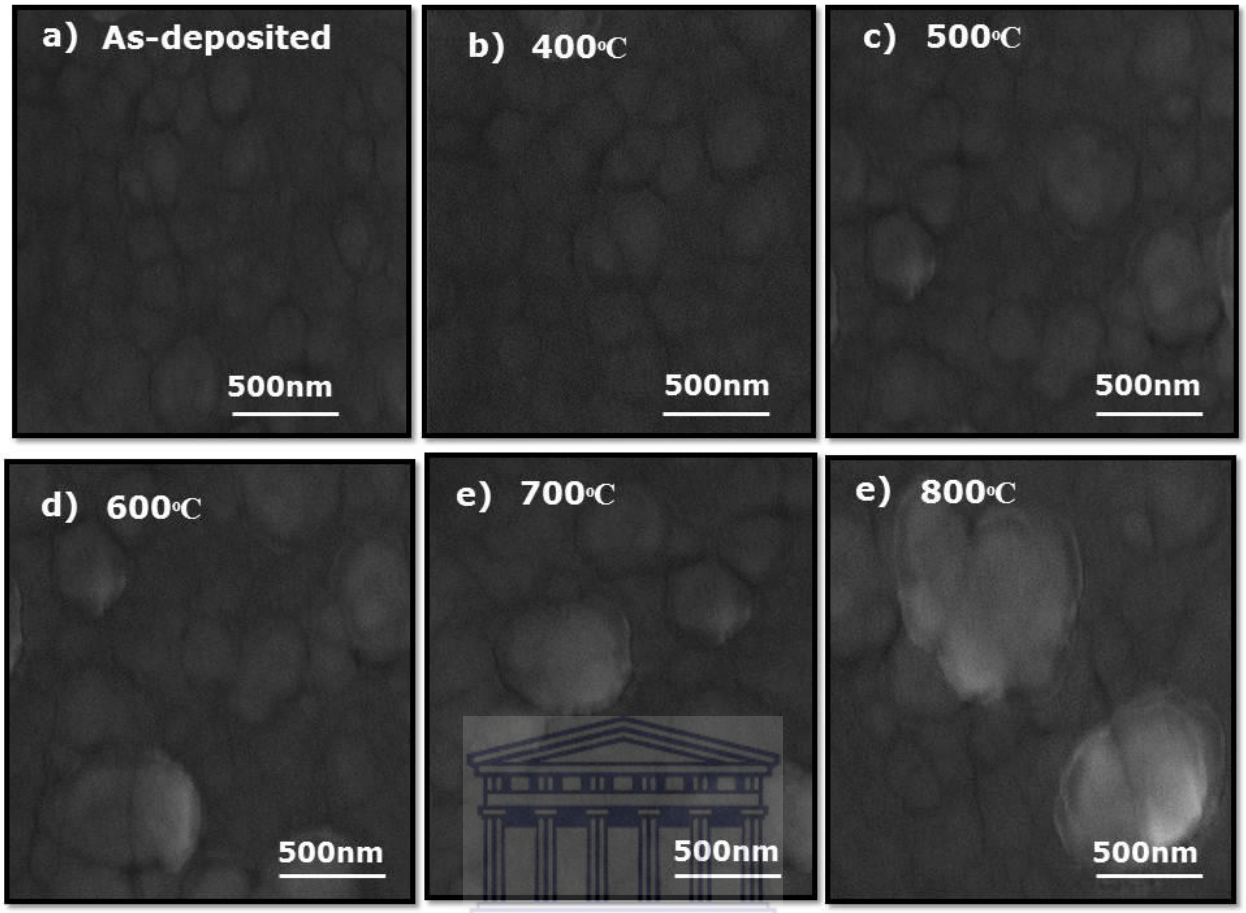

Figure 2: SEM images of Cu/Ta/Al_xO_y/Pt/ Al_xO_y multilayer solar absorber coatings as-grown (a) and annealed at different temperatures in air for 2 h: 400°C (b), 500°C (c), 600°C (d), 700°C (e), and 800°C (f).

Fig. 3(a)-(f) depicts the AFM images of Cu/Ta/Al_xO_y/Pt/Al_xO_y multilayer solar absorber as-deposited and heat treated at different temperatures in air for 2 h: (a) as-deposited, (b) 400°C, (c) 500°C, (d) 600°C, (e) 700°C and (f) 800°C. The images showed columnar growth, as would be expected from evaporated coatings grown from vapour phase deposition at low substrate temperature [6.40]. After annealing the multilayer solar absorber coatings, the particle sizes, the average diameter as well as the surface roughness increased. The average surface roughness (8.1 ± 0.01 nm) of the coatings did not show significant change up to 700°C. However at

800°C, the surface roughness increased significantly to 25 ± 0.02 nm, which is attributed to the noticeable increase in the particle size.

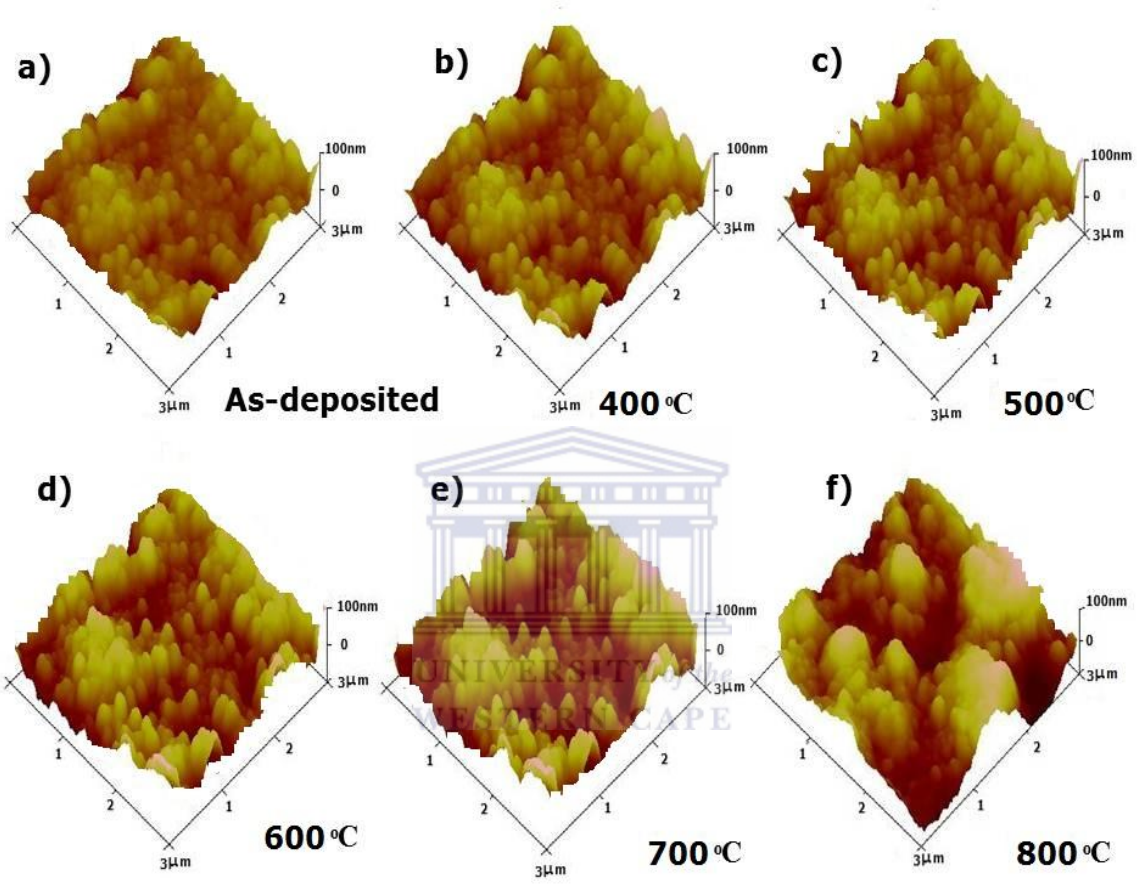

Figure 3: AFM images Cu/Ta/Al_xO_y/Pt/ Al_xO_y multilayer solar absorber coatings as-grown (a) and annealed at different temperatures in air for 2 h: 400°C (b), 500°C (c), 600°C (d), 700°C (e), and 800ºC (f).

6.3.3 Compositional properties

Fig. 4(a)-(f) shows the EDS analysis of Cu/Ta/Al_xO_y/Pt/Al_xO_y multilayer solar absorber as-deposited state and annealed at 400°C, 500°C, 600°C, 700°C and 800°C in air for 2 h

respectively. EDS spectra showed only sharp peaks from Ta (which wasn't shown by XRD), platinum, aluminium, oxygen and from the copper substrate, confirming the pure nature of the prepared Cu/Ta/Al_xO_y/Pt/Al_xO_y multilayer solar absorber coatings. Annealing the Cu/Ta/Al_xO_y/Pt/Al_xO_y multilayer solar absorber coatings up to 700ºC did not show an increase in copper and oxygen signal, which is due to the good adhesion behaviour of Ta with copper that prohibits Cu atoms to migrate during heating. Only at 800ºC, an increase in Copper signal observed, which confirms the XRD result.

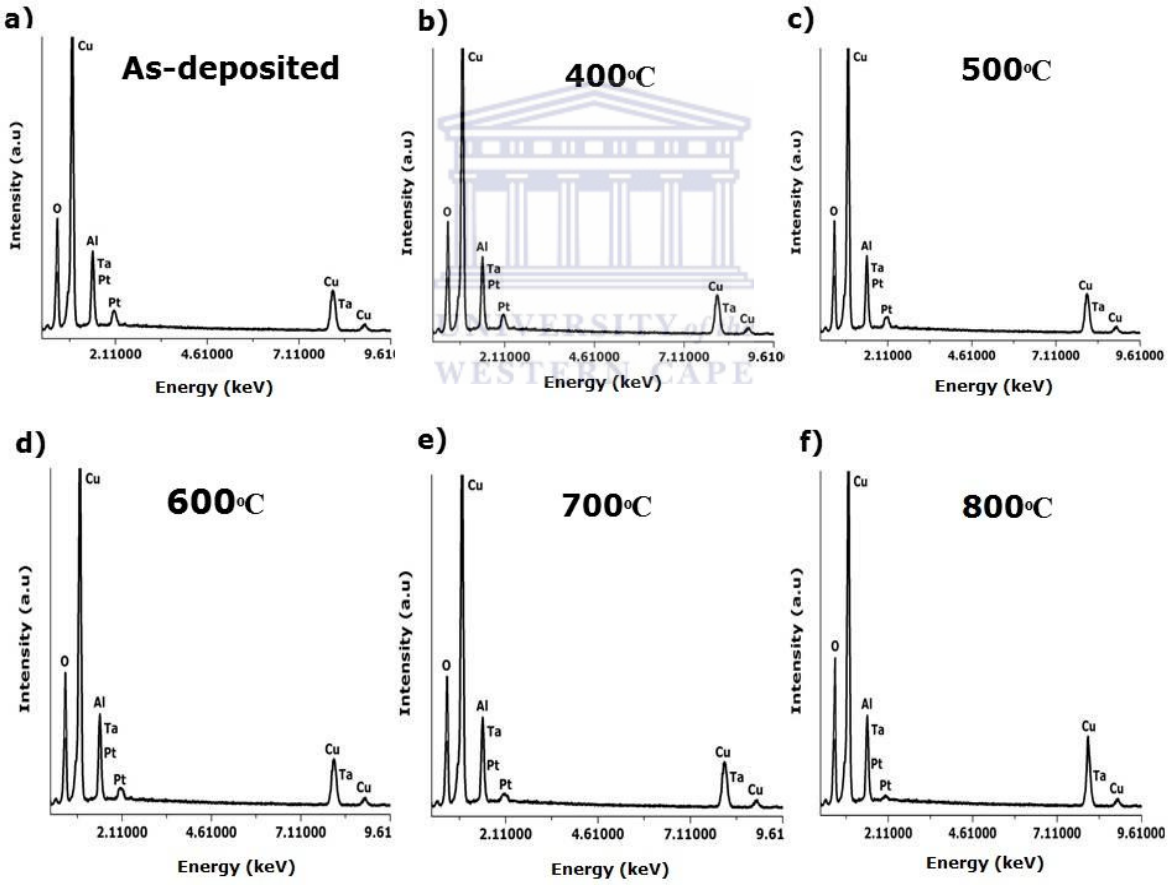

Figure 4: EDS spectra Cu/Ta/Al_xO_y/Pt/ Al_xO_y multilayer solar absorber coatings as-grown (a) and annealed at different temperatures in air for 2 h: 400ºC (b), 500ºC (c), 600ºC (d), 700ºC (e), and 800ºC (f).

6.3.4 Thermal stability in air

The study of the thermal stability in solar absorber coatings is very important as the degradation of the coatings at higher operating temperatures results in a decrease in solar absorptivity and an increase in thermal emissivity. The thermal stability of the $Cu/Ta/Al_xO_y/Pt/Al_xO_y$ multilayer solar absorber coatings was studied by annealing the coatings in air in the range of 400 - 800°C for 2 h. Fig. 5 shows the reflectance spectra of $Cu/Ta/Al_xO_y/Pt/Al_xO_y$ multilayer solar absorber coatings in the as-deposited state and annealed at 400°C, 500°C, 600°C, 700°C and 800°C in air each for 2 h. The corresponding (α) and (ε) values of the multilayer coating are given in Table 1. It is evident that the α and ε values did not show significant change after heat treatment up to 700°C. This indicates that $Cu/Ta/Al_xO_y/Pt/Al_xO_y$ multilayer solar absorber have good thermal stability up to 700°C in air, which is attrbuted to the peculiar property of Ta that acts as an effective diffusion barrier for the copper substrate. However, at 800°C, the absorptance values decreased $(\Delta\alpha = -0.06)$ and the emittance values increased $(\Delta\varepsilon = +0.03)$, which is attributed to the diffusion of Cu into the coating and the formation of oxide phase as confirmed by XRD. This was confirmed using Raman spectroscopy.

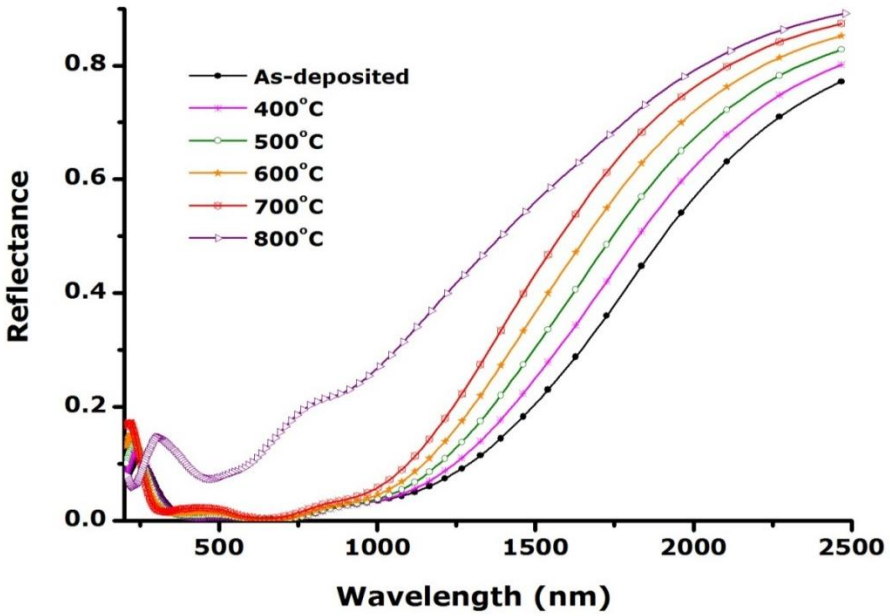

Figure 5: Reflectance spectra of Cu/Ta/Al_xO_y/Pt/ Al_xO_y multilayer solar absorber coatings as-grown and heat treated in air for 2 h.

Temperature (°C)	Absorptance (α)			Emittance (ε at 82°C)		
	As-deposited	Annealed	$\Delta\alpha$	As-deposited	Annealed	$\Delta\varepsilon$
Room temperature	0.940	-	-	0.09	-	-
300	0.940	0.940	-	0.09	0.09	-
400	0.940	0.940	-	0.09	0.09	-
500	0.939	0.938	-0.001	0.09	0.10	+0.01
600	0.939	0.938	-0.001	0.09	0.10	+0.01
700	0.938	0.937	-0.001	0.09	0.10	+0.01
800	0.930	0.870	-0.060	0.09	0.12	+0.03

Table 1: Effect of annealing in air for 2 h on solar absorptance and thermal emittance values of Cu/Ta/Al_xO_y/Pt/Al_xO_y multilayer solar absorber.

The Raman spectra of the as-deposited Cu/Ta/Al_xO_y/Pt/Al_xO_y multilayer solar absorber and coatings annealed up to 800^{o}C in air for 2 h is shown in Fig. 6. There was no significant change in the nature of Raman spectra even after heat treated at 700^{o}C. However, at 800^{o}C, an additional single peak centred at around 211 cm^{-1} appeared which correspond to the formation of CuO [6.41]. This was also confirmed by XRD and EDS.

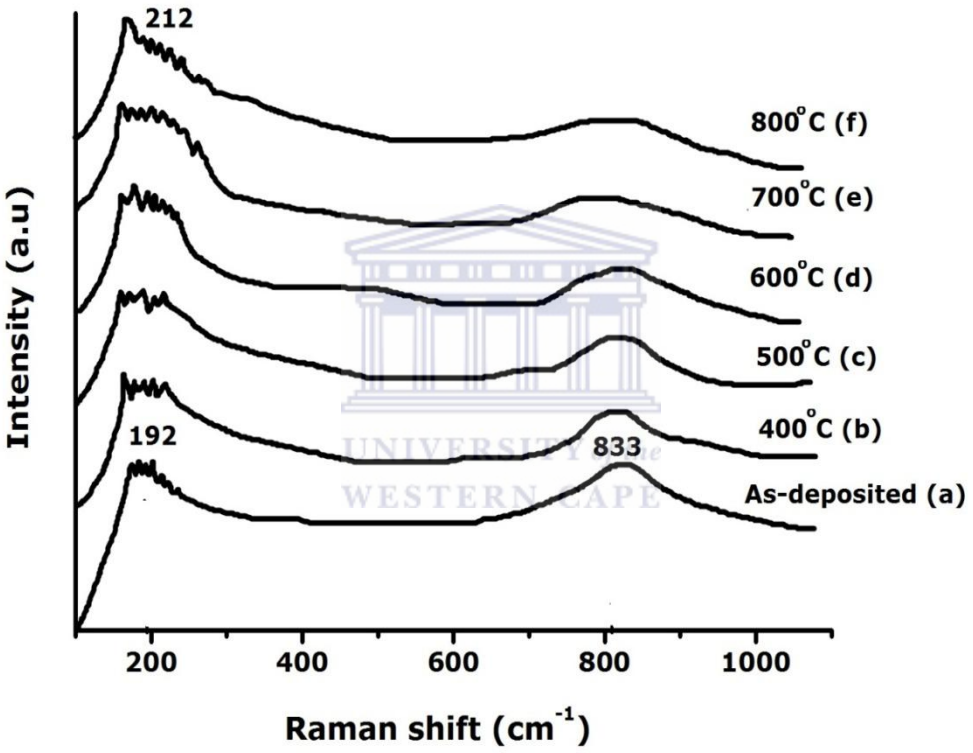

Figure 6: Raman spectra of Cu/Ta/Al_xO_y/Pt/ Al_xO_y multilayer solar absorber coatings as-deposited (a) and annealed at different temperatures in air for 2 h: 400^{o}C (b), 500^{o}C (c), 600^{o}C (d), 700^{o}C (e), and 800^{o}C (f).

6.3.5 Long term thermal stability in air

In order to study whether the Cu/Ta/Al_xO_y/Pt/Al_xO_y multilayer solar absorber coatings can be applicable for longer duration for high temperature concentrated solar thermal applications, they were heated in air for 24 h. Fig. 7 shows the reflectance spectra of the multilayer solar absorber coatings as-deposited and heat treated in air for 24 h: 450ºC, 550ºC and 650ºC.

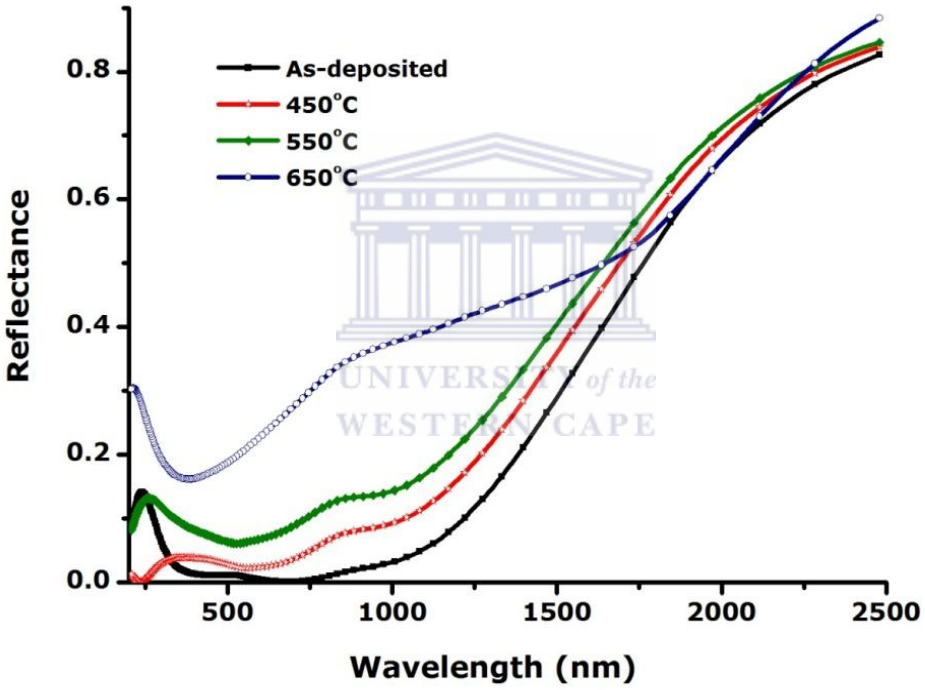

Figure 7: Reflectance spectra of Cu/Ta/Al_xO_y/Pt/ Al_xO_y multilayer solar absorber coatings as-deposited and heat treated in air for 24 h.

The absorptance and emittance values are shown in Table 2. There was no significant change in the absorptance and emittance values even after annealing up to 550ºC.This was also

confirmed by Raman spectroscopy as shown below. However, at 650ºC, the absorptance values decreased $\Delta\alpha = -0.13$ and the emittance $(\Delta\varepsilon = +0.03)$ values increased.

Temperature (ºC)	Absorptance (α)			Emittance (ε at 82°C)		
	As-deposited	Annealed	$\Delta\alpha$	As-deposited	Annealed	$\Delta\varepsilon$
Room temperature	0.940	-	-	0.08	-	-
350	0.940	0.940	-	0.08	0.08	-
450	0.941	0.941	-	0.08	0.08	-
550	0.940	0.938	- 0.002	0.08	0.09	+0.01
650	0.940	0.810	-0.130	0.08	0.12	+0.03

Table 2: Effect of annealing in air for 24 h on solar absorptance and thermal emittance values of Cu/Ta/Al_xO_y/Pt/Al_xO_y multilayer solar absorber coatings.

From the XRD and Raman spectroscopy data shown in Fig. 8 and Fig. 9 respectively, this was due to the formation of CuO. The Cu/Ta/Al_xO_y/Pt/Al_xO_y multilayer solar absorber coatings are thermally stable in air at 550ºC for 24 h.

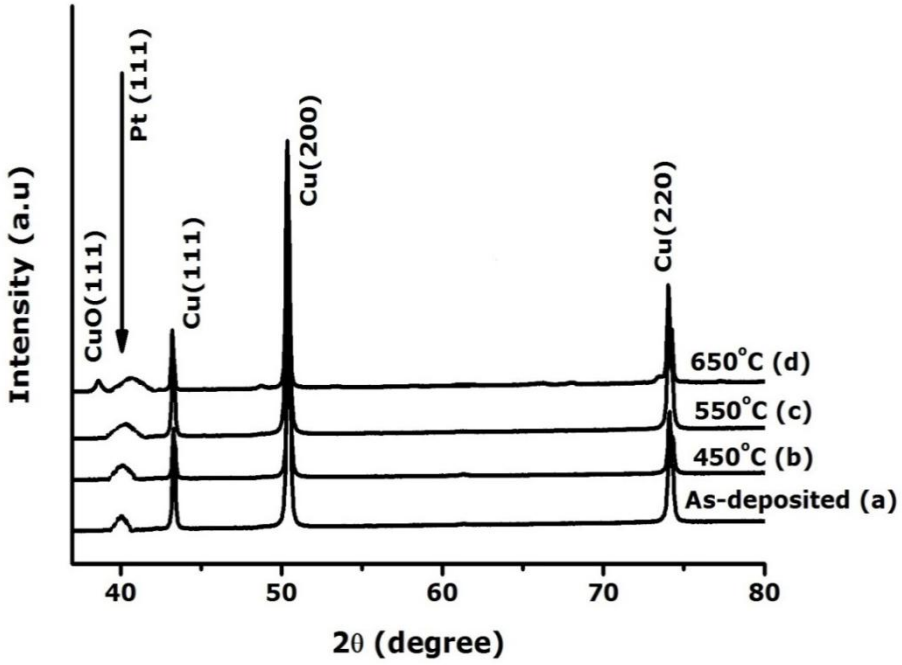

Figure 8: XRD pattern of Cu/Ta/Al_xO_y/Pt/Al_xO_y multilayer solar absorber coatings as-grown (a) and annealed at different temperatures in air for 24 h: 450°C (b), 550°C (c), and 650ºC (d).

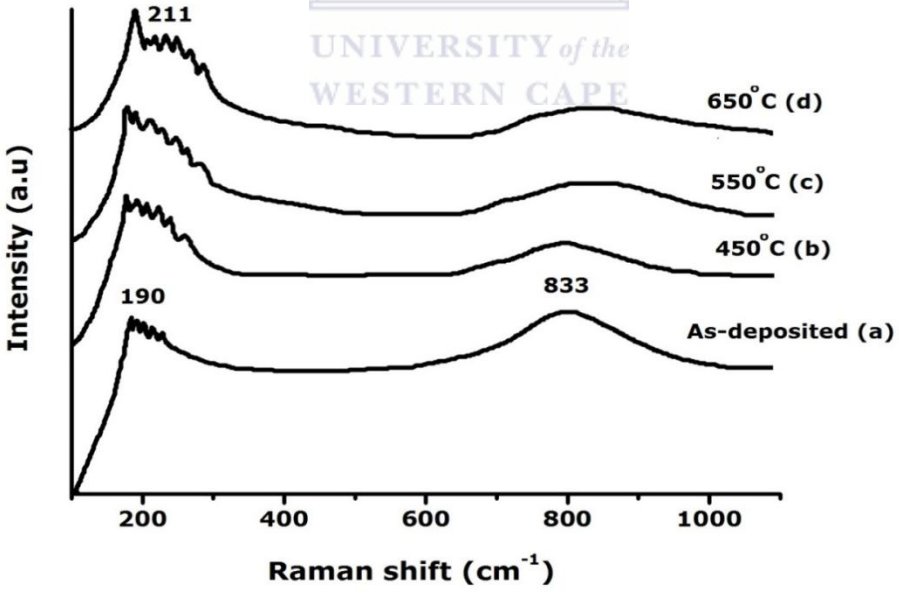

Figure 9: Raman spectra of Cu/Ta/Al_xO_y/Pt/Al_xO_y multilayer solar absorber coatings as-deposited (a) and annealed at different temperatures in air for 24 h: 450°C (b), 550°C (c), 550ºC (d), and 650ºC (d).

Hence one can conclude that using a Ta thin layer as a diffusion barrier to $Al_xO_y/Pt/Al_xO_y$ multilayer solar absorber coatings was an effective method to improve the thermal stability of the coatings.

6.4 CONCLUSION

To improve the thermal stability of $Al_xO_y/Pt/Al_xO_y$ multilayer solar absorber, a thin Ta layer was deposited between copper substrate and the coatings at room temperature using e-beam vacuum evaporator. The multilayer absorber was annealed in air for different temperatures and durations. XRD, EDS and Raman spectroscopy showed formation of CuO only at 800ºC. An increase in the surface roughness was also observed at 800ºC by AFM. The optical property of Cu/Ta/ $Al_xO_y/Pt/Al_xO_y$ in air for 2 h was found to be stable up to 700°C, with solar selectivity α/ε of 0.937/0.10. At 800ºC, its selectivity decreased significantly to 0.870/0.12, which is attributed to the diffusion of copper and formation of CuO phase. Long term annealing showed that the multilayer coating was stable up to 550°C in air for 24 h and showed spectral selectivity of 0.938/0.09. Hence using a Ta thin layer as a diffusion barrier was effective to improve the thermal stability of the multilayer solar absorber coatings.

6.5 REFERENCES

6.1 B. O. Seraphin, ‘‘Solar energy conversion: solid state physics aspects’’, in: Topics in Applied Physics, Vol. 31, Springer, Berlin, (1979), 24.

6.2 C. Sella, T. K. Vien, J. lafait, S. Berthier, Thin Solid Films 90 (1982) 425–431.

6.3 J. Lafait, S. Berthier, C. Sella, T. K. Vien, Vacuum 30 (1986) 125–127.

6.4 M. Maaza, O. Nemraoui, C. Sella, J. Lafait, A. Gibaud, V. Pischedda, Physics Letters A 344 (2005) 57–63.

6.5 M. Maaza, O. Nemraoui, C. Sella, J. Lafait, A. Gibaud, B. Baruch-Barak, A. C. Beye, Solid State Communications 137 (2006) 166–170.

6.6 Zebib.Y. Nuru, C. J. Arendse, R. Nemutudi, O. Nemraoui, M. Maaza, Physica B, 407 (2012) 1634–1637.

6.7 D. R. Mckenzie, , Applied Physics letters 34 (1979) 25-28.

6.8 M. Mast, K. Gindele, M. Kohl, Thin Solid Films 126 (1985) 37-42.

6.9 R. E. Peterson, J. W. Ramsey, Journal of Vacuum Science & Technology 12 (1975) 174.

6.10 J. A. Thornton, J. L. Lamb, Thin Solid Films 83 (1981) 377 – 385.

6.11 J. A. Thornton, J. L. Lamb, Thin Solid Films 96 (1982) 175-183.

6.12 H. C. Barshilia, N. Selvakumar, K. S. Rajam, D. V. S. Rao, K. Muraleedharan, A. Biswas, Applied Physics letters 89 (2006) 191909- 1- 191909-3.

6.13 H. C. Barshilia, N .Selvakumar, K. S. Rajam. A. Biswas, Solar Energy Materials & Solar cells 92 (2008) 1425-1433.

6.14 H. C. Barshilia, N .Selvakumar, K. S. Rajam. A. Biswas, Solar Ener Mat & Sol cells 92 (2008) 495-504.

6.15 N. Selvakumar, H. C. Barshilia, K. S. Rajam. A. Biswas, ‘‘spectrally selective TiAlN/CrAlON/$Si3N_4$ tandum absorber for high temperature solar applications in:

Renewable Energy and Environment for sustainable development'', Narosa publishing house, 2008, 469 – 477.

6.16 H. C. Barshilia, N. Selvakumar, G. Vignesh, K. S. Rajam, A. Biswas, Solar Energy Materials &Solar cells 93 (2009) 393 – 403.

6.17 N. Selvakumar, H. C. Barshilia, K. S. Rajam, , A. Biswas, Solar Energy Materials & Solar cells 94 (2010) 1412 – 1420.

6.18 Q. C. Zhang, Solar Energy Materilas & Solar cells 62 (2000) 63-74.

6.19 Q. C. Zhang, Y. Yin, D. R. Mills, Solar Energy Materilas & Solar cells 40 (1996) 43-53.

6.20 Z. Y. Nuru, C. J. Arendse, T. F. G. Muller, M. Maaza, Material science and Engineering B 177 (2012) 1188-1193.

6.21 Z. Y. Nuru, C. J. Arendse, S. Khamlich, M. Maaza, Vacuum 86 (2012) 2129-2135.

6.22 K. Gelin, Ph.D. Thesis, Uppsala Universoty, Sweden, (2004).

6.23 H. C. Barshilia, N. Selvakumar, K. S. Rajam, D. V. Sridhara Rao, K. Muraleedharan, Thin Solid Films 516 (2008) 6071-6078.

6.24 W. J. Ward, K. M. Carroll, J. Electronchem. Soc:Solid State Sci. Tech-nol 129 (1982) 227.

6.25 M. M. Akhmedova, Sov. Phys., Semicond. 10 (1976) 1400.

6.26 S. K. Gandhi, ''VLSI Fabrication Principles'', Wiley, New York, (1983) 420-445.

6.27 M. A. Nicolet, Thin Solid Films 52 (1978) 415.

6.28 M. Wittmer, J. Vac. SCi. Technol. A2 2 (1984).

6.29 M. Peikert, E. Wieser, H. Reuter, C. Wenzel, Vacuum 69 (2003) 91-95.

6.30 T. Laurila, K. Zeng, J. K. Kivilahti, J. Molarius, I. Suni, J. Appl. Phys 88 (2000) 3377.

6.31 L. Chen, B. Ekstrom, J. Kelber, Mater. Res. Soc. Symp. Proc. 564 (1999) 287.

6.32 P. R. Subramanian, D. E. Laughlin, Bull. Alloy Phase Diagrams 10 (1989) 652.

6.33 K. Holloway, P. M. Fryer, C. Cabral Jr, J.M.E. Harper, P.J. Bailey, K. H.Kellehr, J. Appl. Phys. 71 (1992) 5433.

6.34 L. A. Clevenger, N. A. Bojarezuk, K. Holloway, J. M. E. Harper, C. Cabral, R. G. Schad, F. Cardone, L. Stolt, J. Appl. Phys. 73 (1993) 300.

6.35 L. Kaufman, Calphad 15 (1991) 243.

6.36 D. Gupta, Mater. Chem.Phys.41 (1995) 199.

6.37 H. Arashi, J. Am. Ceram. Soc, 75 (1992) 844-847.

6.38 A. Mortensen, D. H. Christensen, O. F. Nielsen, E. Pedersen, J. Raman Spectosc. 22 (1991) 47-49.

6.39 A. Misra, H. D. Bist, M. S. Navati, R. K. Thareja, J. Narayan, Mater. Sci. Eng. B 79 (2001) 49-54.

6.40 R. B. Pettit, ‘‘Total hemispherical emittance measurement apparatus for solar selective coatings’’, SAND-75-0079, Albuquerque, NM: Sandia National Laboratory, (1975).

6.41 D. Chen, G. Shen, K. Tang, Y. Qian, J. Crys. Growth 254 (2003) 225–228.

SUMMARY

Currently the world relies on fossil fuels to produce 86% of its energy. However, the combustion of fossil fuels generates greenhouse gas, which is the major factor responsible for global warming. To overcome the environmental problems and to fulfil the ever increasing demand of energy, mankind should use renewable energy sources. The sun, one of renewable sources, is the vast majority of energy used by people on earth. The sun's energy is environmental friendly and can be converted to heat and electricity. Hence to harness this inexhaustible energy, solar-thermal systems are the most important candidates. The critical part of these systems is the solar absorber surface, which attracts considerable attention for photo-thermal conversion. To increase the photo-thermal conversion efficiency, the solar absorber surface should capture the maximum solar energy in the high intensity visible and near infrared spectral regions and should have minimum emittance for thermal IR radiation. Moreover, it should be thermally stable at high temperatures (>400^{o}C) in air for high temperature solar-thermal systems.

In this thesis, we have designed and deposited an approximately 1370 Å thick Al_xO_y/Pt/Al_xO_y solar selective coating which was fabricated using high vacuum e-beam evaporator. From the optical constants (n and k) obtained using ellipsometry of each layer, the top and base Al_xO_y layers used in the corresponding coatings were naturally dielectric and the middle Pt layer, was semi-transparent. The thickness was optimized to achieve high solar absorptance $\alpha \sim 0.94 \pm 0.01$ and low thermal emittance $\varepsilon \sim 0.06 \pm 0.01$ at 82^{o}C. Light absorption was due to intrinsic and interference mechanism for Pt layer and due to interference mechanism for Al_xO_y layers. RBS and EDS analysis confirmed that Al_xO_y layers used in the corresponding coating was non-

stoichiometric. SEM and XRD analysis showed the Pt grains are in the fcc crystalline phase with a broad size distribution and spheroidal shape in and between the rims of Al_xO_y. The surface roughness of the stack was found to be comparable to the interparticle distance and it was negligible in comparison with the film thickness. Optical measurements confirmed that light absorption in the $Al_xO_y/Pt/Al_xO_y$ multilayer coatings was due to the multiple reflectance from the layers.

In order to study the thermal stability of the $Al_xO_y/Pt/Al_xO_y$ multilayer solar absorber films, the multilayer absorbers were annealed in air for different temperatures and durations. XRD analysis showed a decrease in the intensity of Pt grain for the multilayers heated from 300 – 600^{o}C in air for 2 h, and completely disappeared and formed CuO and Cu_2O phases at 700^{o}C. This was also confirmed by Raman spectroscopy. A slight increase in the mean size of Pt particles was observed from the samples heated from 300 – 500^{o}C in air for 2 h. The average surface roughness of the multilayers was found to increase slightly with annealing temperature. EDS, HI-ERDA and optical modelling spectra confirmed formation of oxidized copper and the disappearance of Pt. The optical property of $Al_xO_y/Pt/Al_xO_y$ in air for 2 h was found to be stable up to 500^{o}C, with solar selectivity α/ε of 0.951/0.09. At 600^{o}C and 700^{o}C, its selectivity decreased significantly to (0.92/0.10) and 0.846/0.11, respectively, which is attributed to the diffusion of copper and formation of CuO and Cu_2O phases. Long term annealing showed that the multilayer coating was stable up to 450^{o}C in air for 24 h and showed spectral selectivity of 0.963/0.08. The Heavy Ion ERDA measurement showed outward diffusion of copper substrate towards the surface and therefore, the decrease in the constituents of the absorber coating. It also confirmed that the average atomic fraction ratio of aluminum to-oxygen at the first 90 nm of $Al_xO_y/Pt/Al_xO_y$ multilayer solar absorber heated up to 500 ^{o}C was roughly 0.38:0.6 and beyond that, reduction of the relative atomic fraction with depth was

observed as would be expected due to the thinner base Al_xO_y layer. XRD and EDS results confirmed the decrease in the intensity of Pt grains and the formation of oxidized Cu phases.

To improve the thermal stability of $Al_xO_y/Pt/Al_xO_y$ multilayer solar absorber, a thin Ta layer was deposited between copper substrate and the coatings at room temperature using e-beam vacuum evaporator. The multilayer absorber was annealed in air for different temperatures and durations. XRD, EDS and Raman spectroscopy showed formation of CuO only at 800ºC. An increase in the surface roughness was also observed at 800ºC by AFM. The optical property of Cu/Ta/ $Al_xO_y/Pt/Al_xO_y$ in air for 2 h was found to be stable up to 700^{o}C, with solar selectivity α/ε of 0.937/0.10. At 800ºC, its selectivity decreased significantly to 0.870/0.12, which is attributed to the diffusion of copper and formation of CuO phase. Long term annealing showed that the multilayer coating was stable up to 550^{o}C in air for 24 h and showed spectral selectivity of 0.938/0.09. Hence using a Ta thin layer as a diffusion barrier was effective to improve the thermal stability of the multilayer solar absorber coatings. Therefore, one can conclude that the spectrally selective Cu/Ta/AlxOy/Pt/AlxOy multilayer solar absorber can be applicable for high temperature solar-thermal applications.

LIST OF ARTICLES INCLUDED IN THIS THESIS

1. **Z. Y. Nuru,** C. J. Arendse**,** T. F.Muller and M. Maaza**,** "*Optimization of Al_xO_y /Pt/Al_xO_y multilayer spectrally selective coatings for high temperature applications"* Vacuum, 86 (2012) 2129-2135.

2. **Z. Y. Nuru,** C. J. Arendse**,** S. khamlich and M. Maaza**,** "Structural *and optical properties of Al_xO_y / Pt / Al_xO_y multilayer absorber*" Materials Science and Engineering*: B,* 177 (2012) 1188– 1193.

3. **Z. Y. Nuru**, S. Kamlich. T. F. Muller , C. J. Arendse, M. Maaza, *" Thermal stability of e-beam evaporated* Al_xO_y/Pt/Al_x O_y *multilayer solar absorbers"* Solar Energy materials & Solar Cells, 120 (2014) 473-480.

4. **Z. Y. Nuru**, M. Misamanga, C. J. Arendse, M. Maaza, *"Heavy Ion Elastic Recoil Detection analysis of Al_xO_y/Pt/Al_xO_y multilayer solar absorbers"* Applied surface science (2014), http://dx.doi.org/10.1016/.

5. **Z. Y. Nuru**, C. J. Arendse, M. Maaza, *"A tantalum diffusion barrier layer to improve the thermal stability of Al_xO_y/Pt/Al_xO_y multilayer solar absorber"* Solar Energy, submitted.

Comments on my contribution

I am responsible for the writing the above five publications. I prepared all samples, performed theoretical calculations, and analyzed both theoretical and experimental results.

ARTICLES NOT INCLUDED IN THIS THESIS

---

1 **Z. Y. Nuru**, C. J. Arendse, R. Nemutudi, O. Nemraoui, M. Maaza *"Pt-Al_2 O_3 nanocoatings for high temperature concentrated solar thermal power applications"* Physica B 407, (2012) 1634–1637

2 M. Maaza, **Z. Y. Nuru**, B. D. Ngom, S. Khamlich, *"Surface-interface investigation and stability of cermet based solar absorbers by grazing angle x-rays reflectometery: Pt-Al_2O_3 case'* 'The Arabian Journal for Science and Engineering, (Accepted 2013).

3 S. Khamlich, M. Msimanga, C. A. Pineda-Vargas, **Z. Y. Nuru**, R. McCrindle, M. Maaza, *"Compositional analysis and depth profiling of thin film CrO2 by heavy ion ERDA & standard RBS: a comparison"* Materials Characterization, 70, (2012), 42-47.

4 S. Khamlich, R. McCrindle, **Z. Y. Nuru**, N. Cingo, M. Maaza, *"Annealing effect on the structural and optical properties of Cr-Cr2O3 monodispersed particles based solar absorbers",* Applied Surface Science 265 (2013) 745– 749

5 **Z. Y. Nuru**, S. Kamlich. K. Roro, T. F. Muller , C. J. Arends, M. Maaza, *"Microstructure and spectral selectivity of Pt-Al_2 O_3 nanocoatings for high temperature applications"* 56th SA Institute of physics page 262– 266 conference Proceeding ISBN: 978-1-86888-688-3

6 S. Kamlich. **Z. Y. Nuru**, J. Sithole, O. Nemraoui, K. Roro, N. Mongwaketsi, R. Mcrindle, N. Cingo, M. Maaza, *" Cr/α –Cr_2O_3 monodispersed spherical core-shell particles based solar absorbers"* 56th SA Institute of physics Page 140 – 144 conference Proceeding ISBN: 978-1-86888-688-3.